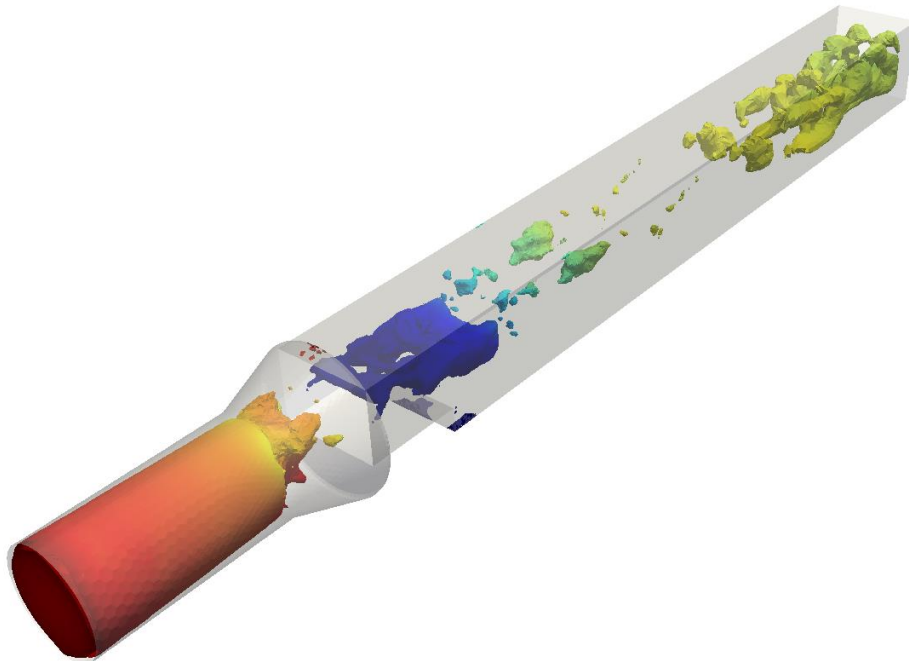




CHALMERS
UNIVERSITY OF TECHNOLOGY



Fibre modelling in venturi flow and disc refiner

Implementation and development of models
for turbulent fibre suspension flow

Master's thesis in Engineering Mathematics and Computational Science

SIMON INGELSTEN

Department of Applied Mechanics
Division of Fluid Dynamics
CHALMERS UNIVERSITY OF TECHNOLOGY
Gothenburg, Sweden 2014

MASTER'S THESIS IN ENGINEERING MATHEMATICS AND
COMPUTATIONAL SCIENCE

Fibre modelling in venturi flow and disc refiner
*Implementation and development of models for
turbulent fibre suspension flow*

Master's thesis 2015:23

SIMON INGELSTEN

Department of Applied Mechanics
Division of Fluid Dynamics
CHALMERS UNIVERSITY OF TECHNOLOGY
Gothenburg, Sweden 2015

Fibre modelling in venturi flow and disc refiner
Implementation and development of models for turbulent fibre suspension flow
SIMON INGELSTEN

© SIMON INGELSTEN, 2015

Master's thesis 2015:23
ISSN 1652-8557
Department of Applied Mechanics
Division of Fluid Dynamics
Chalmers University of Technology
SE-412 96 Gothenburg
Sweden
Telephone +46 (0)31-772 1000

Cover:

Instantaneous picture from simulation in a pipe connected to a channel with a backwards facing step used for fibre model validation. Volumes show areas where the effective viscosity in the Bingham model is larger than 50 times the viscosity of water. The volumes are coloured by pressure.

Abstract

As a part of a larger project in developing a new technology for increased energy efficiency in the pulp and paper industry a model for turbulent fibre suspension flow was needed. The model was also desired to be suitable for applications alongside additional multiphase flow models to study cavitation in fibre suspension flows. Two models with different levels of complexity were studied. A relatively simple model was the Bingham model where a fibre suspension is described as a non-Newtonian fluid. The model acts through modification of the viscous stresses, as the suspension viscosity is computed as a function of shear rate. A more complex model, denoted the ODF model, was implemented by modifying the viscous stress tensor with additional stresses computed from the orientation distribution of suspended fibres. A model for the orientation distribution function (ODF) was proposed and developed within the thesis work and used to construct explicit expressions for the additional stress tensor components as functions of the flow field with the use of Fourier series.

Both fibre models were implemented to Fluent through user-defined functions (UDF) written in C programming language. The models were validated and the best performing parameter setting was identified by performing simulations of turbulent fibre suspension flow and comparing the results to experimental data from literature. Both fibre models resembled experimental data fairly well and had a reasonable computational cost. In comparison the performances of the models were roughly similar. Although both models showed potential the Bingham model gave slightly better resemblance of the experimental data was at the same time fairly simple to implement. In addition the ODF model was judged still needing further and more rigorous study. The Bingham model was therefore identified as the better and more reliable model at the current stage.

Further validation of the chosen model, i.e. the Bingham model, was made by using it in an example application. A simplified model of a disc refiner was used and the fibre suspension flow was simulated with the Bingham model. The simulation yielded results to be expected and that resembled results from literature.

Key words: Fibre modelling, Fibre suspension rheology, Bingham model, Fibre orientation distribution, Computational fluid dynamics, Energy efficiency, Disc refiner

Thesis Layout

This thesis work is based on the following research papers that have been submitted for publication in conferences and journals.

- Modelling of Turbulent Fibre Suspension Flow – A State of the Art CFD Analysis, Simon Ingelsten, Anton Lundberg, Vijay Shankar, Lars-Olof Landström, Örjan Johansson, submitted to the conference, 11th International Conference on Advances in Fluid Mechanics, 5 - 7 September 2016, Ancona, Italy
- Virtual Modelling of Turbulent Fibre Flow in a Low Consistency Refiner for a Sustainable and Energy Efficient Process, Simon Ingelsten, Anton Lundberg, Vijay Shankar, Lars-Olof Landström, Örjan Johansson, submitted to the conference, 13th International Conference of Numerical Analysis and Applied Mathematics, 23-29 September, Rhodes, Greece

Acknowledgements

This Master's thesis is part of the E2MPi (Energy Efficiency in Mechanical Pulp) project carried out by ÅF-Industry AB in collaboration with ÅForsk, Energimyndigheten, Luleå University of Technology, Holmen, SCA and Stora Enso. Examiner for the thesis is Srdjan Sasic at Chalmers University of Technology.

First of all, I would like to thank everyone who has made this thesis possible. I would like to thank my supervisor Vijay Shankar for assigning the exciting project to me and for guiding me along the way. I would like to thank my colleague Anton Lundberg who have been a great support and help throughout my thesis work. I would like to thank Lars-Olof Landström for providing the original idea for the project.

I would also like to hand out a giant thank you to my family who always supports me, to my friends who always keep my feet at the ground and to my girlfriend Louise who always believes in me and treats me like I could to anything.

Contents

1	Introduction.....	1
2	Aim	3
2.1	Desired model features.....	3
2.2	Limitations	4
3	Theory	5
3.1	Fluid mechanics	5
3.1.1	Reynolds averaged Navier-Stokes	6
3.1.2	Large eddy simulations	8
3.1.3	Detached Eddy Simulations	9
3.1.4	Courant-Friedrich-Lewy condition	10
3.2	Fibre suspensions and fibre modelling.....	10
3.2.1	Bingham viscoplastic fluid model.....	11
3.2.2	Fibre orientation distribution.....	12
3.3	Experimental measurements of fibre suspensions.....	13
3.3.1	Fibre suspension flow over a backwards facing step.	13
3.3.2	Fibre suspension flow in rectangular channel	15
3.4	Disc refiners	16
4	Method	17
4.1	Fibre modelling	17
4.1.1	Bingham model	18
4.1.2	ODF model.....	19
4.2	Comparison with experiments by Claesson et al (2012).....	27
4.2.1	Mesh creation and fitting geometry	28
4.2.2	Grid independence study	30
4.2.3	Simulations with the Bingham model	31
4.2.4	Simulations with the ODF model.....	31
4.3	Comparison with experiments by Xu & Aidun (2005).....	33
4.4	Disc refiner application	35
4.4.1	Mesh.....	35
4.4.2	Simulations.....	36
5	Results.....	39

5.1	Comparison with experiments by Claesson et al. (2012).....	39
5.1.1	Simulations with pure water.....	40
5.1.2	Grid independence study.....	41
5.1.3	Simulations with the Bingham model.....	43
5.1.4	Simulations with the ODF model.....	52
5.1.5	Comparison between the respective models.....	66
5.2	Comparison with experiments by Xu & Aidun (2005).....	68
5.3	Disc refiner application.....	70
6	Discussion.....	75
6.1	Error sources.....	75
6.2	Fibre models.....	77
6.2.1	Bingham model.....	77
6.2.2	ODF model.....	78
6.2.3	Comparison of fibre models.....	80
6.3	Disc refiner application.....	80
6.4	Future work.....	80
6.4.1	Bingham model.....	81
6.4.2	ODF model.....	81
7	Conclusion.....	83
	References.....	85

1

Introduction

Production of energy makes up for a significant part of the emission of greenhouse gases and in Europe the use and supply of energy, transport excluded, made up for 60% of all such emissions in 2012 (European Commission, 2014). The Intergovernmental Panel on Climate Change (IPCC) have reported that greenhouse gas emissions caused by humans do have a significant effect on the climate system, and that emission levels now are the highest in our history (IPCC, 2014). Overall energy efficiency in the world is thus important for minimising climate changes caused by human activities. In a report from the Swedish Energy Agency (Swedish Energy Agency, 2014) it can be read that the pulp and paper industry makes up for about 52% of the total energy consumption in the Swedish industrial sector. Developing methods for increased energy efficiency within the pulp and paper industry is thus a highly relevant area of research for contributing to increased overall energy efficiency in Sweden and, in extension, the world.

This Master's thesis is part of a larger project carried out by ÅF-Industry AB in collaboration with ÅForsk, Energimyndigheten, Luleå University of Technology, Holmen, SCA and Stora Enso. The project focuses on the development of a new technology for increased energy efficiency in the process of refining wood fibres in the pulp and paper industry. A new technology has been proposed by Johansson & Landström (2010) in which the concept of flow induced cavitation is put to use. Their idea is based on using the collapse of intentionally induced cavitation bubbles for the fibrillation stage, instead of the commonly used and highly energy demanding disc refiners (Illikainen et al., 2007; Rajabi Nasab et al., 2014).

In another project, carried out by ÅF-Industry AB in collaboration with Volvo Car Corporation, a method for shape optimisation with the use computational fluid dynamics (CFD) was developed (Lundberg et al., 2015). In the first phase of the present project a method to optimise venturi shape in cavitating flows over a set of geometrical parameters was developed from the methodology (Lundberg et al., 2014). The optimisation was then applied for the shape of a venturi using simulations of pure water (Frenander et al., 2015). To further validate and improve the venturi design, prior to the construction of a physical prototype, simulations of fibre suspension flows were needed and a suitable fibre model was thus desired.

Fibre suspensions exhibit complex rheology, which is governed by contact forces between fibres. The rheological properties are also strongly dependent on concentration,

fibre properties and flow regime (Kerekes, 2006). Modelling of fibre suspension flow can grow very complex, especially if micro-scale physical phenomena are to be resolved. Macro-scale models of relatively simple types do exist but may provide limited accuracy and be restricted to certain regimes with regards to flow rate and fibre concentration. The wide span in complexity serve to illustrate that choosing and applying a fibre model that is both efficient and sufficiently accurate is far from trivial. To identify a fibre model suitable for the scope of the main project a study to choose and, if possible, further develop one or more fibre models was thus desired. Such a study was conducted and is described in this Master's thesis.

2

Aim

The aim of this Master's thesis was to deliver a fibre suspension model suitable for engineering simulations of turbulent flow. More specifically the model should be suitable for use in simulations on the venturi geometry designed in the main project. To satisfy the aim models should be evaluated with respect to accuracy, complexity and to what extent they provide necessary features for the simulations in mind. After evaluating existing modelling approaches a set of suitable models should be chosen for implementation and, if possible, further development. The models should be validated by comparing simulated results with experimental data, preferably for benchmark flow cases and cases containing features similar to the venturi. As an example application, the model should also to be used to simulate the flow in a simplified disc refiner. The sub-tasks that needed to be completed in order to fulfil the aim are listed below, namely

- evaluation of available fibre models,
- choice of suitable fibre models,
- further development and implementation of fibre models,
- validation with experimental data to identify the best model,
- application on simplified disc refiner.

2.1 Desired model features

The model was intended to be used for simulations in the venturi geometry designed in the main project in which additional models for cavitation the flow were also intended to be used. In those simulations the fibres effect on the cavitation was a main interest. It was therefore desired that the model described how the suspension flow is affected by fibres being present, contrary to a model with one-way coupling where the flows effect on the fibres is described but not vice versa. The multiphase flow models that were intended to be used to simulate cavitation exhibits certain numerical instabilities. A desired property of the fibre model was thus for it to be relatively stable, so that introduction of unnecessary numerical instabilities was avoided. In addition to instabilities, the simulations on the venturi geometry demands fine resolution in space and time. The additional computational effort introduced by the fibre model should therefore be kept to a minimum. The desired features of the resulting model are listed below, namely

- a coupling between fibres effects and fluid momentum,

- minimal introduction of additional numerical instability,
- minimal introduction of additional computational cost.

2.2 Limitations

Since fluid flow with fibres is a very complex physical situation, there are many uncertainties with respect to modelling and the reliability of numerical solutions. The implementation itself can also grow difficult if the models are complex. This thesis work mainly focused on modelling how turbulent fibre suspension flows behave as a collective result of fibres being present. Detailed description and information of fibres as individual particles was outside the scope of the work. Since fibre suspension rheology is strongly dependent on concentration and properties of the fibres the modelling in this work was limited those suspensions of the type of interest. The type was softwood fibres with mass concentration around 1%.

For the simulations needed to validate the fibre models the computational resources were limited to single laptop workstation with a 4 core CPU. The number of simulations that could be performed to study the fibre models was thus limited. Implementation of the fibre models were intended for the ANSYS Fluent software (ANSYS Inc. (b), 2013). The models available were therefore limited to those having possible implementation through so-called user defined functions (UDF) written in C programming language. All work conducted within the thesis was also made without performing any physical experiments. Experimental data for validation was therefore limited to the one available in literature.

3

Theory

Theory relevant for the thesis work is presented in this section. First fluid mechanics and turbulence modelling is covered, followed by theory on fibre suspensions in general and on fibre modelling in more detail. Literature with experimental data intended for the validation of fibre models is then presented. Finally a short introduction to the concept of disc refiners is given.

3.1 Fluid mechanics

The theory of fluid mechanics is centred on equations governing conservation of mass, momentum and energy. The governing equation for conservation for mass, called the continuity equation, reads in tensor notation (Davidson, 2014)

$$\frac{\partial \rho}{\partial t} + \rho \frac{\partial u_i}{\partial x_i} = 0 \quad (3.1)$$

where ρ is fluid density, u_i is velocity and x_i is spatial direction. From this point and on all flows will be considered incompressible, implying that $\partial \rho / \partial t = 0$. Equation (3.1) then gives

$$\frac{\partial u_i}{\partial x_i} = \frac{\partial u}{\partial x} + \frac{\partial v}{\partial y} + \frac{\partial w}{\partial z} = 0 \quad (3.2)$$

where u , v and w are the velocities in the Cartesian x -, y - and z -coordinates, respectively. In Equation (3.2) Einstein's summation convention for the tensor notation, i.e. that indices appearing twice in the same term are summed over, was explicitly shown. The equation governing conservation of linear momentum reads (Davidson, 2014)

$$\rho \frac{\partial u_i}{\partial t} + \rho u_j \frac{\partial u_i}{\partial x_j} = \frac{\partial \sigma_{ji}}{\partial x_j} + \rho f_i \quad (3.3)$$

where σ_{ij} are the stress tensor and f_i the body force acting on the fluid. The stress tensor may be decomposed into normal stresses and shear stresses, also known as pressure and viscous stresses, respectively, as (Davidson, 2014)

$$\sigma_{ij} = -p\delta_{ij} + \tau_{ij} \quad (3.4)$$

where δ_{ij} is the unit tensor and τ_{ij} is the viscous stress tensor. The constitutive law for Newtonian incompressible viscous fluids reads (Davidson, 2014)

$$\tau_{ij} = \mu \left(\frac{\partial u_i}{\partial x_j} + \frac{\partial u_j}{\partial x_i} \right) = 2\mu S_{ij} \quad (3.5)$$

where μ is the dynamic viscosity of the fluid and S_{ij} , the symmetric part of the velocity gradient tensor, is called the strain rate tensor. Combination of Equation (3.3), Equation (3.4) and Equation (3.5) gives the transport equation for linear momentum, called the Navier-Stokes equation (Davidson, 2014):

$$\rho \frac{\partial u_i}{\partial t} + \rho u_j \frac{\partial u_i}{\partial x_j} = -\frac{\partial p}{\partial x_i} + \mu \frac{\partial^2 u_i}{\partial x_j \partial x_j} + \rho f_i. \quad (3.6)$$

Equation (3.6) may be discretised and solved directly. However, very high resolution in space and time is usually needed to correctly resolve a turbulent flow field. Instead, turbulence modelling is often employed to reduce the computational resources needed. Models relevant for this work are described below.

3.1.1 Reynolds averaged Navier-Stokes

It is preferable for many turbulent flows to decompose the instantaneous velocity and pressure fields into their time-averaged components, assumed steady, and their fluctuating parts. By decomposing velocity and pressure as

$$u_i = \bar{u}_i + u'_i, \quad (3.7)$$

$$p = \bar{p} + p', \quad (3.8)$$

where $\bar{\cdot}$ denotes time averaging and \cdot' denotes fluctuation, and then time-average the Navier-Stokes equation (3.6) the Reynolds Averaged Navier-Stokes equation (RANS) is obtained, reading (Davidson, 2014)

$$\rho \bar{u}_j \frac{\partial (\bar{u}_i)}{\partial x_j} = -\frac{\partial \bar{p}}{\partial x_i} + \frac{\partial}{\partial x_j} \left(\mu \frac{\partial \bar{u}_i}{\partial x_j} - \rho \overline{u'_i u'_j} \right). \quad (3.9)$$

The time-averaged incompressible continuity equation reads

$$\frac{\partial \bar{u}_i}{\partial x_i} = 0, \quad (3.10)$$

which together with the original continuity equation (3.1) gives

$$\frac{\partial u'_i}{\partial x_i} = 0. \quad (3.11)$$

The last term in the RANS equation $\overline{\rho u'_i u'_j}$, called the Reynolds stress tensor, is unknown and needs to be modelled for the system of equations governing the fluid flow to be closed.

The Boussinesq assumption

In many turbulence models used for solving the RANS equation the so-called Boussinesq assumption is used. The unknown Reynolds stresses are then modelled as diffusion-like transport by introducing a turbulent viscosity, or eddy viscosity, ν_t . This is called the Boussinesq assumption and reads (Davidson, 2014)

$$-\overline{u'_i u'_j} = \nu_t \left(\frac{\partial \bar{u}_i}{\partial x_j} + \frac{\partial \bar{u}_j}{\partial x_i} \right). \quad (3.12)$$

The turbulent viscosity ν_t needs to be computed with some model. Such models are described below.

The $k - \varepsilon$ model

In the $k - \varepsilon$ model the turbulent viscosity is computed from the turbulent kinetic energy k and the turbulent dissipation ε as (Davidson, 2014)

$$\nu_t = c_\mu \frac{k^2}{\varepsilon} \quad (3.13)$$

where c_μ is a model constant. k and ε are obtained by solving the modelled transport equation for the respective quantities, reading (Davidson, 2014)

$$\bar{u}_j \frac{\partial k}{\partial x_j} = \frac{\partial}{\partial x_j} \left[\left(\nu + \frac{\nu_t}{\sigma_k} \right) \frac{\partial k}{\partial x_j} \right] + P_k - \varepsilon, \quad (3.14)$$

$$\bar{u}_j \frac{\partial \varepsilon}{\partial x_j} = \frac{\partial}{\partial x_j} \left[\left(\nu + \frac{\nu_t}{\sigma_\varepsilon} \right) \frac{\partial \varepsilon}{\partial x_j} \right] + \frac{\varepsilon}{k} c_{\varepsilon 1} P_k - c_{\varepsilon 2} \frac{\varepsilon^2}{k}, \quad (3.15)$$

where σ_k , σ_ε , $c_{\varepsilon 1}$ are $c_{\varepsilon 2}$ are model constants and the production term for turbulent kinetic energy reads

$$P_k = \nu_t \left(\frac{\partial \bar{u}_j}{\partial x_j} + \frac{\partial \bar{u}_j}{\partial x_i} \right) \frac{\partial \bar{u}_i}{\partial x_j}. \quad (3.16)$$

The $k - \omega$ model

In the $k - \omega$ model the turbulent viscosity is computed from the turbulent kinetic energy k and the so-called specific dissipation rate ω as (Davidson, 2015)

$$\nu_t = \frac{k}{\omega} \quad (3.17)$$

where the specific dissipation is related to the turbulent kinetic energy and the turbulent dissipation rate through a constant β^* as

$$\varepsilon = \beta^* \omega k . \quad (3.18)$$

The quantities k and ω are obtained from solving the modelled transport equation for k , i.e. Equation (3.14), and the modelled transport equation for ω reading (Davidson, 2015)

$$\bar{u}_j \frac{\partial \omega}{\partial x_j} = \frac{\partial}{\partial x_j} \left[\left(\nu + \frac{\nu_t}{\sigma_\omega} \right) \frac{\partial \omega}{\partial x_j} \right] + \frac{\omega}{k} (c_{\omega 1} P_k - c_{\omega 2} k \omega) \quad (3.19)$$

where σ_ω , $c_{\omega 1}$ and $c_{\omega 2}$ are model constants.

The $k - \omega$ SST model

Two main weaknesses of the $k - \varepsilon$ model are over-prediction of shear stress in adverse pressure gradient flows and the need of near-wall modification. While the $k - \omega$ model is better than the $k - \varepsilon$ model in adverse pressure gradient flows it depends on the free stream value of ω . A solution can be the $k - \omega$ SST model, which combines the models and behaves like the $k - \omega$ model near walls and like the $k - \varepsilon$ model in the outer region. (Davidson, 2014)

Using the relation between ω and ε from Equation (3.18), using that $\beta^* = c_\mu$ and assuming $\sigma_k = \sigma_\varepsilon$ the modelled transport equation for ε , i.e. Equation (3.15), is reformulated to an equation for ω as (Davidson, 2014)

$$\bar{u}_j \frac{\partial \omega}{\partial x_j} = \frac{\partial}{\partial x_j} \left[\left(\nu + \frac{\nu_t}{\sigma_\varepsilon} \right) \frac{\partial \omega}{\partial x_j} \right] + \alpha \frac{\omega}{k} P_k - \beta \omega^2 + \frac{2}{k} \left(\nu + \frac{\nu_t}{\sigma_\varepsilon} \right) \frac{\partial k}{\partial x_j} \frac{\partial \omega}{\partial x_j} \quad (3.20)$$

where α and β are model constants derived from the model constants of the $k - \varepsilon$ and the $k - \omega$ models. The $k - \omega$ SST model switches smoothly between coefficients for the $k - \omega$ model and the $k - \varepsilon$ model with the use of a blending function $\xi \in [0,1]$ employed in the computation of β .

3.1.2 Large eddy simulations

If a flow needs to be resolved in both space in time, the Navier-Stokes equations may be filtered, i.e. volume averaged, so that large turbulent scales are resolved but small turbulent scales, called sub-grid scales (SGS), are modelled. This is called large eddy simulation (LES). In this case the pressure and velocity fields, respectively, are decomposed into their volume averages, or filtered quantities, and SGS fluctuations as

$$u_i = \langle u_i \rangle + u_i'' \quad (3.21)$$

$$p = \langle p \rangle + p'' \quad (3.22)$$

where $\langle \cdot \rangle$ denotes volume average and \cdot'' denotes sub-grid fluctuation. Using the composition and volume averaging the Navier-Stokes equation (3.6) yields the filtered Navier-Stokes equation (Davidson, 2014),

$$\frac{\partial \langle u_i \rangle}{\partial t} + \langle u_j \rangle \frac{\partial \langle u_i \rangle}{\partial x_j} = -\frac{1}{\rho} \frac{\partial \langle p \rangle}{\partial x_i} + \frac{\mu}{\rho} \frac{\partial^2 \langle u_i \rangle}{\partial x_j \partial x_j} - \frac{\partial \tau_{ij}^{SGS}}{\partial x_j}, \quad (3.23)$$

and the filtered incompressible continuity equation

$$\frac{\partial \langle u_i \rangle}{\partial x_i} = 0. \quad (3.24)$$

The SGS stresses $\rho \tau_{ij}^{SGS}$ in the filtered Navier-Stokes equation, reading (Davidson, 2014)

$$\tau_{ij}^{SGS} = \langle u_i u_j \rangle - \langle u_i \rangle \langle u_j \rangle, \quad (3.25)$$

are unknown and needs to be modelled to close the system of equations for the fluid flow.

The Smagorinsky-Lilly model

The SGS stresses in the filtered Navier-Stokes equation may be modelled by the Boussinesq assumption, similarly to the RANS models in Section 3.1.1, as (Davidson, 2014)

$$-\tau_{ij}^{SGS} = \nu_{SGS} \left(\frac{\partial \langle u_i \rangle}{\partial x_j} + \frac{\partial \langle u_j \rangle}{\partial x_i} \right) = 2\nu_{SGS} \langle S_{ij} \rangle \quad (3.26)$$

where ν_{SGS} is called the SGS viscosity and needs to be computed using some model. A common model used is the Smagorinsky-Lilly model, which is available for the LES model in Fluent, where the SGS viscosity is computed as (ANSYS Inc. (a), 2013)

$$\nu_{SGS} = L_S^2 |\langle S \rangle| \quad (3.27)$$

with

$$|\langle S \rangle| = \sqrt{2 \langle S_{ij} \rangle \langle S_{ij} \rangle}. \quad (3.28)$$

and with L_S denoting the mixing length for sub-grid scales, computed as

$$L_S = \min[\kappa d, C_S \Delta] \quad (3.29)$$

where κ is the von Kármán constant, d is the distance to the closest wall, C_S is the Smagorinsky constant and Δ is the local grid scale.

3.1.3 Detached Eddy Simulations

Detached Eddy Simulations (DES) uses a combination of LES and the unsteady version of RANS, called URANS, to capture the boundary layer with RANS and the detached eddies away from the boundary layer using LES (Davidson, 2014). DES based on two-equation turbulence models, e.g. $k - \varepsilon$ and $k - \omega$, switches between RANS mode and LES mode by switching the method used to calculate the turbulent length scale l_t and the

dissipation ε_T as. For instance, in DES with the $k - \varepsilon$ model the quantities are computed as (Davidson, 2014)

$$l_t = \min\left(C_\mu \frac{k^{3/2}}{\varepsilon}, C_k \Delta\right), \quad (3.30)$$

$$\varepsilon_T = \max\left(\varepsilon, C_\varepsilon \frac{k^{3/2}}{\Delta}\right), \quad (3.31)$$

where the first arguments in the minimum and maximum operators, respectively, correspond to RANS mode and the second arguments correspond to LES mode.

3.1.4 Courant-Friedrich-Lewy condition

A conditions which is often preferred to satisfy in transient CFD-simulations is the Courant-Friedrich-Lewy condition. The dimensionless CFL number is defined as (Tu et al., 2013)

$$C = \frac{u \Delta t}{\Delta x} \quad (3.32)$$

where u is velocity, Δt the time step and Δx the local grid size. The CFL condition states that $C \leq 1$ must be satisfied to guarantee stability in numerical solutions. A CFL number $C = 1$ corresponds to a case where fluid particles travel one cell per time step (Davidson, 2014).

3.2 Fibre suspensions and fibre modelling

Fibre suspensions exhibit complex rheology and a range of physical phenomena influence the flow pattern with varying significance depending on the fibre concentration, fibre length and flow regime (Kerekes, 2006). Various non-dimensional numbers have been defined in literature characterise fibre suspensions with respect to concentration. A commonly used number, called the crowding number, is the average number of fibres in the volume of a sphere swept by a fibre length, calculated as (Kerekes, 2006)

$$N_c = \frac{2}{3} C_V \left(\frac{L}{d}\right)^2 \quad (3.33)$$

where C_V is volume concentration of fibres, L fibre length and d fibre diameter. Fibre suspensions are associated with a yield stress, which varies in magnitude from suspension to suspension, that has to be exceeded for the network of fibres yield and for the suspension to behave as a fluid contrary to something more similar to an elastic solid (Andersson et al., 1999). Fibre suspensions also have the tendency to form flocs, i.e. local concentration of fibres sticking together through mechanical inter-fibre forces, that can be important for the suspension rheology (Derakhshandeh et al., 2011). Flocculation occurs, for instance, in flows with decaying turbulence which also is the most common flocculating flow in papermaking processes (Kerekes, 2006).

The flow regime and the flow pattern near solid boundaries can be of importance for fibre suspension rheology. Pipe flow may be used as an illustrative example. At low velocity fibres move in a plug formation in the centre of the pipe, with almost no relative motion between fibres, while a clear water annulus can be observed close to the wall (Fock et al., 2011). With increasing velocity the annulus becomes turbulent and increases in size and starts mixing the fibres more and more until a fully turbulent flow is attained for the whole pipe cross section (Derakhshandeh et al., 2011). In the turbulent regime the rheology of pulp suspensions is close to the one of Newtonian fluids and they are therefore often referred to as “fluidized” (Bennington & Kerekes, 1996).

When it comes to modelling of fibre suspensions, different modelling approaches exist with wide differences in complexity, accuracy and computational effort needed. Models span from detailed description of individual fibres, modelled as chains of linked segments tracked individually in the fluid flow field (Lindström & Uesaka, 2008), (Andric et al., 2013), to modelling of the fibre suspension as a single fluid with non-Newtonian rheology (Ford et al., 2006), (Fock et al., 2010). The coupling between fibre orientation distribution and fluid momentum has also been used in the modelling of fibre suspension flow (Yang et al., 2013), (Krochak et al., 2009), (Moosaie & Manhart, 2013). Modelling approaches relevant for this thesis are presented below.

3.2.1 Bingham viscoplastic fluid model

A macroscopic approach to model fibre suspension rheology is to use the non-Newtonian Bingham viscoplastic fluid model. In the model the suspension is associated with a yield stress τ_y which is the shear stress that must be exceeded to initiate flow. If the yield stress is not exceeded the material will behave as solid. If the yield stress is exceeded, on the other hand, the material behaves like a Newtonian fluid. (Irgens, 2014)

The relationship between shear stress and shear rate can be summarised as (Irgens, 2014)

$$\begin{cases} \tau(\dot{\gamma}) \leq \tau_y, & \text{when } \dot{\gamma} = 0 \\ \tau(\dot{\gamma}) = \left[k + \frac{\tau_y}{|\dot{\gamma}|} \right] \dot{\gamma}, & \text{when } \dot{\gamma} \neq 0 \end{cases} \quad (3.34)$$

where k is the consistency index and $\dot{\gamma}$ is the shear rate, defined as

$$\dot{\gamma} = \sqrt{S_{ij}S_{ij}}. \quad (3.35)$$

A sketch of the relationship between stress and shear rate for the Bingham viscoplastic fluid model can be seen in Figure 3.1.

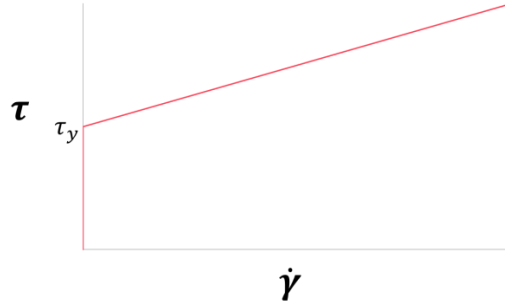


Figure 3.1: Relationship between shear stress τ and shear rate $\dot{\gamma}$ for the Bingham viscoplastic fluid model. Figure from the main project report (Lundberg et al., 2015).

The rheology of a Bingham viscoplastic fluid may be expressed in the relationship between shear rate $\dot{\gamma}$ and effective viscosity η is the fluid as (Irgens, 2014)

$$\eta(\dot{\gamma}) = \begin{cases} \infty, & \text{when } \tau_m < \tau_y \\ k + \frac{\tau_y}{\dot{\gamma}}, & \text{when } \tau_m \geq \tau_y \end{cases} \quad (3.36)$$

where τ_m is the maximum shear stress in the fluid.

3.2.2 Fibre orientation distribution

Fibres a suspension can be described by their distribution with regards to position and orientation in space, with the probability density function (pdf) $\Psi(\mathbf{x}, \mathbf{p}, t)$ (Zhang, 2014). The pdf $\Psi(\mathbf{x}, \mathbf{p}, t)$ describes the probability to find a fibre with position between \mathbf{x} and $d\mathbf{x}$ with orientation vector between \mathbf{p} and $d\mathbf{p}$ at time t . The evolution of Ψ may be described by a transport equation, called a Fokker-Planck equation, as (Zhang, 2014)

$$\frac{\partial}{\partial t} \Psi(\mathbf{p}, \mathbf{x}, t) + \nabla_{\mathbf{p}} \cdot \mathbf{F}_{\mathbf{p}} + \nabla_{\mathbf{x}} \cdot \mathbf{F}_{\mathbf{x}} = 0 \quad (3.37)$$

where $\nabla_{\mathbf{p}}$ and $\nabla_{\mathbf{x}}$ are the gradient operators in rotational space and translational space, respectively. The flux densities in Equation (3.37) are defined as (Zhang, 2014)

$$\mathbf{F}_{\mathbf{p}} = \dot{\mathbf{p}}(\mathbf{p}, \mathbf{x}, t) \Psi(\mathbf{p}, \mathbf{x}, t) - D_{\mathbf{p}} \cdot \nabla_{\mathbf{p}} \Psi(\mathbf{p}, \mathbf{x}, t), \quad (3.38)$$

$$\mathbf{F}_{\mathbf{x}} = \dot{\mathbf{x}}(\mathbf{p}, \mathbf{x}, t) \Psi(\mathbf{p}, \mathbf{x}, t) - D_{\mathbf{x}} \cdot \nabla_{\mathbf{x}} \Psi(\mathbf{p}, \mathbf{x}, t), \quad (3.39)$$

where $\dot{\mathbf{p}}$ and $\dot{\mathbf{x}}$ are called the rotational and translational drift coefficients, respectively, and represents collective rotational and translational motion, respectively, of fibres in the suspension. If fibre concentration is homogeneous the distribution is uniform with respect position, since the probability of finding a fibre is the same for all positions, and Ψ is a non-uniform distribution solely for fibre orientation.

A coupling between the fibre orientation distribution function, from here on denoted the ODF, $\Psi(\mathbf{p})$ and the fluid momentum equations can be introduced through a constitutive

equation for viscous stresses in the suspension. Assuming high aspect ratio rigid fibres the stresses in the fibre suspension are (Shaqfeh & Fredrickson, 1990)

$$\tau_{ij} = 2\mu S_{ij} + \mu_f \left(a_{ijkl} - \frac{1}{3} \delta_{ij} a_{kl} \right) S_{kl} \quad (3.40)$$

where μ_f is called the additional viscosity due to presence of fibres. The tensors a_{ij} and a_{ijkl} are the second and fourth order statistical moments of the fibre orientation distribution:

$$a_{ij} = \langle p_i p_j \rangle_\Psi, \quad (3.41)$$

$$a_{ijkl} = \langle p_i p_j p_k p_l \rangle_\Psi, \quad (3.42)$$

where $\langle \cdot \rangle_\Psi$ denotes averaging with respect to the orientation distribution and p_i is the orientation vector of a fibre.

3.3 Experimental measurements of fibre suspensions

Data from experimental measurements of fibre suspension flows was used to validate simulations with the fibre models. In this section two articles on experimental measurements are covered. The first article provides experimental data from fibre suspension flow in a channel with a backwards facing step, a flow case featuring recirculating flow and decaying turbulence, much like the venturi geometry in the main project (Lundberg et al., 2015). The second article is on the turbulent fibre suspension flow in a rectangular channel where turbulent boundary layers are of importance for the flow. Graphical data from experimental measurements in the literature shown in this section were read graphically using a Matlab script that was created for the purpose. In short, the Matlab script was designed in a way so that the user may click on points of plotted data in a coordinate system and then save them to a data file.

3.3.1 Fibre suspension flow over a backwards facing step.

Claesson et al (2012) studied the flow of fibre suspensions over a backward facing step using Laser Doppler Anemometry (LDA). In the experiments the flow entered from a circular pipe with diameter 40 mm which was expanded and connected to a quadratic channel with side 40mm. A backwards facing step was created by inserting a block at the entrance of the quadratic channel. Two different step heights, 5mm and 10mm, were used. Mass concentrations 1%, 1.5%, 2% and 3% were used and the pulp was fully bleached never-dried kraft pulp provided by Södra Cell Värö in Sweden.

Instantaneous velocities were measured for flows with all different concentrations and at two free stream velocities, 1.3m/s and 1.8m/s. For free stream velocity 1.3m/s and mass consistency 1.5 % the profiles of mean streamwise velocity and turbulent intensity were shown in the article. Turbulent intensity I was defined as the average velocity fluctuation magnitude u'_{RMS} normalised by bulk velocity U_B computed as

$$I = \frac{u'_{\text{RMS}}}{U_B} = \frac{1}{U_B} \sqrt{\frac{\sum_{n=1}^N (u_n - \bar{u})^2}{N}} \quad (3.43)$$

where N is the number of instantaneous measurements, u_n the instantaneous streamwise velocity in measurement n and \bar{u} the mean streamwise velocity. The bulk velocity U_B was taken as the mean streamwise velocity at the step and at height 20mm. The recirculation zone for all flow cases were visualized by the level curve $\bar{u} = 0$. For step height 10mm, profiles of mean streamwise velocity for mass concentration 1.5% and free stream velocity 1.3m/s can be seen in Figure 3.2 and corresponding profiles of turbulent intensity can be seen in Figure 3.3. The peak in turbulent intensity that can be seen, roughly at the height of the step, is referred to as the mixing layer in Claesson et al. (2012). The recirculation zones can be seen in Figure 3.4 for mass concentrations 1%, 1.5% and for pure water, both for step height 10mm.

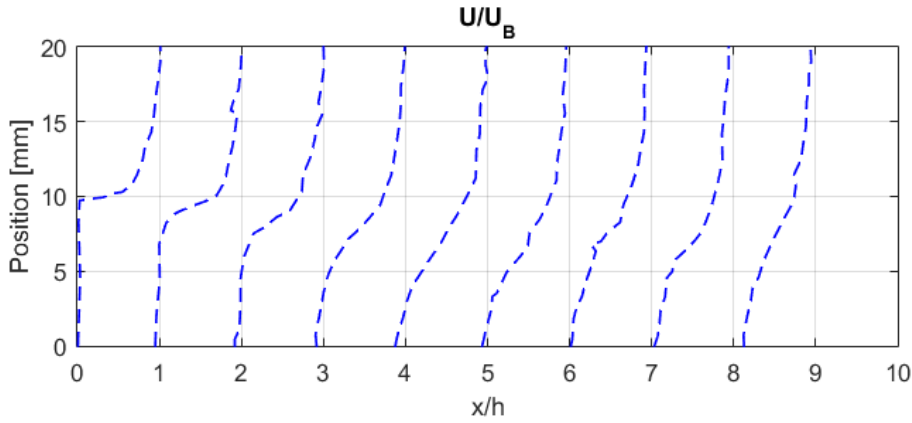


Figure 3.2: Mean streamwise velocity profiles for fibre suspension with free stream velocity 1.3m/s and mass consistency 1.5% read graphically from experimental data in Claesson et al. (2012).

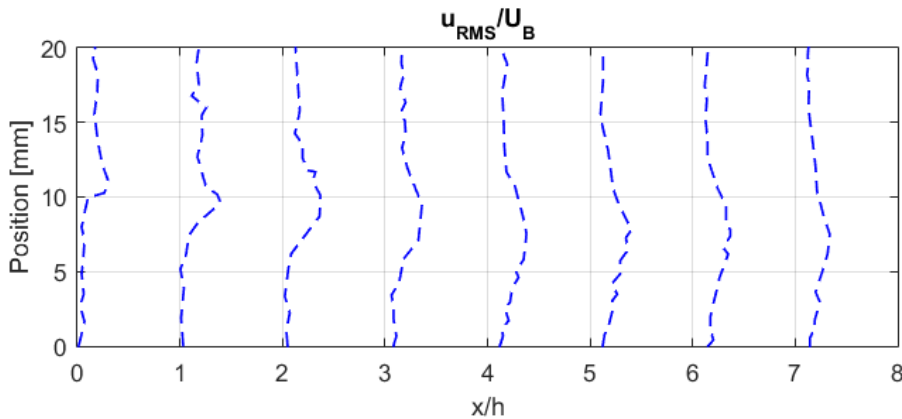


Figure 3.3: Turbulent intensity profiles for fibre suspension with free stream velocity 1.3m/s and mass consistency 1.5% read graphically from experimental data in Claesson et al. (2012).

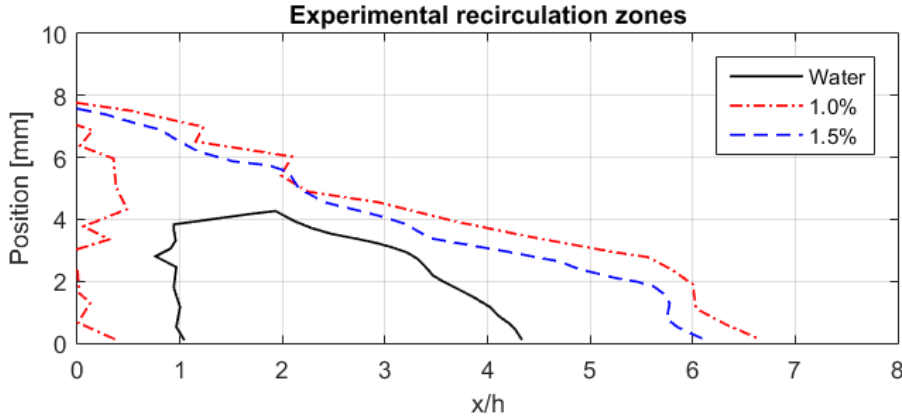


Figure 3.4: Recirculation zones as the level curve of mean streamwise velocity $\bar{u} = 0$ for free stream velocity 1.3m/s read graphically from experimental data in Claesson et al. (2012).

3.3.2 Fibre suspension flow in rectangular channel

Xu & Aidun (2005) measured velocity and turbulent intensity for turbulent fibre suspension flow with different mass concentrations and flow rates in a rectangular channel. Measurements were made using pulsed ultrasonic Doppler velocimetry (PUDV). Cellulose wood fibres, with average length and diameter $2,3\text{ mm}$ and $35\text{ }\mu\text{m}$, respectively, were used and mass concentrations ranged from $0.05\text{ }\%$ to $1.0\text{ }\%$. The fibres were assumed to have the same density as water in the experiments, since they were totally soaked, so that mass concentration and volume concentration were equal.

Inlet velocities used ranged from 0.16 m/s to 7.0 m/s and the corresponding Reynolds number based on pure water ranged from $2,000$ to $92,000$. The rectangular channel was 50.8 mm wide, 16.5 mm high and $1,500\text{ mm}$ long and measurements were made close to the outlet. Mean velocities and turbulent intensities were plotted along the height-direction in the channel. As a result of the measurements an empirical relation for the velocity profile in the channel was found as

$$u^+ = \frac{1}{0.41} \ln(y^+) + 4.69 + \frac{\Pi}{0.41} \sin^2\left(\frac{y}{0.9b} \Pi\right) \quad (3.44)$$

where y is wall distance, b is channel height, y^+ and u^+ are non-dimensional wall distance and velocity, respectively. The coefficient Π was called the wake coefficient, defined as

$$\Pi = 0.98e^{0.14nl^3 - 1.9 \cdot 10^{-5} \text{Re}} \quad (3.45)$$

where Re is the Reynolds number, n the fibre number density and l the fibre half-length. The authors came to the conclusion that the higher the flow rate the lower the effect of fibre concentration is on the velocity profiles. For sufficiently high flow rate velocity profiles of pure water and fibre suspensions were practically the same.

3.4 Disc refiners

In mechanical pulping processes so-called disc refiners are used to process cellulose fibres mechanically between rotating discs patterned with bars and grooves. Fibre suspension enters at the centre of the refining discs and is then forced towards the periphery by centrifugal forces and the fibres are processed by passing over the bars and through the grooves. A rotating disc is called rotor, a non-rotating disc is called stator and the distance between rotor and stator is called gap clearance. In low consistency refining, meaning where the fibre consistency or mass concentration is below 6%, the gap clearance can have length on the same order as a few fibre diameters. (Rajabi Nasab et al., 2014)

A sketch of the disc refiner concept is shown in Figure 3.5. In the figure the sizes of gap clearance and bars have been exaggerated for comprehensibility. In reality the bars and the grooves between them have width and height on the scale of a few millimetres (Rajabi Nasab et al., 2014).

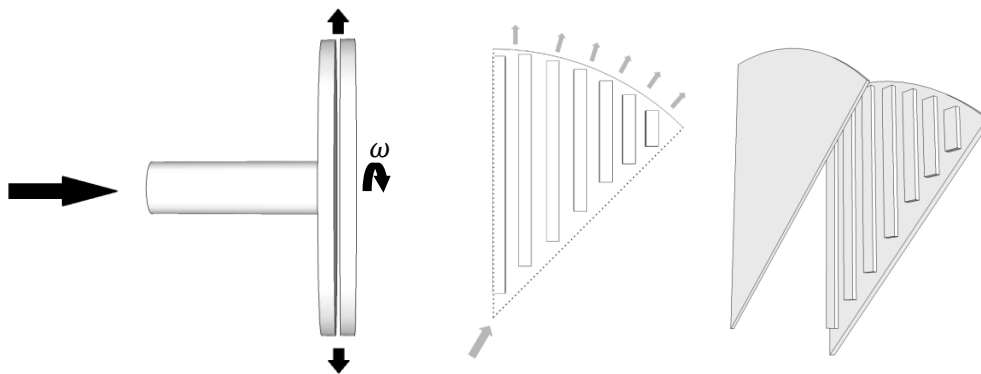


Figure 3.5: Sketch of disc refiner showing the concept of inlet and rotor movement (left), the concept of bars on the disc (middle) and the concept of stator and rotor discs (right). The size of gap clearance and bars are exaggerated.

4

Method

In this section the methodology for the thesis work is presented. In summary, the work consisted of conducting a literature survey providing a theoretical background and an overview of fibre modelling. Two approaches for modelling were chosen for implementation and, if possible, further development and the models were implemented in Fluent. The models were then validated using experimental data from literature. In the validation the models were optimised, in the sense that the best parameter setting was identified, using data from the flow over a backwards facing step. The models were then further validated using data from the flow in a rectangular channel. All simulations were performed using Fluent (ANSYS Inc. (b), 2013) and all mesh creation was made in ANSA (BETA CAE Systems S.A., 2014). After the validation one of the models were used to simulate the flow in a simplified disc refiner. The disc refiner simulation was performed as an example application for the fibre models and since it was of interest as a relevant flow case for pulp and paper industry.

4.1 Fibre modelling

Two fibre models, denoted the Bingham model and the ODF model, were implemented. The Bingham model was to a large part an implementation of modelling that can be found in literature, while the ODF model was mainly developed within this thesis. Both models effectively act as single-phase flow models in the sense that the Navier-Stokes equations are solved for a single phase with some modification of the viscous stress tensor. The single-phase property supposedly enhances the numerical stability of the models which was considered a desired property. The models were implemented in Fluent through so-called user-defined functions (UDF) which are sub-routines to the Fluent solver written in C programming language.

As discussed in Section 3.2 the rheology of fibre suspensions depend on many factors. Fibres of interest for the project were softwood fibres from pine and spruce, being a type of fibres commonly used in Swedish paper mills. Softwood pulp fibres have length on the millimetre scale and diameter on the order of tens of microns giving aspect ratio ~ 100 (Derakhshandeh et al., 2011). Fibre suspensions with mass concentration around 1% were mainly considered for modelling.

4.1.1 Bingham model

A method to numerically model fibre suspension flow with the Bingham viscoplastic fluid model was used by Fock et al. (2010). In this thesis work the implementation of the Bingham model followed a similar methodology. The yield stress for the suspension was computed using the empirical relation (Fock et al., 2010; Derakhshandeh et al., 2011; Kerekes, 2006)

$$\tau_y = aC_m^b \quad (4.1)$$

where a and b are model constants, varying from suspension to suspension, and C_m is the mass concentration, or mass consistency, of fibres. In the theoretical case for a Bingham viscoplastic fluid the effective viscosity is infinite for shear stress levels below the yield stress, which was stated in Equation (3.36). In a numerical model this may be approximated by assigning a large value to the viscosity for low shear rates and vary it linearly with shear rates corresponding to stress levels exceeding yield stress. That methodology, however, gives a discontinuity in the derivative $\partial\tau/\partial\dot{\gamma}$ which may cause numerical issues. Fock et al. (2010) used the Herschel-Bulkley model in Fluent to compute suspension viscosity as (ANSYS Inc. (b), 2013)

$$\mu = \begin{cases} \frac{\tau_y}{\dot{\gamma}_c} \left(2 - \frac{\dot{\gamma}}{\dot{\gamma}_c} \right) + k, & \dot{\gamma} \leq \dot{\gamma}_c \\ \frac{\tau_y}{\dot{\gamma}} + k, & \dot{\gamma} > \dot{\gamma}_c \end{cases} \quad (4.2)$$

where k is called consistency index which they set to the viscosity of water, $\dot{\gamma}_c$ is called critical strain rate, corresponding to the limit case were fluid shear stress equals the yield stress, and is computed as

$$\dot{\gamma}_c = \frac{\tau_y}{\mu_0}, \quad (4.3)$$

where they set the constant μ_0 to a large value. Equation (4.2) was used to compute the viscosity of the fibre suspension for the Bingham model also in this thesis work. It can be observed that the derivative of the viscosity with respect to shear rate yields

$$\left. \frac{\partial\mu}{\partial\dot{\gamma}} \right|_{\dot{\gamma}=\dot{\gamma}_c} = -\frac{\tau_y}{\dot{\gamma}_c^2}, \quad (4.4)$$

and is thus continuous, which also corresponds to a continuous derivative $\partial\tau/\partial\dot{\gamma}$. A comparison between the numerical model for the viscosity with discontinuous derivative and the modified version in the Herschel-Bulkley model is illustrated in Figure 4.1.

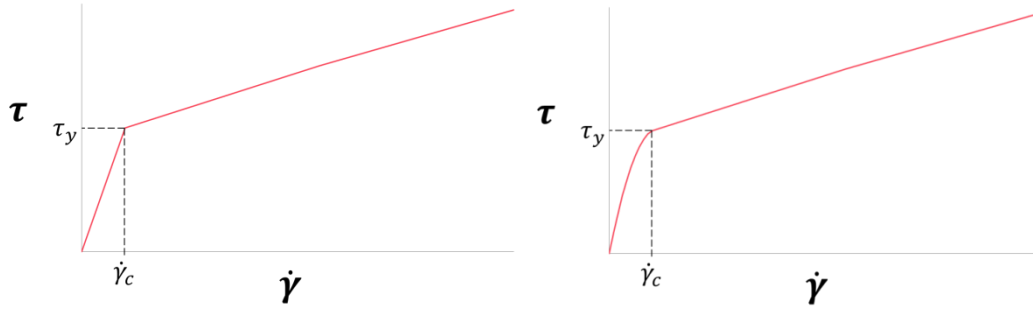


Figure 4.1: Illustration of the difference between discontinuous derivative (left) and continuous derivative (right) in the relationship between shear stress and shear rate in the fluid. Figures from the main project report (Lundberg et al., 2015).

The Herschel-Bulkley model in Fluent is not available for use in simulation of turbulent flows. In addition, according to Fock et al. (2010) the Bingham model is only valid for flows with low shear rates. In this work, however, the desired fibre model needed to be used also for simulations of turbulent fibre suspension flow. It was therefore decided to implement the model anyway and use validation with experimental data to evaluate if the use may be justified or not. To make it possible to use the model alongside turbulence models in Fluent the suspension viscosity was instead computed in each cell from Equation (4.2) using a UDF. In the flow model described in Fock et al. (2010) an additional transport equation was introduced to account for local variations in fibre mass concentration C_m , reading

$$\frac{\partial \rho C_m}{\partial t} + \frac{\partial}{\partial x_j} \left(\rho u_i - \Gamma \frac{\partial C_m}{\partial x_j} \right) = 0 \quad (4.5)$$

where Γ is fibre concentration diffusivity. In this thesis work, however, this transport was excluded. In the main project the model was tested for simulation in the designed venturi geometry. Both the case of homogenous concentration in the whole domain and the case of non-homogeneous inlet concentration together with the use of Equation (4.5) was tested. It was found that both cases yielded practically the same simulation results (Lundberg et al., 2015). Solving Equation (4.5) would therefore solely raise the computational cost and it was therefore concluded that the fibre concentration may and should be treated as homogeneous in this work.

4.1.2 ODF model

With intent to implement the coupling between fibre orientation and fluid momentum, described in Section 3.2.2, a model for the fibre orientation distribution function (ODF) was developed. The model was then used contrary to solving the probability transport from the Fokker-Planck equation (3.37). The modelled ODF was then used to construct explicit expressions for the fibre stresses τ_{ij}^f as a function of the flow field prior to simulations. Using the model no additional transport equation to the momentum and continuity equations needs to be solved. The idea behind the model was to use a statistical model for the ODF for an arbitrary flow field. Expressions for the orientation tensors,

needed to compute the fibre stresses, may then be constructed by computing the components numerically for the set of possible flow fields and fit a regression model the results. The model and its implementation are described below.

Modelling of the orientation distribution function

Lin et al. (2005) studied the ODF numerically in turbulent boundary layer flow and found that fibres aligned with the flow streamlines. Lin et al. (2011) numerically studied turbulent fibre suspension flow through an axisymmetric contraction and found that fibres aligned with flow direction, a result which was also validated with experimental data. In addition Lin et. al (2011) found that higher aspect ratio fibres aligned faster with flow direction and that turbulence had a randomising effect on the ODF, which increased in significance with the turbulent intensity of the flow. Olson et al. (2004) numerically studied the ODF for fibre suspension flowing in a planar contraction and found that fibres aligned in the flow direction, which was validated by experimental data. Similar numerical results for fibre suspension flow in a planar contraction were obtained by Krochak et al. (2009). Lin et al. (2012) simulated the ODF in a round turbulent jet of fibre suspension and found alignment with flow direction also in that flow, with more alignment for higher aspect ratio fibres. In summary, studies have shown that in turbulent flows suspended fibres align with flow direction and the alignment increases with aspect ratio. A sketch of the concept of fibres aligning with the streamlines of the fluid flow can be seen in Figure 4.2.

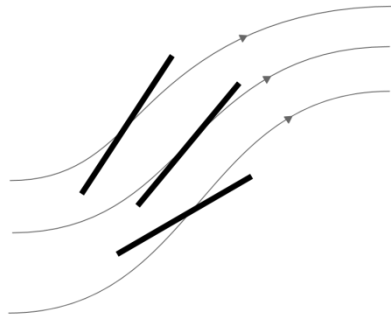


Figure 4.2: Suspended fibres aligning with streamlines of the fluid flow.

Starting with the assumption that fibres always align the flow direction, the goal was to develop a model where the ODF is approximated by a statistical mode centred about the flow direction. To describe fibre orientation a spherical coordinate system was applied, where the projected angle in the x - y plane is denoted ϕ and the angle between a fibre and the z -axis is denoted θ . The coordinate system can be seen in Figure 4.3.

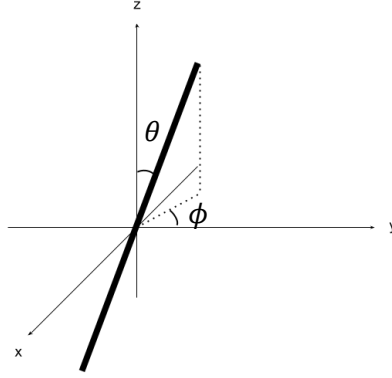


Figure 4.3: Spherical coordinates (ϕ, θ) used to describe fibre orientation.

In the Cartesian coordinate system the fibre orientation vector \mathbf{p} is related to the spherical coordinates as (Krochak et al., 2009)

$$\mathbf{p} = \begin{bmatrix} \cos \phi \sin \theta \\ \sin \phi \sin \theta \\ \cos \theta \end{bmatrix}. \quad (4.6)$$

Using the spherical coordinates the direction of the fluid flow was computed as

$$\bar{\phi} = \arctan\left(\frac{v}{u}\right), \quad (4.7)$$

$$\bar{\theta} = \arctan\left(\frac{w}{\sqrt{u^2 + v^2}}\right). \quad (4.8)$$

Equation (4.7) and Equation (4.8) yields angles the $\bar{\phi} \in \left[-\frac{\pi}{2}, \frac{\pi}{2}\right]$ and $\bar{\theta} \in \left[-\frac{\pi}{2}, \frac{\pi}{2}\right]$ and it may be seen from Figure 4.3 that the angles spans possible rotations of a fibres. The mean direction of fibres was then assumed to be $(\bar{\phi}, \bar{\theta})$. As a remark, it was assumed that the particle response time of fibres was small in comparison to the time-scale of changes in the flow field. The result is a small Stokes number, $St \ll 1$, implying that fibres follow changes in the flow with negligible delay (Crowe & Michaelides, 2006). Next, the ODF was modelled as a distribution about the flow direction by letting the fibre direction angles (ϕ, θ) have a bivariate normal distribution centred about $(\bar{\phi}, \bar{\theta})$. The probability density function, i.e. the modelled ODF, then reads (Rice, 2007)

$$\Psi(\phi, \theta) = \frac{1}{2\pi\sigma_\phi\sigma_\theta\sqrt{1-\xi^2}} e^{-\frac{1}{2(1-\xi^2)}\left[\frac{(\phi-\bar{\phi})^2}{\sigma_\phi^2} + \frac{(\theta-\bar{\theta})^2}{\sigma_\theta^2} - \frac{2\xi(\phi-\bar{\phi})(\theta-\bar{\theta})}{\sigma_\phi\sigma_\theta}\right]} \quad (4.9)$$

where σ_ϕ and σ_θ are the standard deviations for ϕ and θ , respectively, and ξ is the correlation between ϕ and θ . Since it strongly reduced the complexity of the model the respective variances for ϕ and θ were assumed equal and the correlation ξ was assumed to be zero. The standard deviation $\sigma = \sigma_\phi = \sigma_\theta$ will from here on be denoted the ODF standard deviation and σ^2 the ODF variance. Equation (4.9) was then rewritten as

$$\Psi(\phi, \theta) = \Psi_\phi(\phi) \cdot \Psi_\theta(\theta) \quad (4.10)$$

where $\Psi_\phi(\phi)$ and $\Psi_\theta(\theta)$ are the respective marginal distributions of ϕ and θ reading

$$\Psi_\phi(\phi) = \frac{1}{\sigma\sqrt{2\pi}} e^{-\frac{(\phi-\bar{\phi})^2}{2\sigma^2}}, \quad (4.11)$$

$$\Psi_\theta(\theta) = \frac{1}{\sigma\sqrt{2\pi}} e^{-\frac{(\theta-\bar{\theta})^2}{2\sigma^2}}. \quad (4.12)$$

It can be observed that Equation (4.11) and Equation (4.12) are the probability density functions for ϕ and θ being independently normally distributed random variables (Rice, 2007). In other words,

$$\phi \sim N(\bar{\phi}, \sigma^2), \quad (4.13)$$

$$\theta \sim N(\bar{\theta}, \sigma^2). \quad (4.14)$$

A visualisation of the modelled ODF is shown in Figure 4.4. The choice of ODF standard deviation σ is discussed below.

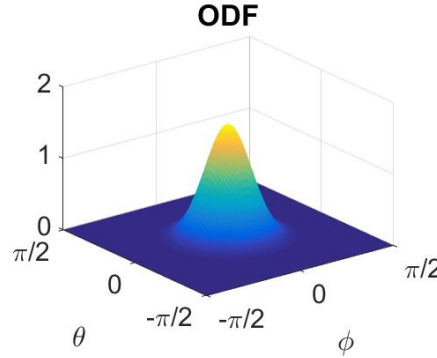


Figure 4.4: Fibre orientation distribution function (ODF) modelled as a bivariate normal distribution with zero correlation.

ODF standard deviation

A possible choice of ODF standard deviation was to set it constant and assume it to be homogeneous throughout the flow. Another possibility was that it rather would depend on the flow in some way. It therefore was assumed that the ODF standard deviation should increase with the magnitude of turbulent velocity fluctuations, inspired by the results from Lin et al. (2011). The ODF standard deviation was thus assumed to vary with turbulent intensity I , computed from the turbulent kinetic energy k as

$$I = \frac{1}{U_B} \sqrt{\frac{2}{3}k} \quad (4.15)$$

where U_B is the bulk velocity for the flow. Being a simple form of variation, a linear function was used relate the ODF standard deviation to the turbulent intensity. The ODF standard deviation σ was then computed as

$$\sigma = m \cdot I \quad (4.16)$$

where m is the slope of the linear function. A minimum value $\sigma_0 > 0$ was also introduced to prevent the fibres to perfectly align assuming it being non-realistic. Above the minimum σ varies linearly according to Equation (4.16).

A priori computation of fibre orientation tensors

The fibre orientation tensors of second and fourth order, respectively, can be computed from the integrals (Yang et al., 2013)

$$a_{ij} = \oint p_i p_j \Psi(\mathbf{p}) d\mathbf{p}, \quad (4.17)$$

$$a_{ijkl} = \oint p_i p_j p_k p_l \Psi(\mathbf{p}) d\mathbf{p}, \quad (4.18)$$

where p_i is component i of the fibre orientation vector \mathbf{p} and the integrals are taken over all possible rotations. It should be remarked that general second and fourth order tensors have $3^2 = 9$ and $3^4 = 81$ components, respectively. However, it can be seen that because of symmetries a_{ij} has 6 unique components and a_{ijkl} has 15 unique components. Now, since the modelled ODF is known for an arbitrary flow field the fibre orientation tensors a_{ij} and a_{ijkl} may be computed numerically for all possible flow directions prior to simulations. Explicit expressions for all tensor components as functions of $\bar{\phi}$ and $\bar{\theta}$ may then be constructed by fitting a regression model to the computed values and the expressions can be used to compute the tensor components as functions of the flow field in simulations. For instance, components of the second order orientation tensor could be computed from Equation (4.17) for given flow direction $(\bar{\phi}, \bar{\theta})$ as

$$\begin{aligned} a_{ij} &= \iint f(\phi) g(\theta) \Psi d\phi d\theta = \left(\int f(\phi) \Psi_\phi(\phi) d\phi \right) \cdot \left(\int g(\theta) \Psi_\theta(\theta) d\theta \right) \\ &:= F(\bar{\phi}) \cdot G(\bar{\theta}) \end{aligned} \quad (4.19)$$

where $f(\phi)$ and $g(\theta)$ denotes the ϕ - and θ -parts, respectively, of the combined fibre direction vectors according to

$$p_i p_j = f(\phi) g(\theta). \quad (4.20)$$

All components a_{ij} and a_{ijkl} can be computed analogously. Note that the reason $F(\bar{\phi})$ and $G(\bar{\theta})$ are functions of the flow direction coordinates $\bar{\phi}$ and $\bar{\theta}$, respectively, is since the marginal distribution functions Ψ_ϕ and Ψ_θ are determined by those coordinates.

For series of discrete values $\bar{\phi} \in \left[-\frac{\pi}{2}, \frac{\pi}{2}\right]$ and $\bar{\theta} \in \left[-\frac{\pi}{2}, \frac{\pi}{2}\right]$, and for given ODF standard deviation σ , $F(\bar{\phi})$ and $G(\bar{\theta})$ were computed as described for all unique components of

the fibre orientation tensors by numerical integration of Equation (4.17) and Equation (4.18). As regression model to construct explicit expressions for the tensor components Fourier series expansions then was applied, approximating $F(\bar{\phi})$ and $G(\bar{\theta})$ as (Nordling & Österman, 2006)

$$F(\bar{\phi}) \approx \bar{F}(\bar{\phi}) := \frac{a_0}{2} + \sum_{n=1}^N \left(a_n \cos \frac{n\pi\bar{\phi}}{L} + b_n \sin \frac{n\pi\bar{\phi}}{L} \right), \quad (4.21)$$

$$G(\bar{\theta}) \approx \bar{G}(\bar{\theta}) := \frac{c_0}{2} + \sum_{n=1}^M \left(c_n \cos \frac{n\pi\bar{\theta}}{L} + d_n \sin \frac{n\pi\bar{\theta}}{L} \right), \quad (4.22)$$

where L is length of the intervals for $\bar{\phi}$ and $\bar{\theta}$, respectively, i.e. $L = \pi$. The number of terms needed in the sums N and M , respectively, was only up to 3 to obtain approximations that resembled the computed values very well. The expressions for the orientation tensor components constructed by multiplying $\bar{F}(\bar{\phi})$ and $\bar{G}(\bar{\theta})$. In Figure 4.5 the numerically computed values and the fitted Fourier series can be seen for the fourth order orientation tensor component a_{1123} as an example. In Figure 4.6 the same tensor component, $a_{1123} = \bar{F}(\bar{\phi}) \cdot \bar{G}(\bar{\theta})$, is shown in 2-D. It can be observed that the Fourier series expressions practically match the computed values. Similar good agreement was found for all components a_{ij} and a_{ijkl} and for the range of σ used.

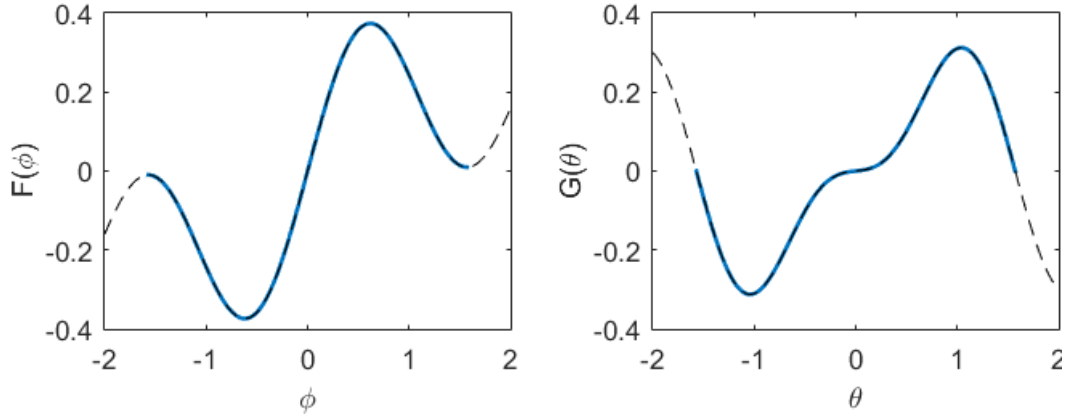


Figure 4.5: Computed values(—) and Fourier series value (--) of $F(\bar{\phi})$ (left) and $G(\bar{\theta})$ (right) for the fourth order orientation tensor component a_{1123} . ODF standard deviation $\sigma = 0.1$ rad.

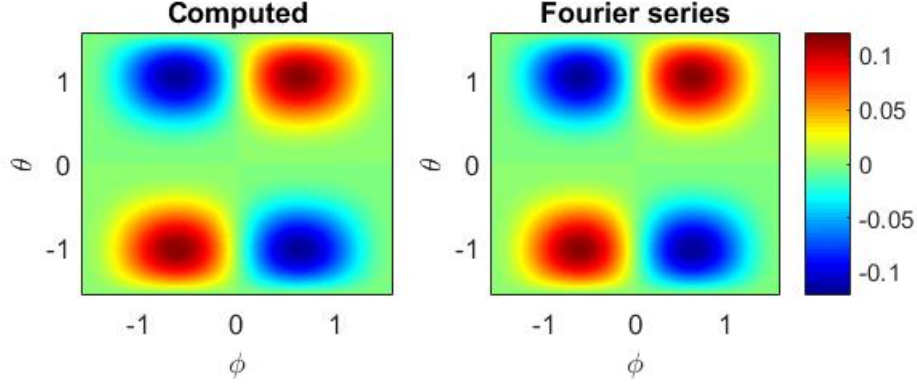


Figure 4.6: Component a_{1123} of the fourth order orientation tensor computed from numerical integration (left) and Fourier series expression (right) with ODF standard deviation $\sigma = 0.1$ rad

A Matlab script was used to compute the components of the fibre orientation tensors. In addition to computing and fitting of Fourier series the script also printed the expressions in C programming language to the Matlab console so that they could be copied directly into a Fluent UDF source code. For the case of non-homogeneous ODF standard deviation local values of the orientation tensor components were computed using linear interpolation. Fourier series expressions were constructed as described for a series discrete values of σ as

$$\sigma_0 < \sigma_1 < \dots < \sigma_n \quad (4.23)$$

and a total of $n = 10$ discrete values were used. The local values the orientation tensor components were then computed using linear interpolation between constructed expressions. The maximum value $\sigma_n = 0.5$ was used and was chosen as a value to cover an upper bound on σ with a certain margin. The value was based on results on the ODF in the literature (Lin et al., 2005; Lin et al., 2011; Olson et al., 2004; Lin et al., 2012; Kerekes, 2006). As a remark, the fibres of interest for this thesis work were of larger aspect ratio than the ones in the mentioned literature which should reduce the maximum value of σ further.

Coupling to fluid momentum

Using the constitutive equation for viscous stresses in a fibre suspension, Equation (3.40), the ODF was effectively coupled to the fluid momentum equations by an anisotropic modification of the viscous stress tensor through an additional fibre stress tensor τ_{ij}^f as

$$\tau_{ij} = 2\mu S_{ij} + \tau_{ij}^f = 2\mu S_{ij} + \mu_f \left(a_{ijkl} - \frac{1}{3} \delta_{ij} a_{kl} \right) S_{kl}, \quad (4.24)$$

which leads to a modified version of the incompressible Navier-Stokes equation (3.6) reading (Yang et al., 2013)

$$\frac{\partial u_i}{\partial t} + u_j \frac{\partial u_i}{\partial x_j} = -\frac{1}{\rho} \frac{\partial p}{\partial x_i} + \frac{\mu}{\rho} \frac{\partial^2 u_i}{\partial x_j \partial x_j} + \frac{\mu_f}{\rho} \frac{\partial}{\partial x_j} \left[a_{ijkl} S_{kl} - \frac{1}{3} (\delta_{ij} a_{kl}) S_{kl} \right]. \quad (4.25)$$

The body force term ρf_i was left out by Yang et al. (2013) but can, if desired, be included by adding it on the right hand side of Equation (4.25). Additional viscosity due to presence of fibres μ_f for a semi-dilute suspension of rigid slender ellipsoids was computed by using a relation derived by Shaqfeh & Fredrickson (1990) reading

$$\mu_f = \mu \frac{8\pi n l^3}{3 \left[\ln\left(\frac{1}{C_V}\right) + \ln\left(\ln\left(\frac{1}{C_V}\right)\right) + 1.4389 \right]} \quad (4.26)$$

where n is the number of fibres per unit volume, l the fibre half-length and C_V the volume fraction of fibres. Shaqfeh & Fredrickson (1990) defined semi-dilute concentration as the regime where $nl^3 \gg 1$ and $nl^2 d < 1$. Following, for completeness, it is motivated that this was the case for fibre suspensions of interest within this work. The volume concentration can be computed as the number of fibres per unit volume times volume of a fibre, i.e.

$$C_V = n \cdot \frac{\pi d^2}{4} \cdot 2l = n \cdot \frac{\pi}{4} \left(\frac{2l}{\beta}\right)^2 \cdot 2l = \frac{2\pi n l^3}{\beta^2} \quad (4.27)$$

where it was used that the aspect ratio $\beta = 2l/d$. An expression for nl^3 as a function of C_V and β can then be obtained from Equation (4.27) as

$$nl^3 = \frac{C_V \beta^2}{2\pi}. \quad (4.28)$$

An expression for $nl^2 d$ was also derived using Equation (4.28) as

$$nl^2 d = nl^2 d \cdot \frac{l}{l} = nl^3 \cdot \frac{d}{l} = nl^3 \cdot \frac{2}{\beta} = \frac{C_V \beta^2}{2\pi} \cdot \frac{2}{\beta} = \frac{C_V \beta}{\pi}. \quad (4.29)$$

Assuming $\beta = 100$ then $nl^2 d < 1$ for $C_V < \pi/\beta \approx 0.03$ and for $C_V = 0.03$ $nl^3 \approx 48$. In other words for fibres with aspect ratio $\beta = 100$ suspensions with volume concentration up to $\sim 3\%$ can be considered semi-dilute. If the aspect ratio is smaller the upper limit on C_V is even larger. The concentration regime thus covers up fibre suspensions of interest and it was considered justified to use the expression for μ_f as stated in Equation (4.26). Equation (4.26) was also rewritten to a function of C_V and β using Equation (4.28) as

$$\mu_f = \mu \frac{4\beta^2 C_V}{3 \left[\ln\left(\frac{1}{C_V}\right) + \ln\left(\ln\left(\frac{1}{C_V}\right)\right) + 1.4389 \right]}. \quad (4.30)$$

Since information on either β and C_V or n and l may be missing in some cases the model may contain uncertainties. It was therefore decided to introduce a constant, called D_f , to

account for this. The constant $D_f > 0$ was introduced in the expression for additional viscosity due to fibres and Equation (4.30) was thus modified as

$$\mu_f = \mu \cdot D_f \frac{4\beta^2 C_V}{3 \left[\ln\left(\frac{1}{C_V}\right) + \ln\left(\ln\left(\frac{1}{C_V}\right)\right) + 1.4389 \right]}. \quad (4.31)$$

Implementation in Fluent

A total of 4 UDF:s were used to implement the ODF model in Fluent. The methodology of the implementation was to compute the components of the orientation tensors from constructed expressions and use them to compute the components of the fibre stress tensor τ_{ij}^f . Then the divergence of the stresses, the last term in Equation (4.25), was added to the momentum equation in the respective directions as source terms. To store variables a total of 9 so-called user-defined scalars (UDS) in Fluent were used. UDS are additional transport equations for scalar variables defined by the user. UDS variables were allocated to store variables since Fluent automatically computes the gradient of each UDS variable, which were needed to compute the divergence of τ_{ij}^f . Solution of the transport equations for the UDS variables, however, was deactivated. The first UDF executes at the beginning of each iteration and its actions are listed below, namely

- computes the mean direction angles $\bar{\phi}$ and $\bar{\theta}$ from the flow field according to Equation (4.7) and Equation (4.8),
- computes ODF standard deviation σ (homogeneous or non-homogeneous),
- computes the components of the orientation tensors a_{ij} and a_{ijkl} ,
- computes the 6 unique components of the fibre stress tensor τ_{ij}^f in Equation (4.24) and stores in the 6 first UDS variables,
- obtains the gradient of the 6 first UDS variables,
- computes divergence $\mu_f \frac{\partial \tau_{ij}^f}{\partial x_j}$ from the last term in Equation (4.25) in the three momentum equations and stores in the remaining 3 UDS variables.

The remaining 3 UDFs adds the 3 last UDS variables as momentum sources in the x-, y-, and z-directions, respectively.

4.2 Comparison with experiments by Claesson et al (2012)

Data obtained from experimental measurements of fibre suspension flow in a channel with a backwards facing step obtained by Claesson et al. (Claesson et al., 2012) was used to validate the fibre models. The aim was identify the best performing settings and which parameters gave significant impact on the simulated results for the respective models. The experiments were considered suitable for the project since the flow geometry includes a recirculation zone after a sudden change in flow geometry, a flow characteristic relevant for the flow in the venturi nozzle. In addition pulp from a Swedish paper mill was used, which was the type of fibres of main interest for this work.

The first step consisted of creating a mesh to resemble experimental conditions sufficiently accurate in geometry and the second step consisted of simulations with fibre models. All simulations were made with the step height 10mm. This was made mainly since the most amount of data was available for the case. All simulations were performed using DES with $k - \omega$ SST turbulence model, the main reason being that the simulations on the venturi geometry were intended to be performed using the same turbulence model. The model is also accurate as a large part of the turbulence is resolved and not modelled. Since the simulations were performed to validate the fibre models it was preferred to minimise the sources of additional modelling errors as, for instance, turbulence modelling. Gravity was therefore also accounted for in the simulations. Simulations were carried out assuming isothermal conditions at temperature $20^{\circ}C$. The properties of water were then viscosity $\mu_w = 1.005\text{mPa} \cdot \text{s}$ and density $\rho_w = 998.2\text{kg/m}^3$ (Mörtstedt & Hellsten, 2010). The time step was chosen sufficiently small to satisfy the CFL condition $u\Delta t/\Delta x \leq 1$ in the mesh. Inlet velocity 1.3m/s was used in all simulations. The flow was simulated until stabilised and then averaged over about 0.5s. The turbulence was assumed to be sufficient for the fibre concentration to be homogeneous and $C_m = 1.5\%$ was used for the fibre models.

4.2.1 Mesh creation and fitting geometry

A first version mesh for the backwards facing step flow case was created. Simulations were then carried out for pure water with the same flow conditions as in the experimental measurements in Claesson et al. (2012). The computed and experimental recirculation zones were compared graphically the mesh was updated modified by increasing the geometry detail level. The process was repeated until good agreement with experimental data was found and in total three versions were created. All three meshes consisted of polyhedral cells and were constructed with boundary layers and cell sizes suitable for DES. A symmetry boundary was used at the channel centre line with respect to the spanwise direction, effectively reducing the number of cells in half.

Mesh version 1

Version 1 of the mesh consisted of a simple 3-D geometry of a backwards facing step flow. The mesh had a channel inlet with rectangular cross section of height 30mm and width 40mm and at 150mm downstream distance from the inlet the flow encounters the step. The distance from the inlet to the step was to allow for the flow to develop. The mesh consisted of around 180,000 cells and can be seen in Figure 4.7. Simulations with water on version 1 of the mesh resulted in poor resemblance with the experimental recirculation zone. More detail on the results is presented in Section 5.1.1.

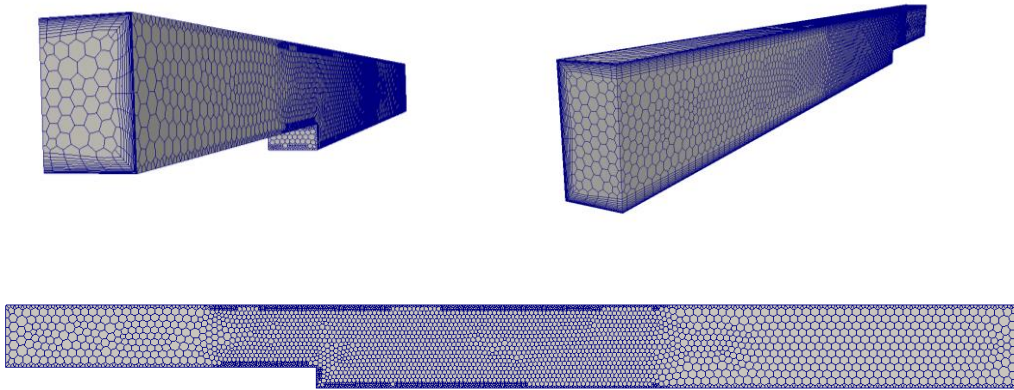


Figure 4.7: Backwards facing step mesh version 1.

Mesh version 2

A second version mesh was created by modifying version 1 and taking the flow before the step into account in higher detail. In the experiments performed by Claesson et al. (2012) the step was created by inserting a block with dimensions $40\text{ mm} \times 40\text{ mm} \times 10\text{ mm}$ in a quadratic channel with the side 40 mm . Mesh version 1 was therefore modified to a quadratic channel encountering an obstacle 110 mm downstream of the inlet. The distance from the inlet to the step, i.e. the expansion, was the same as for version 1. The mesh consisted of about 208.000 cells and can be seen in Figure 4.8. Simulations with water on the version 2 mesh produced results showing great improvement from the version 1 mesh. However, it was decided to increase the geometry detail further to resemble the experimental recirculation zone for water more closely. The results are presented in Section 5.1.1.

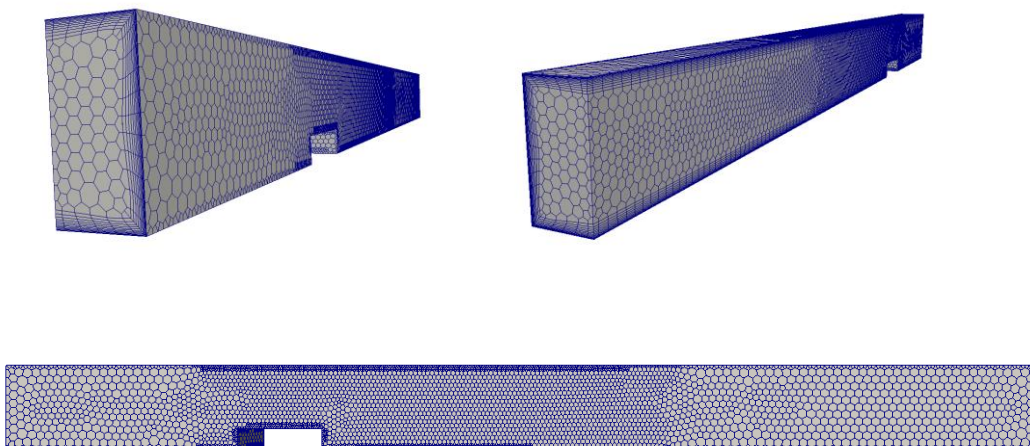


Figure 4.8: Backwards facing step mesh version 2.

Mesh version 3

In Claesson et al. (2012) the channel upstream of the step was not rectangular, but a pipe with circular cross section that was expanded and connected to the rectangular channel just upstream of the step. For the third version of the mesh this feature was included and the part upstream of the obstacle in version 2 was modified. In version 3 the upstream section instead consisted of a circular pipe with diameter 40mm. Then, starting at distance 80mm downstream of the inlet, the pipe diameter increased linearly over a streamwise length 30mm. The pipe then connected to the rectangular channel at the obstacle. As a remark, the information on how the pipe expanded and its final diameter was not given by Claesson et al. (2012) and had to be assumed. The mesh consisted of about 180.000 cells and can be seen in Figure 4.9. Simulations with water in the version 3 mesh yielded results resembling the experimental data better than version 2. It was decided that version 3 was sufficiently accurate to be used for the validation of the fibre models.

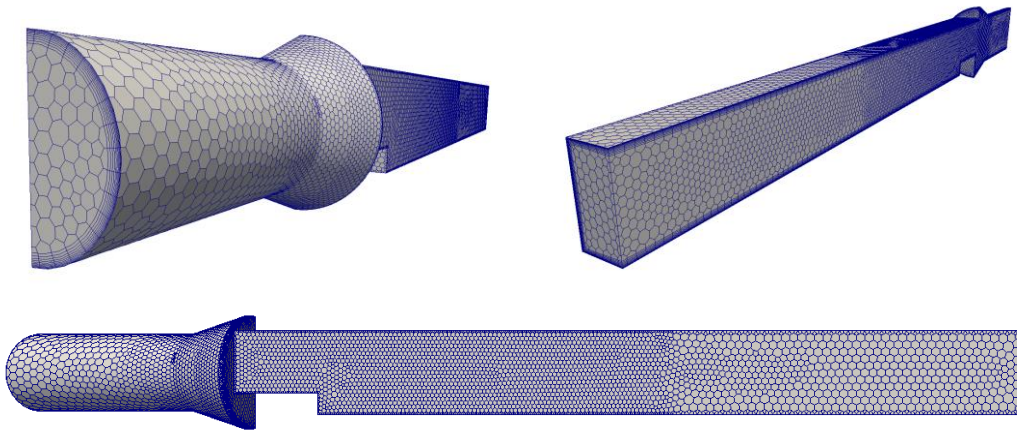


Figure 4.9: Backwards facing step mesh version 3.

4.2.2 Grid independence study

A grid independence study was conducted to confirm that the resolution of the mesh used for the simulations was sufficient. Two meshes of the same geometry as mesh version 3 with much lower and much higher resolution, respectively, were therefore created. The change in resolution was applied to all sections of the mesh, including boundary layers and the section around the step and the recirculating flow. The low resolution mesh consisted of around 34,500 cells and the high resolution mesh of around 434,000 cells. Simulations of water were performed on the low and high resolution meshes, respectively, for the same flow case as the simulations described in Section 4.2.1. Profiles of mean streamwise velocity and turbulent kinetic energy were plotted over the channel at three different distances downstream of the step and the pressure was plotted along the channel. The simulations indicated that the medium mesh, i.e. mesh version 3, had sufficient resolution. Detailed results are presented in Section 5.1.2.

4.2.3 Simulations with the Bingham model

The simulations with the Bingham model over the backwards facing step were initialized by starting from stabilised transient simulations of pure water using DES with $k - \omega$ SST turbulence model. Validation of the model was made in two separate steps. In the first step three combinations of the parameters a and b were tested, chosen based on the results in Derakhshandeh et al. (2010), to find the combination with best resemblance of experimental data. In this step the constant μ_0 was kept the same in with a value for was based on Ford et al. (2006). In the second step of the validation the effect on varying μ_0 by changing it a factor 2 up and down was studied, using the combination of a and b performing best in the first step. In total 5 parameter settings were used in the two steps which are listed in Table 4.1. The two validation steps are summarised in short below, namely

1. Vary a and b ,
2. Vary μ_0 .

Table 4.1: Parameter settings used for the Bingham model in the simulations of the backwards facing step flow.

Setting	B1	B2	B3	B4	B5
a [Pa]	810,000	495,000	222,000	222,000	222,000
b	2.50	2.33	1.95	1.95	1.95
μ_0 [Pa · s]	100	100	100	50	200

4.2.4 Simulations with the ODF model

Simulations on the backwards facing step using the ODF model were, in the same way as the Bingham model, initialised by starting from stabilised transient simulations of pure water using DES with $k - \omega$ SST turbulence model. In Claesson et al. (2012) the mass concentration of fibres was given but not the volume concentration. A relation between volume concentration C_V and mass concentration C_m was therefore desired since μ_f was computed from C_V and β . A relation was given in Derakhshandeh et al. (2011) as

$$C_V = C_m \left(\frac{1}{\rho_f} + \frac{X_w}{\rho_w} + V_L \right) \rho_b \quad (4.32)$$

where ρ_f is fibre density, X_w the amount of water absorbed in the fibre wall, ρ_w water density, V_L the volume of the hollow channel in the fibre per unit mass of fibre and ρ_b the bulk density. Assuming that the amount of water absorbed in the fibre wall and the hollow volume could instead be included in an approximation of the fibre density, Equation (4.32) was simplified as

$$C_V \approx \frac{\rho_{\text{tot}}}{\rho_f} C_m, \quad (4.33)$$

where $\rho_{\text{tot}} = \rho_f C_m + \rho_w (1 - C_m) \approx \rho_w$ because of the low fibre concentration. The density of the fibres ρ_f , however, was unknown and needed to be approximated with some assumption. In their experiments Claesson et al. (2012) used never-dried softwood pulp from a Swedish paper mill and it was therefore assumed that the pulp consisted of fibres from pine and spruce. The densities of the dry substance in wood from pine and spruce are 290 kg/m^3 and 285 kg/m^3 , respectively (Mörtstedt & Hellsten, 2010). Since the fibres were never-dried they had also absorbed a significant amount of water. It was, as a qualified guess, assumed that the fibre had absorbed water so that their moisture content was 50%. The fibre density was therefore approximated as the average of the dry density and the density of water, as

$$\rho_f \approx \frac{1}{2}(\rho_f + \rho_w) \approx \frac{1}{2}(1000 + 290) \text{ kg/m}^3 \approx 650 \text{ kg/m}^3. \quad (4.34)$$

Fibre aspect ratio in the experimental data, which was also needed to compute μ_f , was unknown but was assumed to $\beta \approx 50^1$. Validation of the ODF model was made in three steps. In the first step the flow was simulated for three different homogeneous ODF standard deviations. This was done so see if the model was at all feasible and if experimental data would be resembled to some extent. In these simulations the constant D_f was set to 1.0. In the second step the ODF standard deviation σ was computed as a linear function of turbulent intensity I , between the minimum and maximum values for σ , with three different slopes, namely 1.25, 2.5 and 5.0. The constant D_f was again set to 1.0 in the simulations. The linear functions with different slopes used can be seen in Figure 4.10

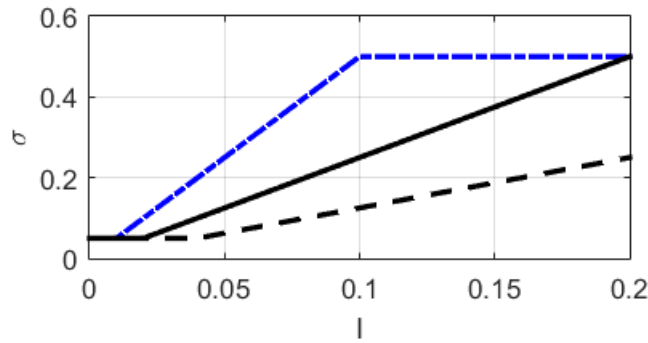


Figure 4.10: ODF standard deviation σ as linear function of turbulent intensity I with minimum 0.05 rad and maximum 0.5 rad computed as $\sigma = 1.25 \cdot I$ (—), $\sigma = 2.5 \cdot I$ (---) and $\sigma = 5.0 \cdot I$ (-·-).

¹ Originally the aspect ratio $\beta = 100$ was intended as motivated in Section 4.1. However, a miscalculation in the derivation of the expression for μ_f , i.e. Equation (4.30), led to that the simulations were effectively performed for fibres with aspect ratio $\beta = 50$. The error was found after all simulations were made.

In the third step the linear variation of σ was kept with the best slope from step 2. Two additional simulations with $D_f = 0.5$ and $D_f = 2.0$ were performed to test the impact on the results of varying the constant, thus testing how sensitive the model was to not having correct data on the fibre aspect ratio and volume concentration. All settings used to study the ODF model are listed in Table 4.2. The three steps of the study are summarised in short below, namely

1. Study different constant σ ,
2. Study $\sigma \propto I$ with different slopes,
3. Study sensitivity of varying D_f .

Table 4.2: Parameter settings used for the ODF-model in the simulations in the simulations of backwards facing step flow.

Setting	R1	R2	R3	R4	R5	R6	R7	R8
σ	0.10	0.25	0.05	$2.5 \cdot I$	$5.0 \cdot I$	$1.25 \cdot I$	$1.25 \cdot I$	$1.25 \cdot I$
D_f	1.0	1.0	1.0	1.0	1.0	1.0	2.0	0.5

4.3 Comparison with experiments by Xu & Aidun (2005)

The best performing settings for the Bingham model and the ODF model, respectively, from the study of the backwards facing step flow, described in Section 4.2, were used to simulate turbulent fibre suspension flow in a rectangular channel. The results were then compared to experimental data from Xu & Aidun (2005). A mesh of the channel used in the experiments was created. The mesh consisted of a 1500mm long channel of width of 50.8mm and height 16.5mm. Since the geometry was rectangular two symmetry boundaries was applied so that only a quarter of the channel needed to be simulated. The mesh was constructed with boundary layers and cell sizes suitable for DES. To ensure that the resolution of the mesh was sufficient it was ensured that the turbulent boundary layers were covered by at least 10 cells in the wall-normal directions. The condition serves as a guideline for turbulent flows resolved with RANS, which is the case for the boundary layers in DES (ANSYS Inc. (b), 2013). In addition it should be remarked that the geometry, the cells and the velocities were of similar order of magnitude for as the backwards facing step case, where a more thorough study on grid convergence study was conducted, described in Section 4.2.2. Further, the geometry of the rectangular channel was less complex than the backwards facing step. It was therefore decided not to conduct a full grid convergence study on mesh. The final mesh consisted of around 120,000 cells and can be seen in Figure 4.11.

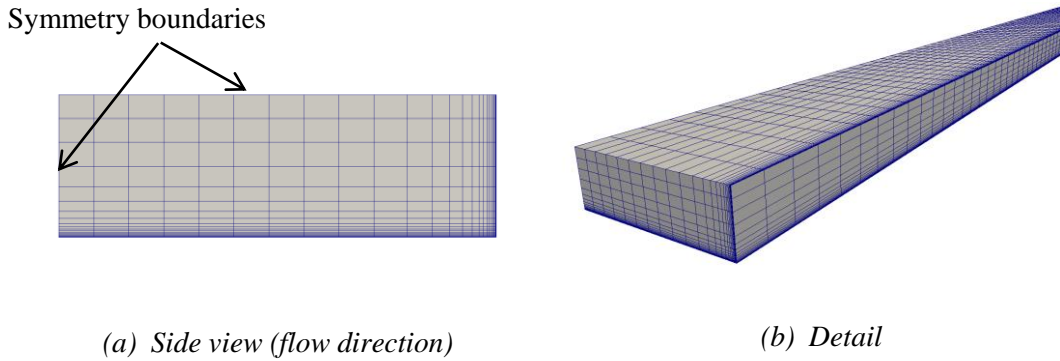


Figure 4.11: Mesh used for the turbulent fibre suspension flow in a rectangular channel. Figure from main project report (Lundberg et al., 2015).

Simulations were performed using DES with $k - \omega$ SST turbulence model. With the same motivation as for backwards facing step, described in Section 4.2, this was done since the simulations with the fibre models on the venturi geometry were intended to be performed using the same turbulence model. In addition, DES comes with small turbulence modelling errors because of its accuracy. The time step was chosen sufficiently small to satisfy the CFL condition $u\Delta t/\Delta x \leq 1$ in the mesh. Data on temperature conditions for the experimental setup was not given in Xu & Aidun (2005). However, the Reynolds number and flow rates presented corresponded to those for water at $10^\circ C$ giving dynamic viscosity $\nu = \mu/\rho_w = 1.308 \cdot 10^{-6}$ (Mörtstedt & Hellsten, 2010). The same conditions were therefore used in the simulations with the fibre models. For the Bingham model setting B3 was used and for the ODF model setting R6 was used, being the best settings for the respective models. Gravity was neglected in the simulations since the flow was not gravity driven and since the symmetry boundary in the direction of height would be invalid if gravity was included. Simulations were performed at the mass concentrations $C_m = 1\%$ and $C_m = 0.1\%$ and at Reynolds numbers 37,000 and 92,000 based on pure water.

The authors reported that the fibres had the same density as the water in the experiments as the fibres were fully soaked. The volume concentration in the ODF model was therefore set equal to the mass concentration in the simulations to compute μ_f , where fibre aspect ratio $\beta = 30$ used². Profiles of mean streamwise velocity \bar{u} and turbulent intensity I were plotted near the centre of the flow far downstream of the inlet where the flow was fully developed. This was chosen to match the measurement position from the experiments in Xu & Aidun (2005). Turbulent intensity was computed from turbulent kinetic energy k as

² Originally the aspect ratio $\beta = 60$ was intended, as it was given in Xu & Aidun (2005). However, a miscalculation in the derivation of the expression for μ_f , i.e. Equation (4.30), led to that the simulations were effectively performed for fibres with aspect ratio $\beta = 30$. The error was found after all simulations were made.

$$I = \frac{\overline{|u'|}}{\bar{u}_{\text{mean}}} = \frac{1}{\bar{u}_{\text{mean}}} \sqrt{\left(\frac{2}{3}k\right)} \quad (4.35)$$

where \bar{u}_{mean} is the mean streamwise velocity averaged over the channel height, as defined by Xu & Aidun (2005), computed as

$$\bar{u}_{\text{mean}} = \frac{1}{b/2} \int_0^{b/2} \bar{u} \, dy \quad (4.36)$$

where b is the height of the channel.

4.4 Disc refiner application

As example of an application for fibre models a in disc refiner was simulated with a simplified flow model. The geometry consisted of a single disc refiner groove and the best performing fibre model from the validation was used for the flow. The setup of the geometry was inspired by the method used in Prahl Wittberg et al. (2012) where the authors modelled the flow in a single disc refiner groove using CFD-simulations. In their model the relative motion between disc refiner stator and rotor was implemented with a moving wall as the top boundary and neighbouring grooves were realised with the use of periodic boundaries. Simulations were performed for laminar flow and experimental data from a model scale disc refiner was used for validation. (Prahl Wittberg et al., 2012)

A sketch of the concept with a single groove with periodic boundaries and a moving top plate can be seen in Figure 4.12. The same concept was used for the simulation in this thesis work.

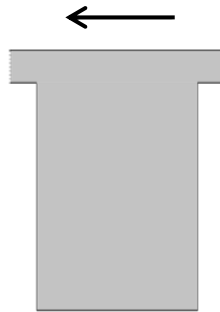


Figure 4.12: Concept of disc refiner single groove model with periodic boundaries to neighbouring grooves and a moving top wall, as seen from inlet.

4.4.1 Mesh

A mesh consisting of a groove of width 4 mm and height 8 mm was created. Relative motion between rotor and stator was implemented by a moving wall with a no slip condition at the top boundary. Connection to neighbouring grooves was modelled using periodic boundaries were used in the same way as in Prahl Wittberg et al. (2012). The gap clearance, i.e. the distance between stator and the rotor which in the mesh was the

distance between the bars and the moving wall, was 0.2 mm and the groove length was 100 mm. The mesh was constructed with polyhedral cells of sizes suitable for DES with boundary layers at the walls of the groove and at the part of the flat plate above the groove. To ensure that the resolution of the mesh was sufficient in the boundary layers it was ensured that they were covered by at least 10 cells in the wall-normal directions. The condition is a guideline for modelling of turbulent boundary layers resolved with RANS, as they are in DES (ANSYS Inc. (b), 2013). The mesh resolution was also similar to the backwards facing step mesh and the channel flow mesh and it was therefore decided not to conduct a more thorough grid convergence study.

The gap clearance between the bars and the moving top wall was only resolved by about 3 layers of cells. Such a low resolution will most certainly not be sufficient to capture a turbulent boundary layer near the top wall. However, assuming that fibres have diameter of approximately $20\mu\text{m}$ (Derakhshandeh et al., 2011), and with the gap clearance of 0.2mm, the gap is approximately 10 fibre diameters thick. The flow will therefore supposedly be significantly affected by small scale fibre effects that are not accounted for in the fibre model. The computed boundary layer will thus not be correct there even with high resolution. It was decided, however, to include the gap with the low resolution so that suspension can enter and exit from the groove at the periodic boundaries. The final mesh consisted of about 480,000 cells and can be seen in Figure 4.13.

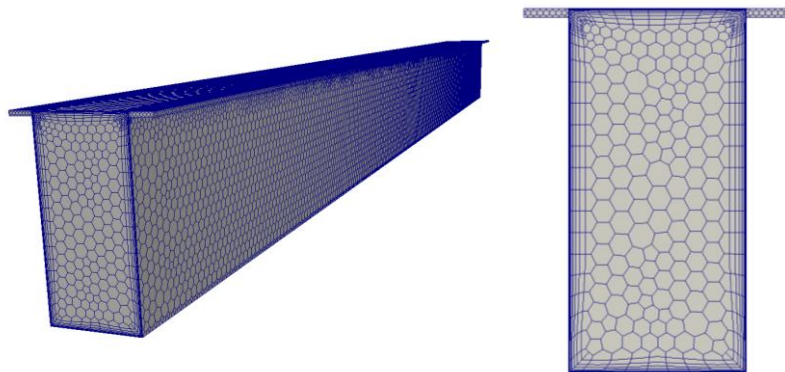


Figure 4.13: Mesh used for simulations of fibre suspension flow in a single disc refiner groove.

4.4.2 Simulations

In the simulations of the disc refiner the pressure was specified at inlet to 3bar and at outlet to 1bar. The pressure drop was chosen being one used in the numerical simulations performed by Prah Wittberg et al. (2012). With the same motivation the velocity for the moving wall was set to 18.6 m/s perpendicular to the flow direction, i.e. the direction from inlet to outlet. In the simulation the best performing Bingham model was used, corresponding to setting B3 in Table 4.1, since it was the one decided to be used also in the simulations on the venturi geometry in the main project (Lundberg et al., 2015). DES with the $k - \omega$ SST model was used as for the validation of fibre models. Before switching to the transient DES simulation the solution was initialised by solving the steady RANS equation with the $k - \omega$ SST turbulence model.

The time step was chosen to satisfy the CFL condition $v\Delta t/\Delta x \leq 1$ and the flow was simulated for approximately 10 throughputs. The flow quantities were then averaged over the last 5 throughputs where the flow was stabilised from initial transients resulting from the switch from steady to transient simulation.

5

Results

In this section the results from the simulations performed in the thesis work are presented and commented. Results from the simulations on the backwards facing step are covered followed by the simulations of the turbulent channel flow. Finally the results from the disc refiner simulation are presented.

5.1 Comparison with experiments by Claesson et al. (2012)

The recirculation zone, defined by the mean streamwise velocity $\bar{u} \leq 0$, was plotted with the corresponding experimental the curve $\bar{u} = 0$ downstream of the step. For the simulations with fibre models the profiles of mean streamwise velocity and turbulent intensity were also plotted along with the experimental profiles from Claesson et al. (2012). A visualisation of the lines along which profiles were plotted and the section of the recirculation zone can be seen in Figure 5.1. As a remark, the profiles were only plotted up to the height 20mm in the same way as the experimental profiles.

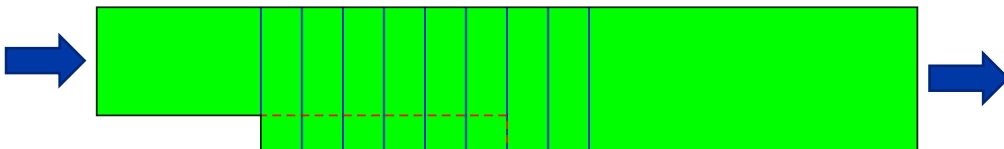


Figure 5.1: 2-D model of the backwards step with the lines used to compare computed profiles with experimental profiles (—) and the area where the recirculation zone was plotted (--).

The experimental data in Claesson et al. (2012) had been normalised with U_B , defined as the mean streamwise velocity at the step and at height 20 mm. The computed data was therefore normalised with U_B defined similarly from the simulations. Root mean square (RMS) errors from experimental profiles were computed both with respect to mean streamwise velocity and turbulent intensity. The RMS errors were computed by interpolating computed and experimental data, respectively, to 20 uniformly distributed points along the lines, up to height 20mm. They were then computed as

$$\text{Error} = \frac{1}{n_{\text{samples}}} \sum_{k=1}^{n_{\text{samples}}} (\alpha_k^{\text{comp}} - \alpha_k^{\text{exp}})^2 \quad (5.1)$$

where α_k^{comp} and α_k^{exp} denotes normalised computed and experimental quantities, respectively. The errors were used to compare the performances of different parameter settings.

5.1.1 Simulations with pure water

Simulations performed with pure water on the backwards facing step were used to tune the mesh geometry for the backwards facing step flow case. Results from the simulations from the three mesh versions are presented below.

Mesh version 1

The computed recirculation zone $\bar{u} \leq 1$ from mesh version 1 and the experimental level curve $\bar{u} = 0$ for water from Claesson et al. (2012) can be seen in Figure 5.2. It can be observed that the size of the recirculation zone is clearly overestimated by the simulations. The result indicates that the mesh geometry does not resemble the experimental geometry with sufficient accuracy.

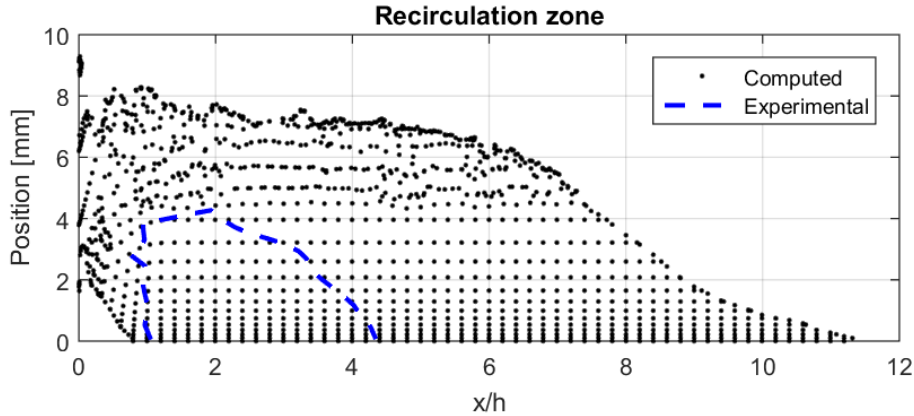


Figure 5.2: Computed recirculation zone, $\bar{u} \leq 0$, from simulations of pure water flow on mesh version 1 and experimental level curve $\bar{u} = 0$ from the experimental data in Claesson et al (2012).

Mesh version 2

The computed recirculation zone $\bar{u} \leq 0$ from mesh version 2 and the experimental level curve $\bar{u} = 0$ for water from Claesson et al. (2012) can be seen in Figure 5.3. It can be observed that the size of the computed recirculation zone is significantly improved compared to the one obtained using mesh version 1, which can be seen in Figure 5.2. The improvement is expected due to the increased detail level of the geometry. The computed zone does, however, yield a recirculation zone starting directly downstream of the wall, which is not seen in the experimental data. The results indicate that the geometry used to obtain the experimental data could be resembled even more accurately.

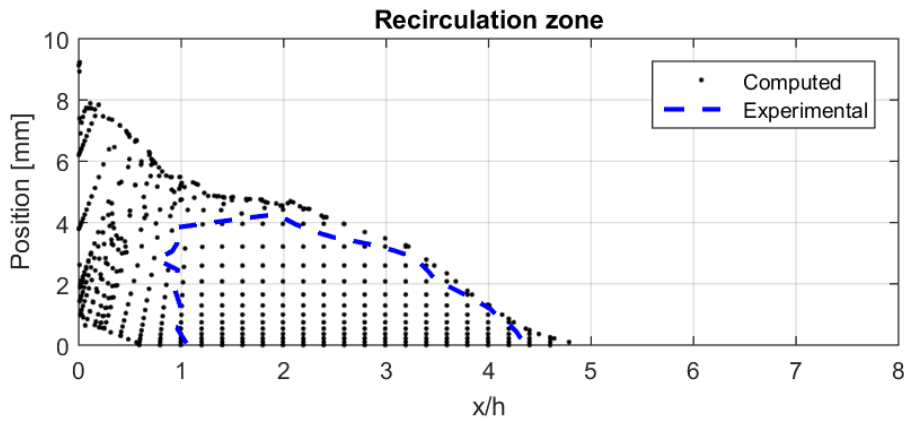


Figure 5.3: Computed recirculation zone, $\bar{u} \leq 0$, from simulations of pure water flow on mesh version 2 and experimental level curve $\bar{u} = 0$ from the experimental data in Claesson et al (2012).

Mesh version 3

Computed recirculation zone $\bar{u} \leq 0$ from mesh version 3 and the experimental level curve $\bar{u} = 0$ for water from Claesson et al. (2012) can be seen in Figure 5.4. An improvement compared to the zone from mesh version 2, which can be seen in Figure 5.3, can be observed as the part of the recirculation zone directly downstream of the step is not seen from mesh version 3. In the first part of the zone the height is slightly overestimated. The results obtained from mesh version 3, however, give the best resemblance of the experimental recirculation zone out of the three versions. This is expected since mesh version 3 has the highest level of detail in geometry.

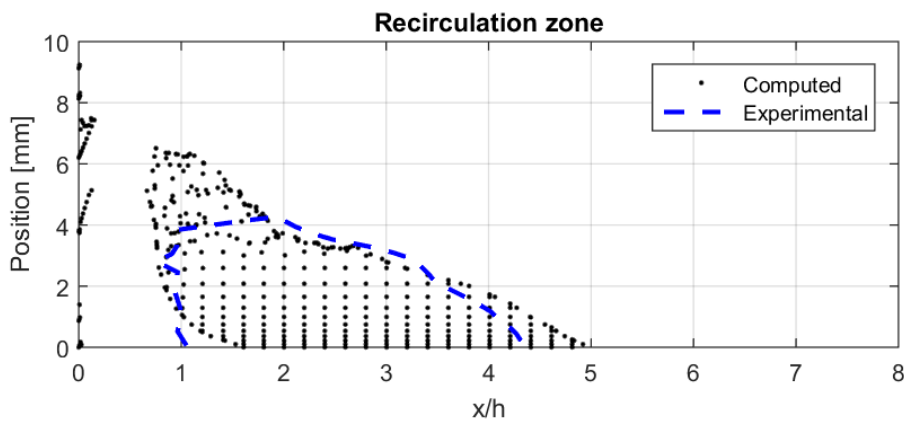


Figure 5.4: Computed recirculation zone, $\bar{u} \leq 0$, from simulations of pure water flow on mesh version 3 and experimental level curve $\bar{u} = 0$ from the experimental data in Claesson et al (2012).

5.1.2 Grid independence study

Computed profiles of mean streamwise velocity and turbulent kinetic energy at three different streamwise positions downstream of the step can be seen in Figure 5.5 and Figure 5.6, respectively, for the three mesh resolutions. The absolute pressure plotted

along the channel downstream of the step at height 25 mm can be seen in Figure 5.7. It can be seen in Figure 5.5 that the medium and high resolution grids give similar velocity profiles and the boundary layers are similar for the two meshes. For the low resolution mesh the velocity profiles differ from the two finer meshes. In Figure 5.6 it can be seen that the medium and fine meshes yield similar results on the turbulent kinetic energy while the coarse mesh gives a significantly different result. In Figure 5.7 it can be seen that the pressure is practically the same for the medium and high resolution meshes while the result differs in the low resolution mesh. Obtained results indicate that the medium resolution mesh with 180,000 cells has sufficient resolution and results obtained with the mesh may be considered grid independent.

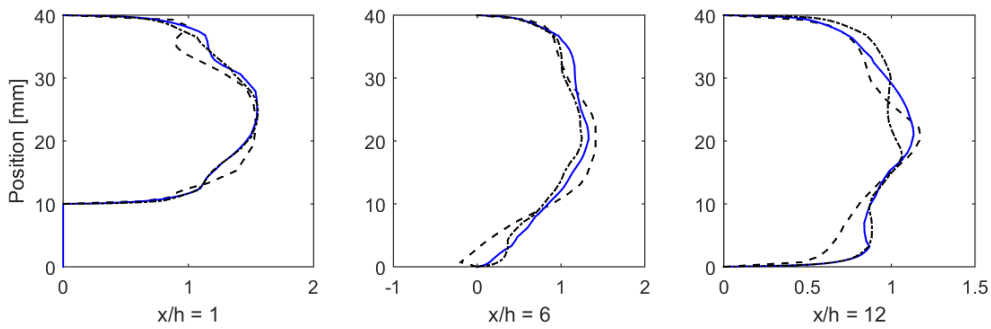


Figure 5.5: Computed profiles of mean streamwise velocity at three different streamwise positions using 34,500 cells (--), 180,000 cells (—) and 434,000 cells (-·-).

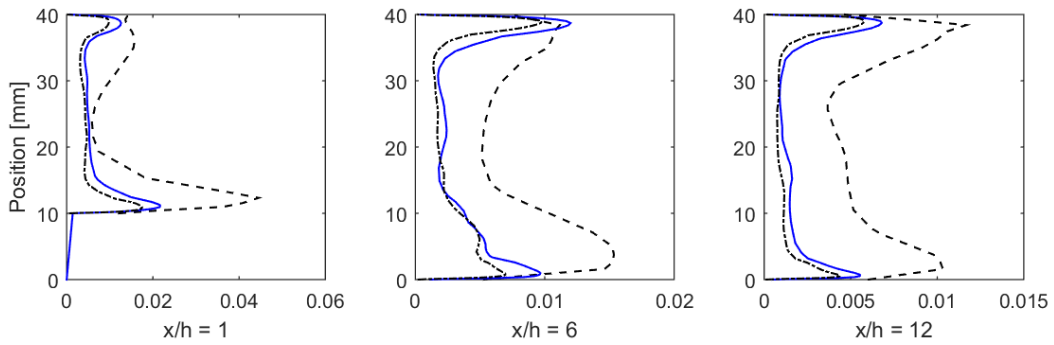


Figure 5.6: Computed profiles of turbulent kinetic energy at three different streamwise positions using 34,500 cells (--), 180,000 cells (—) and 434,000 cells (-·-).

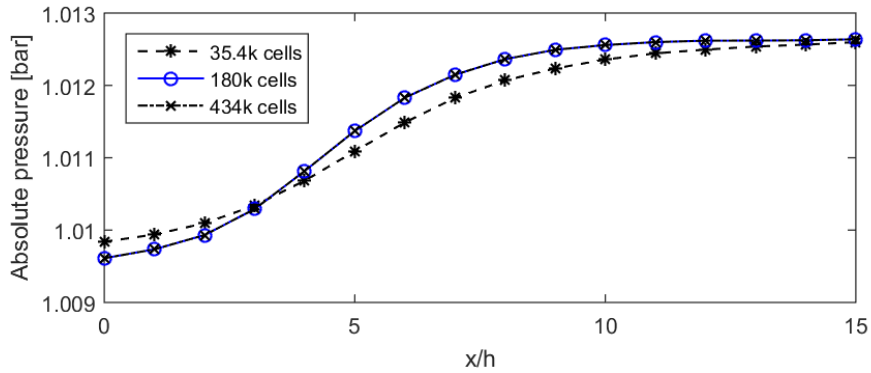


Figure 5.7: Computed pressure downstream of the step at height 25mm using 34,500 cells, 180,000 cells and 434,000 cells.

5.1.3 Simulations with the Bingham model

Results obtained from all simulations performed with the Bingham model are presented in this section. The results from each step of the validation study are first presented individually and then compared to simulations within the same step.

Bingham model with setting B1

Computed profiles of mean streamwise velocity for setting B1 can be seen together with corresponding experimental profiles in Figure 5.8. Computed profiles of turbulent intensity can be seen with corresponding experimental profiles in Figure 5.9. The computed recirculation zone $\bar{u} \leq 0$ can be seen together with the experimental level curve $\bar{u} = 0$ in Figure 5.10.

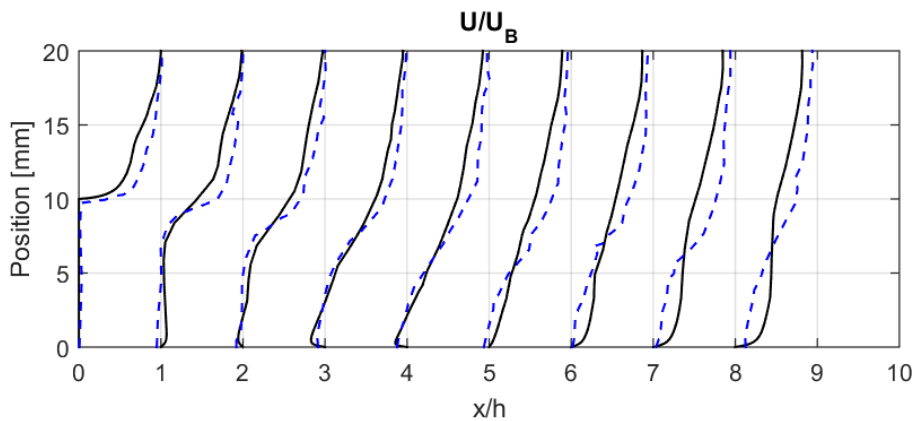


Figure 5.8: Computed profiles of mean streamwise velocity using the Bingham model setting B1 for mass consistency $C_m = 1.5\%$ (—) and corresponding experimental profiles from Claesson et al. (2012) (--).

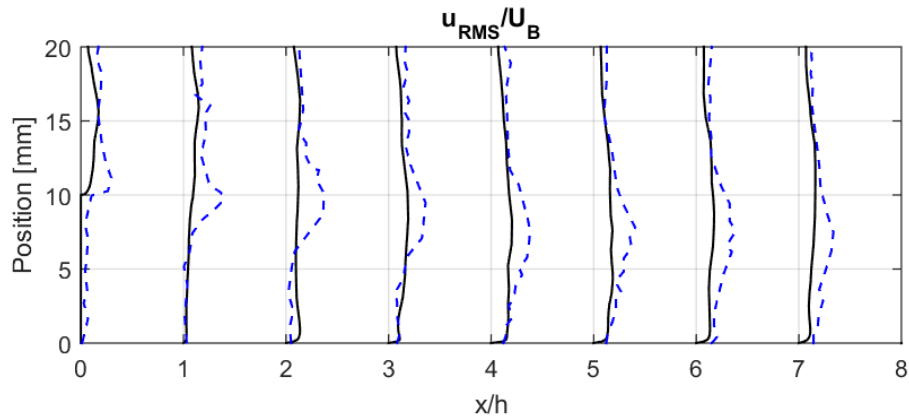


Figure 5.9: Computed profiles of turbulent intensity using the Bingham model setting B1 for mass consistency $C_m = 1.5\%$ (—) and corresponding experimental profiles from Claesson et al. (2012) (---).

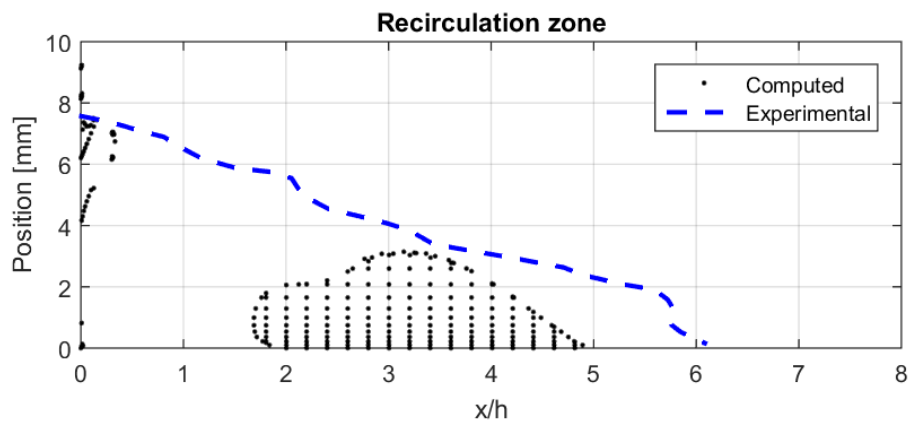


Figure 5.10: Computed recirculation zone, $\bar{u} \leq 0$, from simulations with the Bingham model setting B1 and experimental level curve $\bar{u} = 0$ from the experimental data in Claesson et al (2012).

Bingham model with setting B2

Computed profiles of mean streamwise velocity for setting B2 can be seen together with corresponding experimental profiles in Figure 5.11. Computed profiles of turbulent intensity can be seen with corresponding experimental profiles in Figure 5.12. The computed recirculation zone $\bar{u} \leq 0$ can be seen together with the experimental level curve $\bar{u} = 0$ in Figure 5.13.

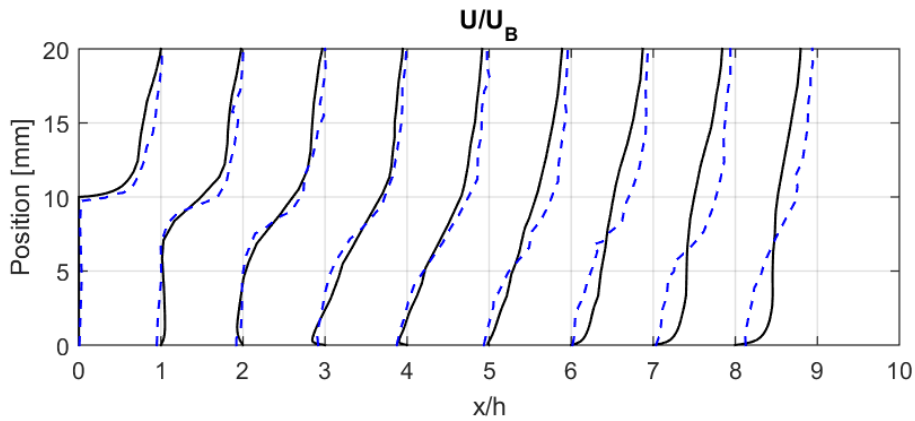


Figure 5.11: Computed profiles of mean streamwise velocity using the Bingham model setting B2 for mass consistency $C_m = 1.5\%$ (—) and corresponding experimental profiles from Claesson et al. (2012) (—).

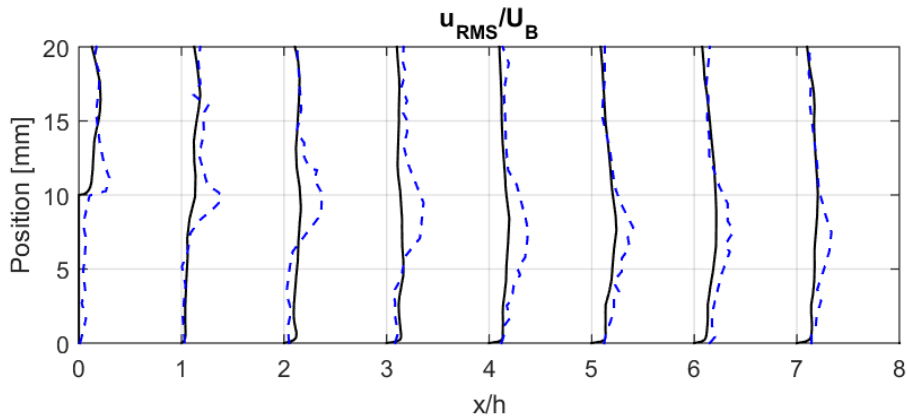


Figure 5.12: Computed profiles of turbulent intensity using the Bingham model setting B2 for mass consistency $C_m = 1.5\%$ (—) and corresponding experimental profiles from Claesson et al. (2012) (—).

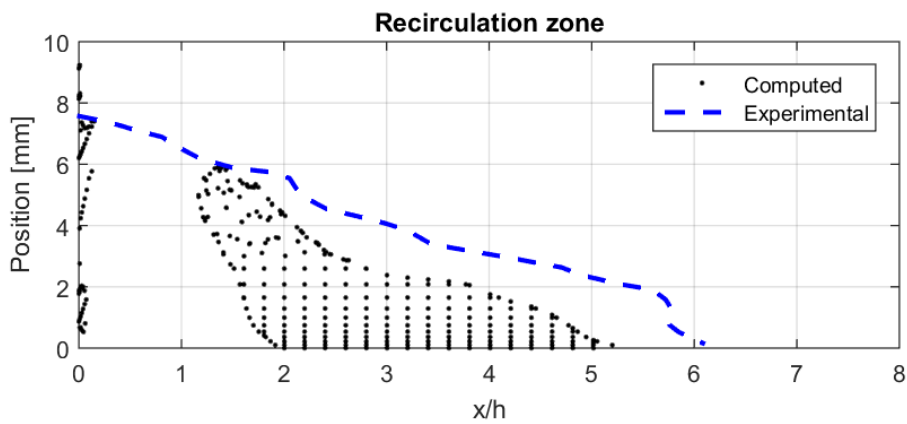


Figure 5.13: Computed recirculation zone, $\bar{u} \leq 0$, from simulations with the Bingham model setting B2 and experimental level curve $\bar{u} = 0$ from the experimental data in Claesson et al (2012).

Bingham model with setting B3

Computed profiles of mean streamwise velocity for setting B3 can be seen together with corresponding experimental profiles in Figure 5.14. Computed profiles of turbulent intensity can be seen with corresponding experimental profiles in Figure 5.15. The computed recirculation zone $\bar{u} \leq 0$ can be seen together with the experimental level curve $\bar{u} = 0$ in Figure 5.16.

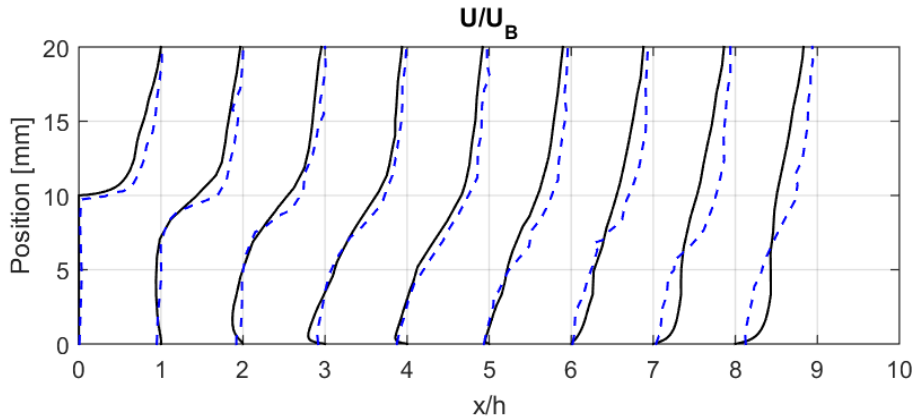


Figure 5.14: Computed profiles of mean streamwise velocity using the Bingham model setting B3 for mass consistency $C_m = 1.5\%$ (—) and corresponding experimental profiles from Claesson et al. (2012) (—).

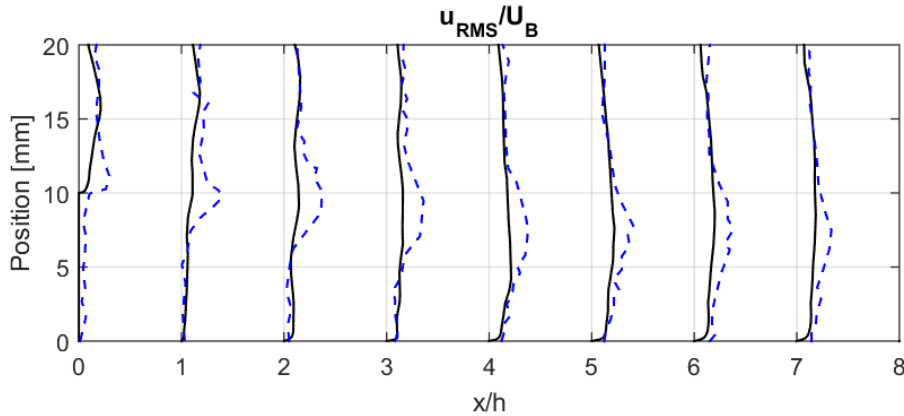


Figure 5.15: Computed profiles of turbulent intensity using the Bingham model setting B3 for mass consistency $C_m = 1.5\%$ (—) and corresponding experimental profiles from Claesson et al. (2012) (—).

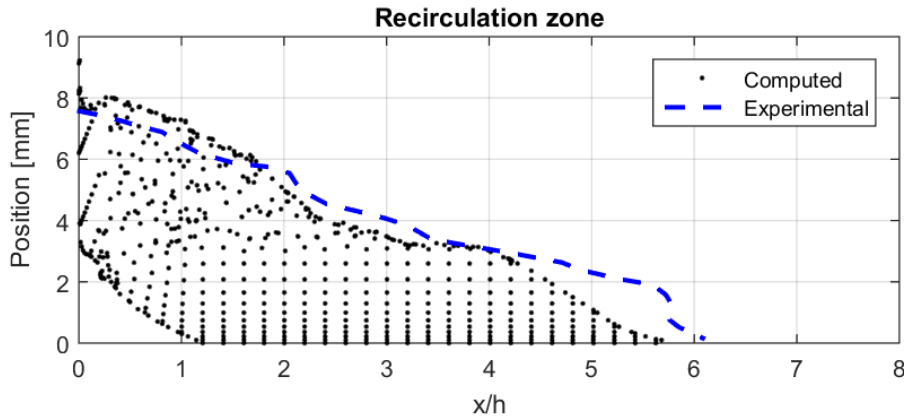


Figure 5.16: Computed recirculation zone, $\bar{u} \leq 0$, from simulations with the Bingham model setting B3 and experimental level curve $\bar{u} = 0$ from the experimental data in Claesson et al (2012).

Comparison of Bingham setting B1,B2 and B3

By comparing the profiles of mean streamwise velocity and turbulent intensity resulting from the simulations with the Bingham model setting B1, B2 and B3 it can be observed that the general flow pattern is the same for all three settings. This is expected since the same model is used with different parameter settings. In Figure 5.17 the computed RMS errors from experimental profiles of mean streamwise velocity are plotted for the three settings along the channel. All three settings produced the largest error in the downstream part of the channel after the flow reattachment. In Figure 5.18 the computed RMS errors of turbulent intensity can be seen for the three settings. A weak trend along the channel may be identified for the turbulent intensity error with a local maximum around $x/h \approx 2$ and a local minimum around $x/h \approx 6$. However, all three settings fail to capture the mixing layer seen in the experimental data, which is a major source of error.

Comparing the recirculation zones computed with the three model settings it can be seen that the experimental recirculation zone is clearly better resembled by setting B3 than with the other two settings. Looking at the computed errors it can also be observed that the setting B3 produced the smallest or next to smallest errors among the three settings along the channel. Given the results it may be inferred that setting B3 is the best parameter setting in the first step of the validation study.

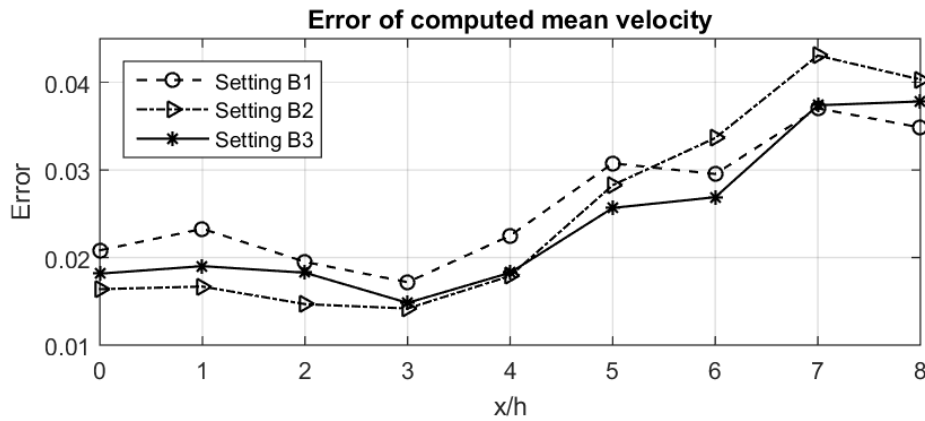


Figure 5.17: Standard error from experimental profiles of mean streamwise velocity at streamwise points downstream of the step from simulations with Bingham model setting B1, B2 and B3.

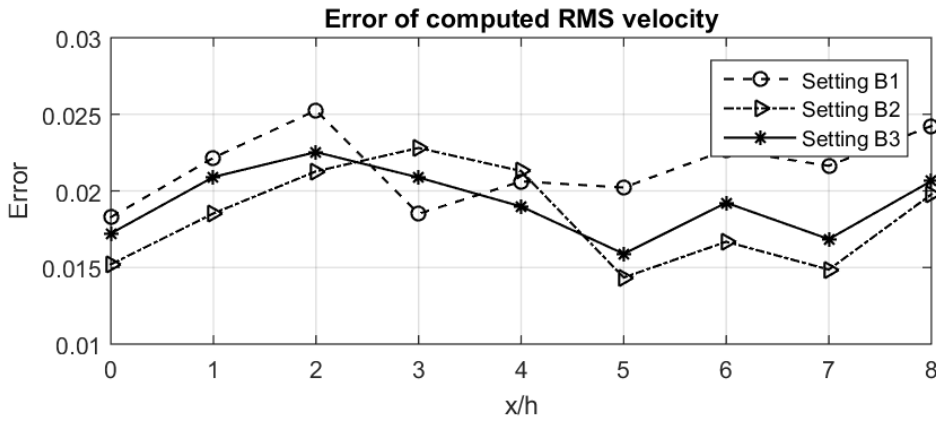


Figure 5.18: Standard error from experimental profiles of turbulent intensity at streamwise points downstream of the step from simulations with Bingham model setting B1, B2 and B3.

Bingham model with setting B4

Computed profiles of mean streamwise velocity for setting B4 can be seen together with corresponding experimental profiles in Figure 5.19. Computed profiles of turbulent intensity can be seen with corresponding experimental profiles in Figure 5.20. The computed recirculation can be seen together with experimental level curve $\bar{u} = 0$ in Figure 5.21. The zone resembles experimental data to some extent with respect to shape. Size and position of the zone is poorly resembled.

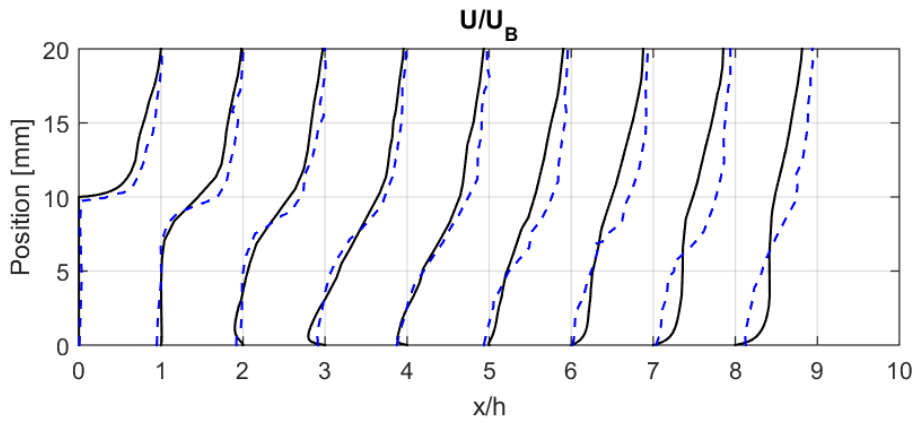


Figure 5.19: Computed profiles of mean streamwise velocity using the Bingham model setting B4 for mass consistency $C_m = 1.5\%$ (—) and corresponding experimental profiles from Claesson et al. (2012) (--).

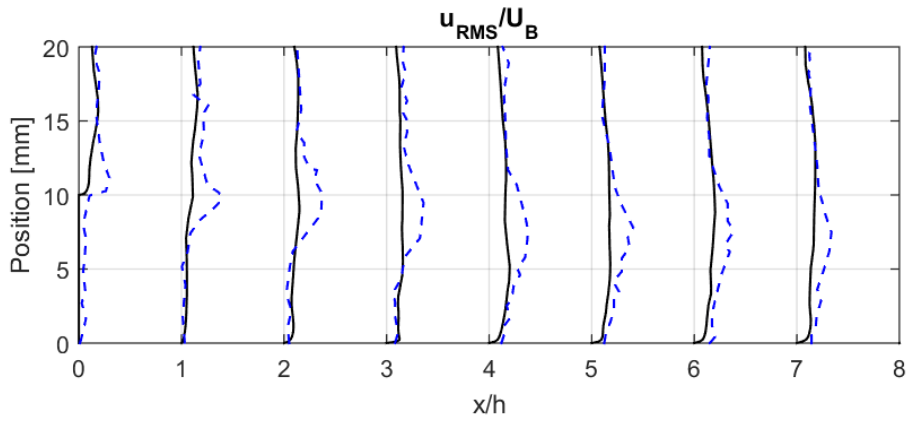


Figure 5.20: Computed profiles of turbulent intensity using the Bingham model setting B4 for mass consistency $C_m = 1.5\%$ (—) and corresponding experimental profiles from Claesson et al. (2012) (--).

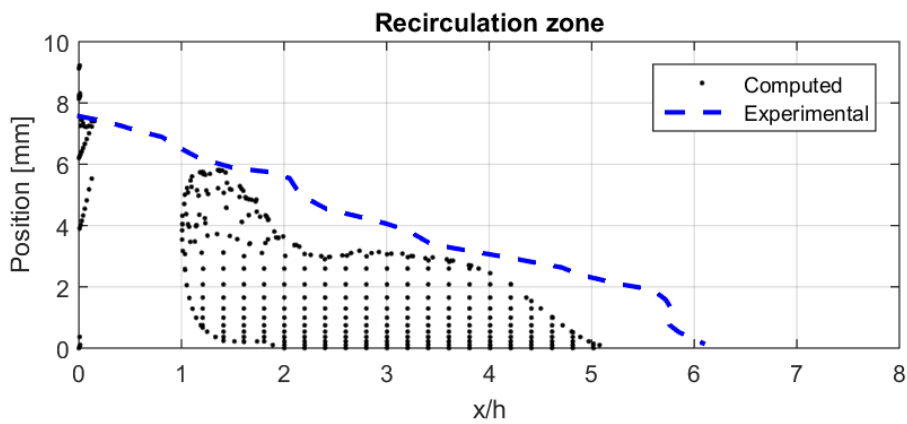


Figure 5.21: Computed recirculation zone, $\bar{u} \leq 0$, from simulations with the Bingham model setting B4 and experimental level curve $\bar{u} = 0$ from the experimental data in Claesson et al (2012).

Bingham model with setting B5

Computed profiles of mean streamwise velocity for setting B5 can be seen together with corresponding experimental profiles in Figure 5.22. Computed profiles of turbulent intensity can be seen with corresponding experimental profiles in Figure 5.23. The computed recirculation zone $\bar{u} \leq 0$ can be seen together with the experimental level curve $\bar{u} = 0$ in Figure 5.24.

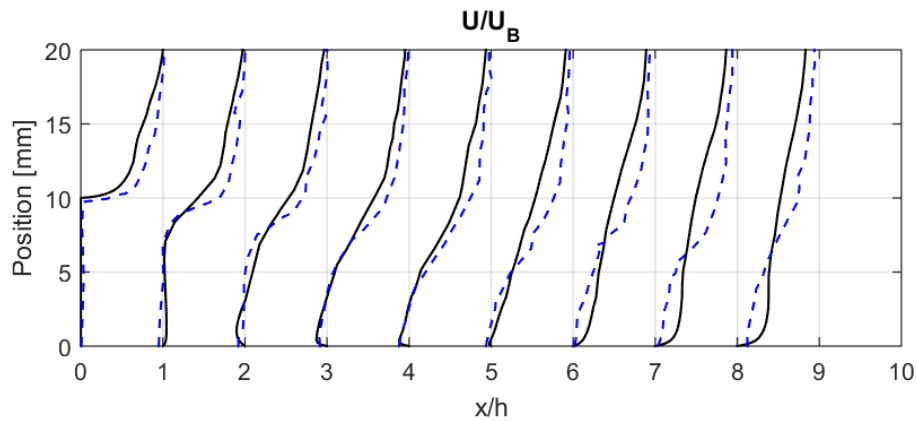


Figure 5.22: Computed profiles of mean streamwise velocity using the Bingham model setting B5 for mass consistency $C_m = 1.5\%$ (—) and corresponding experimental profiles from Claesson et al. (2012) (--).

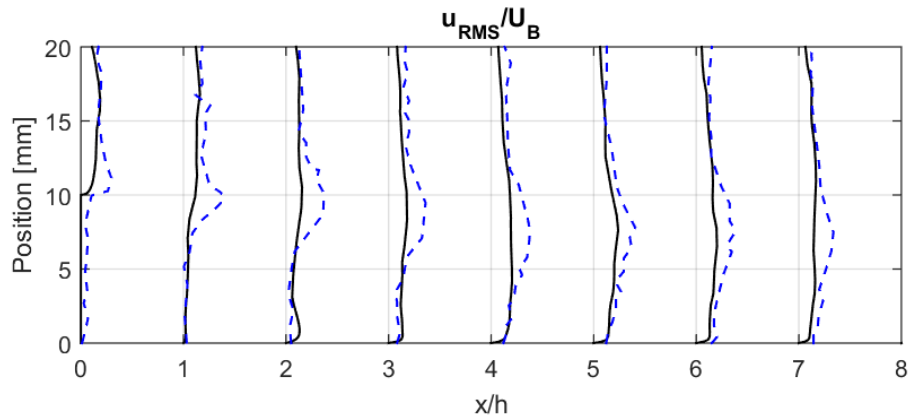


Figure 5.23: Computed profiles of turbulent intensity using the Bingham model setting B5 for mass consistency $C_m = 1.5\%$ (—) and corresponding experimental profiles from Claesson et al. (2012) (--).

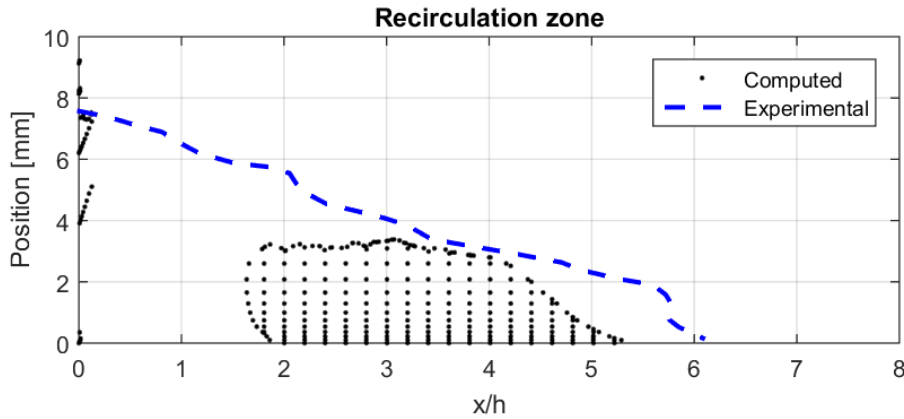


Figure 5.24: Computed recirculation zone, $\bar{u} \leq 0$, from simulations with the Bingham model setting B5 and experimental level curve $\bar{u} = 0$ from the experimental data in Claesson et al (2012).

Comparison of Bingham setting B3, B4 and B5

Computed RMS errors from the experimental profiles of mean streamwise velocity can be seen for the three settings in Figure 5.25 for setting B3, B4 and B5. RMS errors from experimental profiles of turbulent intensity can be seen in Figure 5.26. Similar general trends as for the settings in the first step of the Bingham model validation study, i.e. setting B1, B2 and B3, can also be seen for setting B4 and B5. The mean velocity errors increase with the downstream distance from the step and the turbulent intensity error has a local maximum around $x/h \approx 2$ and a local minimum around $x/h \approx 5$. However, all three settings fail to capture mixing layer seen in the experimental data, which again is a major source of error.

By comparing the computed recirculation zones for the three settings it can be observed that both setting B4 and B5 yielded zones that resembled the experimental data significantly worse than setting B3. Setting B3 also yielded the smallest or next to smallest errors among the three in the major part of the channel downstream of the step, both with respect to mean streamwise velocity and turbulent intensity. Given these results it may be inferred that setting B3 is the best parameter setting for the Bingham model of the ones studied.

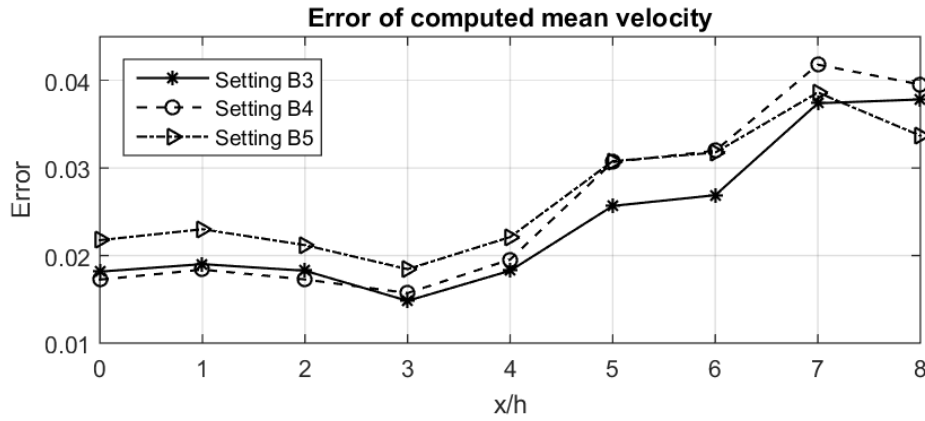


Figure 5.25: Standard error from experimental profiles of mean streamwise velocity at streamwise points downstream of the step from simulations with Bingham model setting B3, B4 and B5.

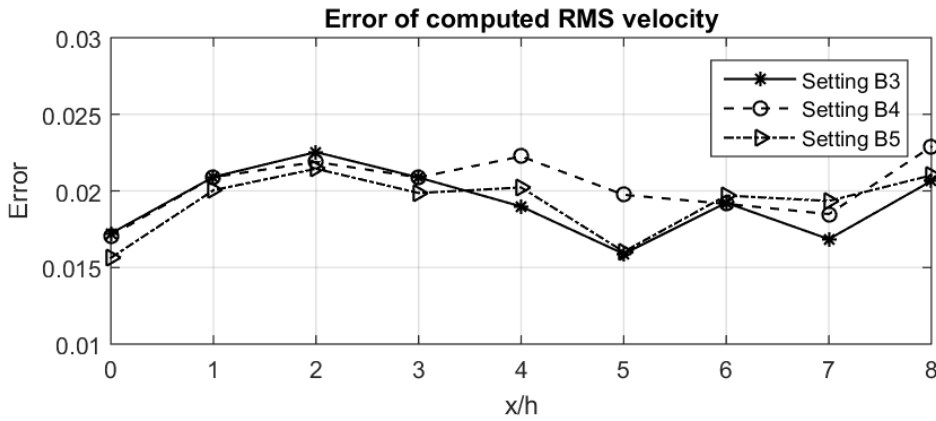


Figure 5.26: Standard error from experimental profiles of turbulent intensity at streamwise points downstream of the step from simulations with Bingham model setting B3, B4 and B5.

5.1.4 Simulations with the ODF model

Results obtained from all simulations performed with the ODF model are presented in this section. The results from each step of the validation study are first presented individually and then compared to all simulations in the same step.

ODF model setting R1

Computed profiles of mean streamwise velocity for setting R1 can be seen together with corresponding experimental profiles in Figure 5.27. Computed profiles of turbulent intensity can be seen with corresponding experimental profiles in Figure 5.28. The computed recirculation zone $\bar{u} \leq 0$ can be seen together with the experimental level curve $\bar{u} = 0$ in Figure 5.29.

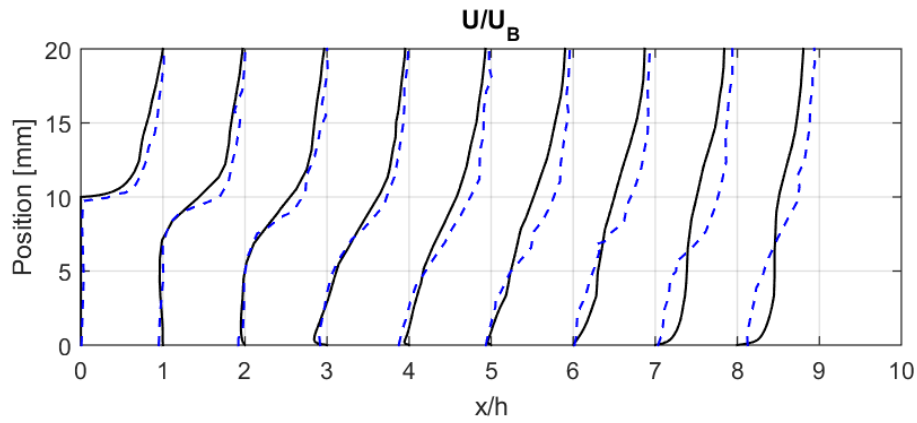


Figure 5.27: Computed profiles of mean streamwise velocity using the ODF model setting R1 for mass consistency $C_m = 1.5\%$ (—) and corresponding experimental profiles from Claesson et al. (2012) (--).

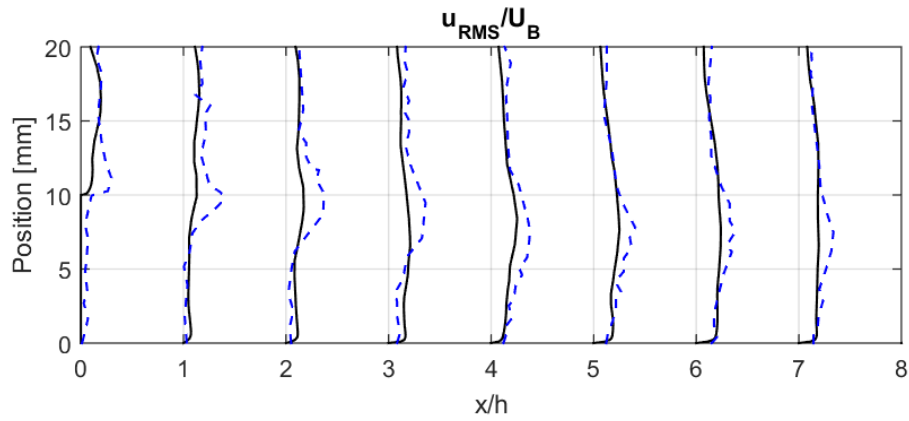


Figure 5.28: Computed profiles of turbulent intensity using the ODF model setting R1 for mass consistency $C_m = 1.5\%$ (—) and corresponding experimental profiles from Claesson et al. (2012) (--).

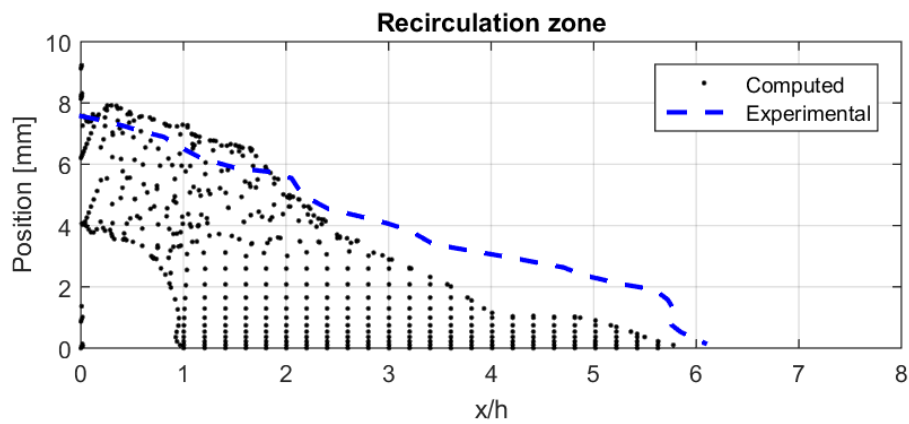


Figure 5.29: Computed recirculation zone, $\bar{u} \leq 0$, from simulations with the ODF model setting R1 and experimental level curve $\bar{u} = 0$ from the experimental data in Claesson et al (2012).

ODF model setting R2

Computed profiles of mean streamwise velocity for setting R2 can be seen together with corresponding experimental profiles in Figure 5.30. Computed profiles of turbulent intensity can be seen with corresponding experimental profiles in Figure 5.31. The computed recirculation zone $\bar{u} \leq 0$ can be seen together with the experimental level curve $\bar{u} = 0$ in Figure 5.32.

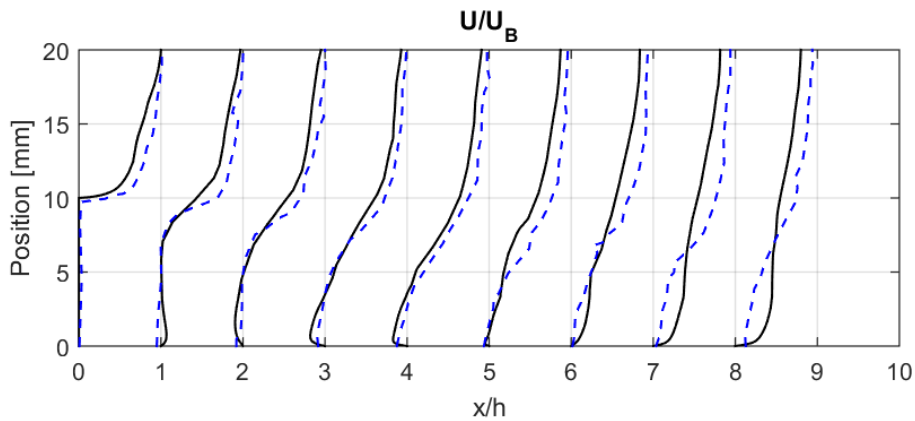


Figure 5.30: Computed profiles of mean streamwise velocity using the ODF model setting R2 for mass consistency $C_m = 1.5\%$ (—) and corresponding experimental profiles from Claesson et al. (2012) (--).

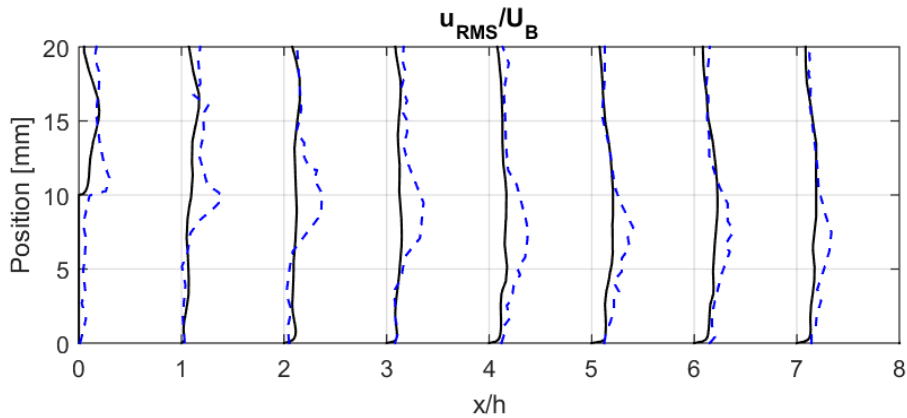


Figure 5.31: Computed profiles of turbulent intensity using the ODF model setting R2 for mass consistency $C_m = 1.5\%$ (—) and corresponding experimental profiles from Claesson et al. (2012) (--).

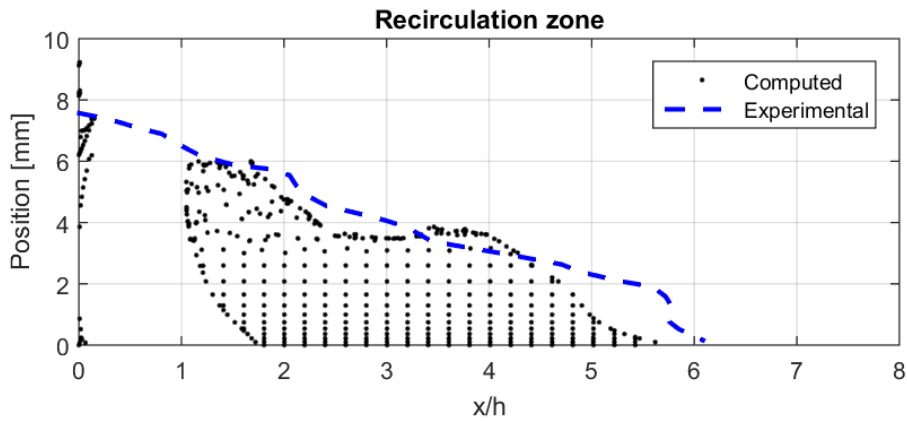


Figure 5.32: Computed recirculation zone, $\bar{u} \leq 0$, from simulations with the ODF model setting R2 and experimental level curve $\bar{u} = 0$ from the experimental data in Claesson et al (2012).

ODF model setting R3

Computed profiles of mean streamwise velocity for setting R3 can be seen together with corresponding experimental profiles in Figure 5.33. Computed profiles of turbulent intensity can be seen with corresponding experimental profiles in Figure 5.34. The computed recirculation zone $\bar{u} \leq 0$ can be seen together with the experimental level curve $\bar{u} = 0$ in Figure 5.35.

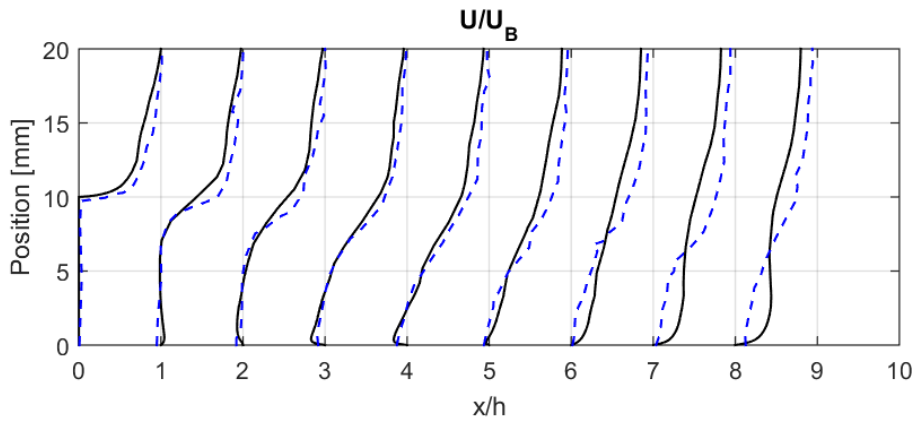


Figure 5.33: Computed profiles of mean streamwise velocity using the ODF model setting R3 for mass consistency $C_m = 1.5\%$ (—) and corresponding experimental profiles from Claesson et al. (2012) (--).

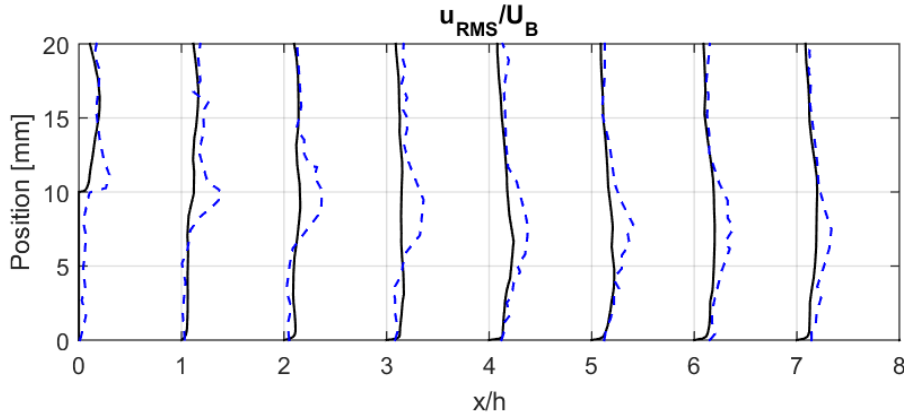


Figure 5.34: Computed profiles of turbulent intensity using the ODF model setting R3 for mass consistency $C_m = 1.5\%$ (—) and corresponding experimental profiles from Claesson et al. (2012) (---).

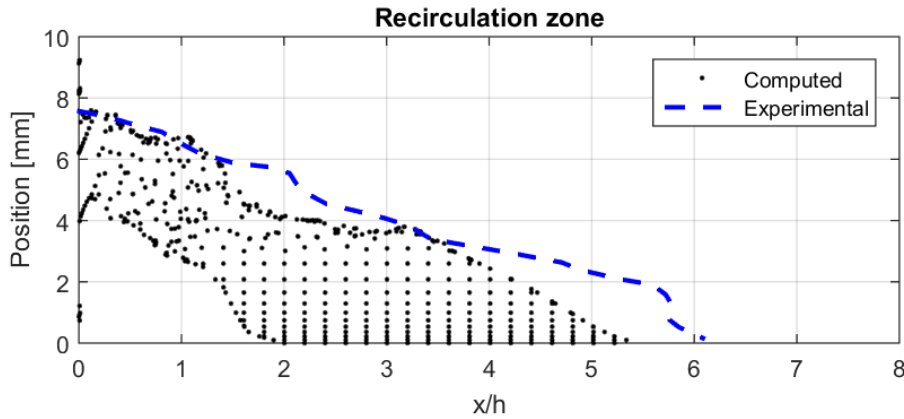


Figure 5.35: Computed recirculation zone, $\bar{u} \leq 0$, from simulations with the ODF model setting R3 and experimental level curve $\bar{u} = 0$ from the experimental data in Claesson et al (2012).

Comparison of ODF model setting R1, R2 and R3

In Figure 5.36 computed RMS errors from the experimental profiles of mean streamwise velocity are plotted for settings R1, R2 and R3. In Figure 5.36 the computed RMS errors from experimental profiles of mean streamwise velocity can be seen for the three settings. In the same way as for the simulations with the Bingham model a general trend can be seen for the mean velocity errors as they increase with downstream distance from the step. A similar trend as for the Bingham model simulations can also be seen for the turbulent intensity errors with local maxima slightly downstream of the step and local minima further downstream.

By comparing the computed recirculation zones for setting R1, R2 and R3 it can be seen that neither of the settings gave as good resemblance as the best Bingham model setting, B3. The different settings do however capture different features of the recirculation zone. The given results indicate that the different choice of values of homogenous ODF standard deviation may capture different parts of the flow pattern correctly. They also

indicate that a homogeneous standard deviation does not give a sufficiently complete description of the flow.

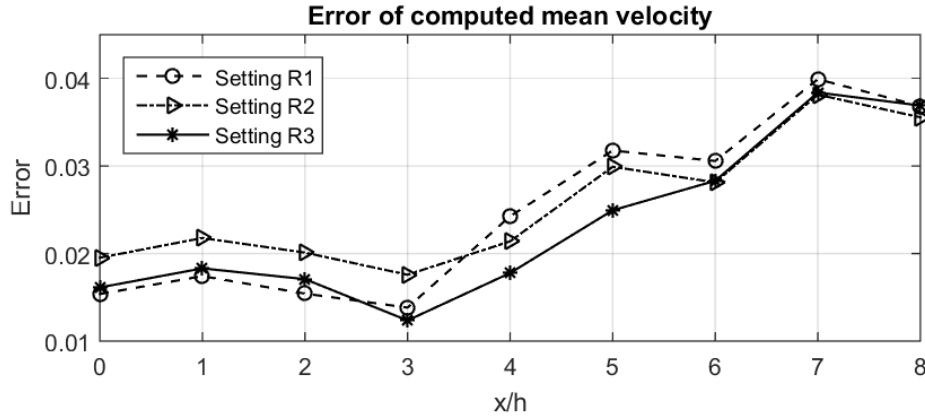


Figure 5.36: Standard error from experimental profiles of mean streamwise velocity at streamwise points downstream of the step from simulations with ODF model setting R1, R2 and R3.

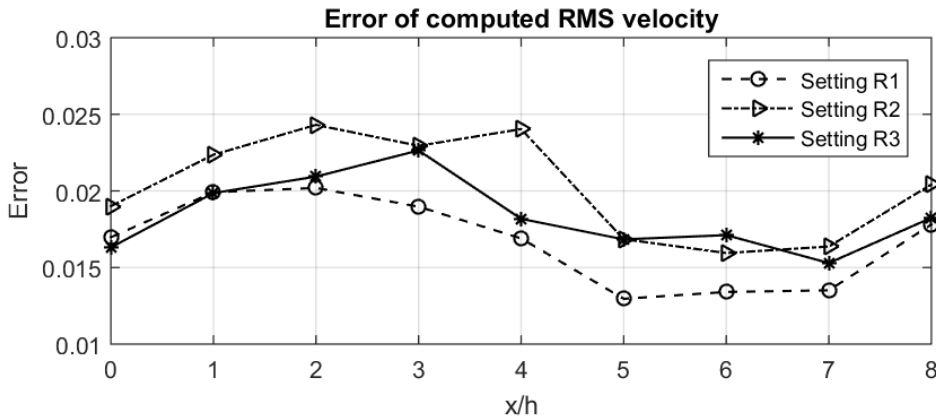


Figure 5.37: Standard error from experimental profiles of turbulent intensity at streamwise points downstream of the step from simulations with ODF model setting R1, R2 and R3.

ODF model setting R4

Computed profiles of mean streamwise velocity for setting R4 can be seen together with corresponding experimental profiles in Figure 5.38. Computed profiles of turbulent intensity can be seen with corresponding experimental profiles in Figure 5.39. The computed recirculation zone $\bar{u} \leq 0$ can be seen together with the experimental level curve $\bar{u} = 0$ in Figure 5.40.

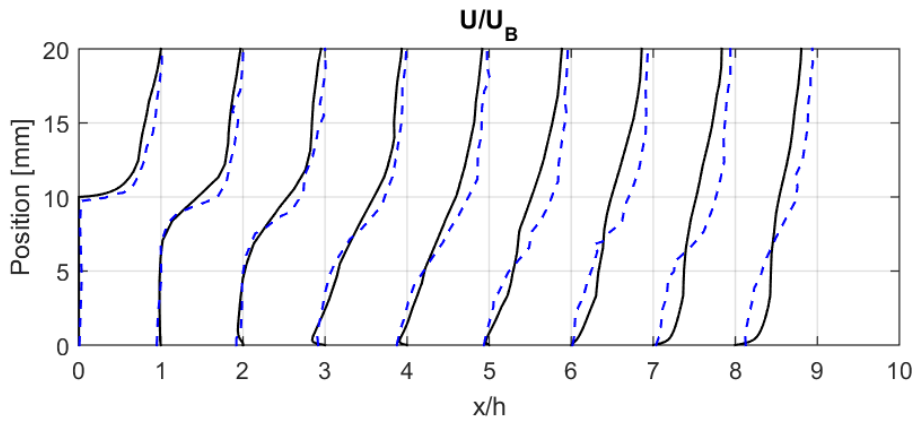


Figure 5.38: Computed profiles of mean streamwise velocity using the ODF model setting R4 for mass consistency $C_m = 1.5\%$ (—) and corresponding experimental profiles from Claesson et al. (2012) (--).

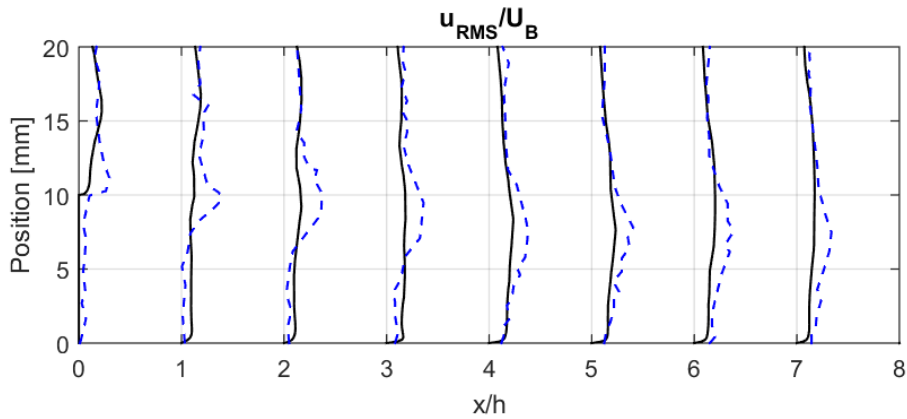


Figure 5.39: Computed profiles of turbulent intensity using the ODF model setting R4 for mass consistency $C_m = 1.5\%$ (—) and corresponding experimental profiles from Claesson et al. (2012) (--).

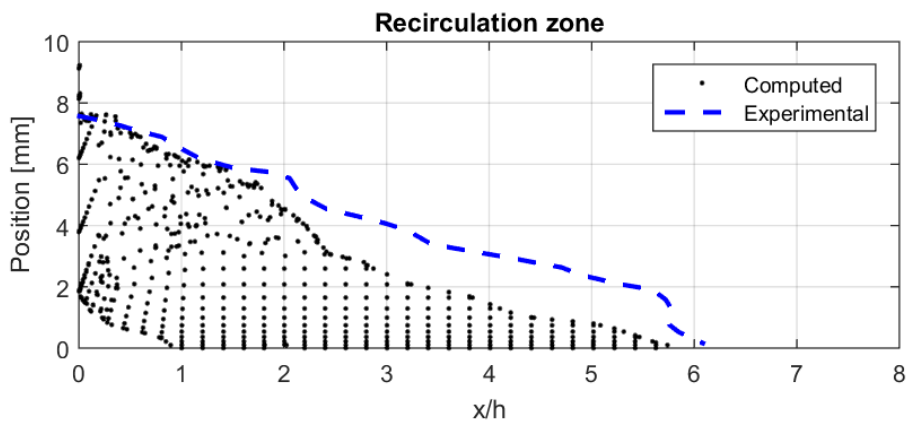


Figure 5.40: Computed recirculation zone, $\bar{u} \leq 0$, from simulations with the ODF model setting R4 and experimental level curve $\bar{u} = 0$ from the experimental data in Claesson et al (2012).

ODF model setting R5

Computed profiles of mean streamwise velocity for setting R5 can be seen together with corresponding experimental profiles in Figure 5.41. Computed profiles of turbulent intensity can be seen with corresponding experimental profiles in Figure 5.42. The computed recirculation zone $\bar{u} \leq 0$ can be seen together with the experimental level curve $\bar{u} = 0$ in Figure 5.43.

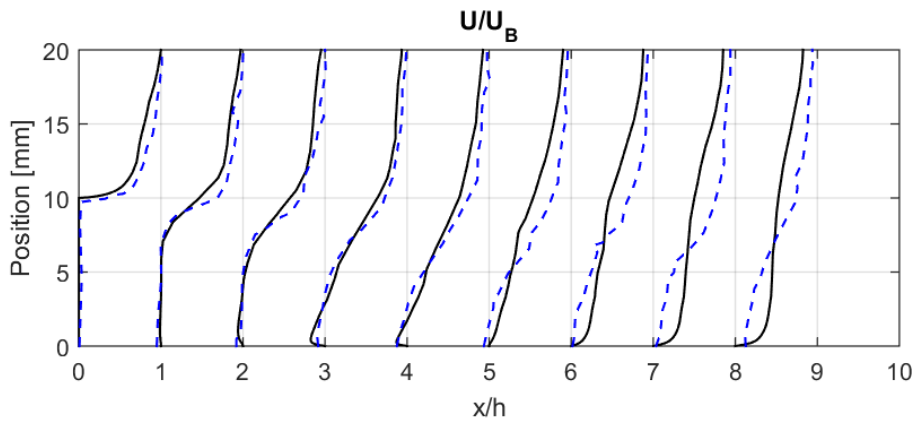


Figure 5.41: Computed profiles of mean streamwise velocity using the ODF model setting R5 for mass consistency $C_m = 1.5\%$ (—) and corresponding experimental profiles from Claesson et al. (2012) (--).

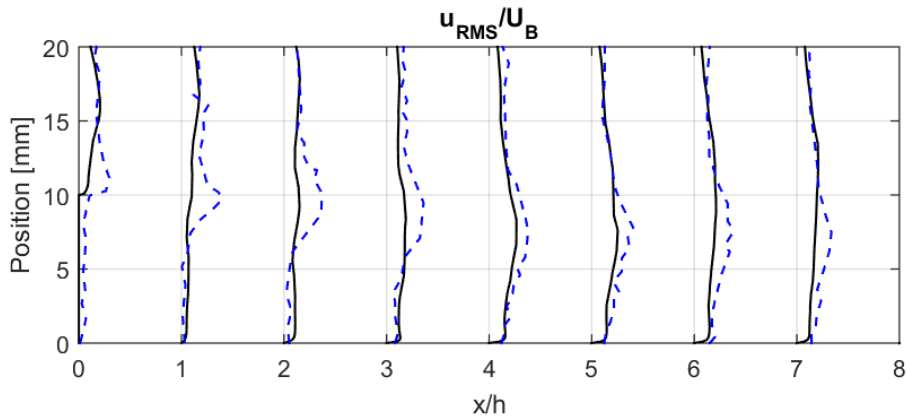


Figure 5.42: Computed profiles of turbulent intensity using the ODF model setting R5 for mass consistency $C_m = 1.5\%$ (—) and corresponding experimental profiles from Claesson et al. (2012) (--).

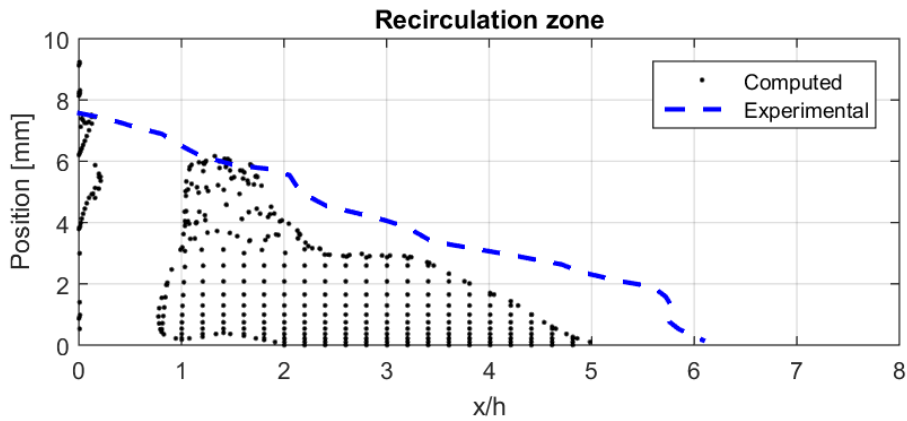


Figure 5.43: Computed recirculation zone, $\bar{u} \leq 0$, from simulations with the ODF model setting R5 and experimental level curve $\bar{u} = 0$ from the experimental data in Claesson et al (2012).

ODF model setting R6

Computed profiles of mean streamwise velocity for setting R6 can be seen together with corresponding experimental profiles in Figure 5.44. Computed profiles of turbulent intensity can be seen with corresponding experimental profiles in Figure 5.45. The computed recirculation zone $\bar{u} \leq 0$ can be seen together with the experimental level curve $\bar{u} = 0$ in Figure 5.46.

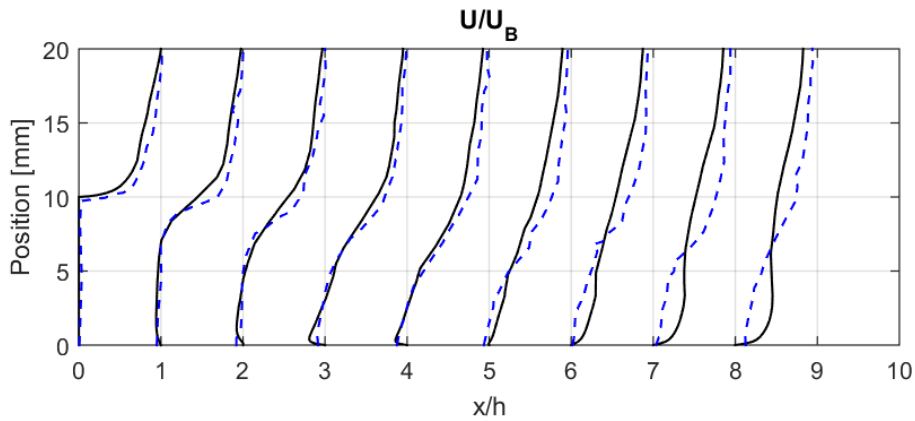


Figure 5.44: Computed profiles of mean streamwise velocity using the ODF model setting R6 for mass consistency $C_m = 1.5\%$ (—) and corresponding experimental profiles from Claesson et al. (2012) (--).

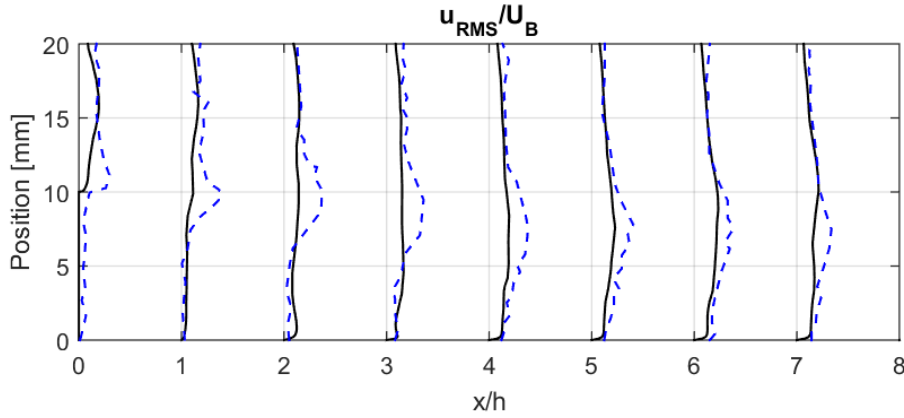


Figure 5.45: Computed profiles of turbulent intensity using the ODF model setting R6 for mass consistency $C_m = 1.5\%$ (—) and corresponding experimental profiles from Claesson et al. (2012) (--).

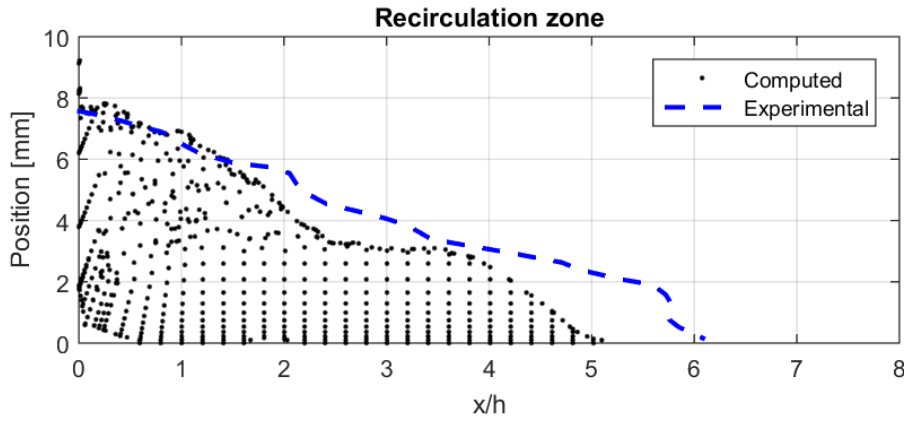


Figure 5.46: Computed recirculation zone, $\bar{u} \leq 0$, from simulations with the ODF model setting R6 and experimental level curve $\bar{u} = 0$ from the experimental data in Claesson et al (2012).

Comparison of ODF model setting R4, R5 and R6

In Figure 5.47 the computed RMS errors from experimental profiles of mean streamwise velocity are plotted for setting R4, R5 and R6. In Figure 5.48 the computed RMS errors from experimental profiles of turbulent intensity can be seen for the three settings. The same general trends are seen as for all previous simulations with the Bingham model and the ODF model.

Comparing the recirculation zones for the three settings it can be observed that while setting R5 clearly gives the worst prediction of the three, setting R4 and R6 both predict the recirculation zone to some extent. Setting R4 gives a good prediction on the length of the zone but the shape is not correct. Setting R6 slightly underestimates the length of the zone but the shape is well predicted. Setting R6 has the smallest or next to smallest error with respect to mean velocity along the channel while the error with respect to turbulent intensity actually is the largest of the three settings for the middle section of the channel. Setting R4, the other hand has the smallest or next to smallest error with respect to

turbulent intensity along the channel while the mean velocity error is the largest among the three for the middle section. Given the results both setting R4 and R6 could be seen as the best parameter setting among the three. However, given that the turbulent intensity contains large errors due to that the mixing layer was not captured by simulations, the result that setting R6 performed well with respect to mean velocity and in resembling the recirculation zone may be used as motivation to for setting R6 being the best setting out of the three. It was therefore the one chosen for further validation.

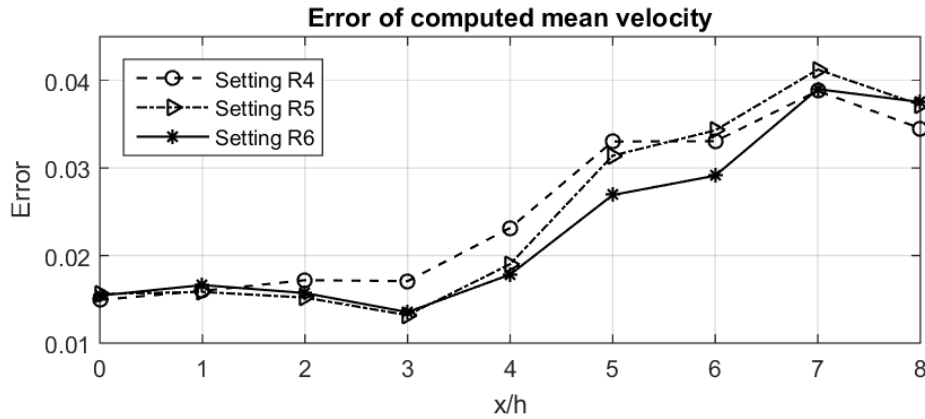


Figure 5.47: Standard error from experimental profiles of mean streamwise velocity at streamwise points downstream of the step from simulations with ODF model setting R4, R5 and R6.

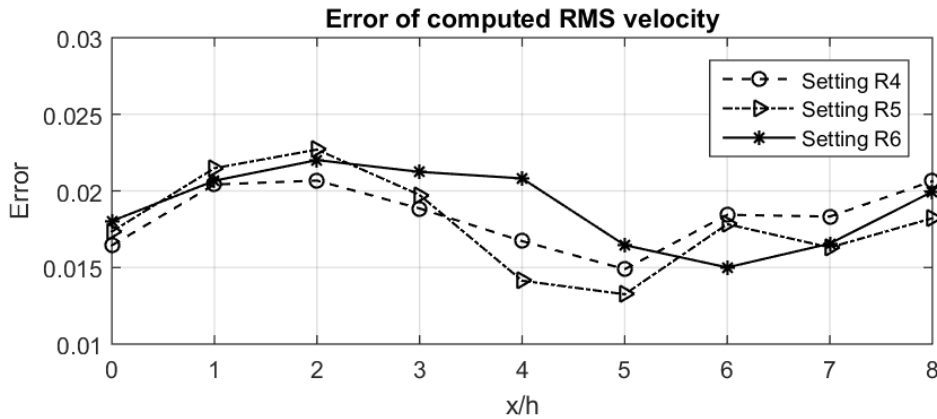


Figure 5.48: Standard error from experimental profiles of turbulent intensity at streamwise points downstream of the step from simulations with ODF model setting R4, R5 and R6.

ODF model setting R7

Computed profiles of mean streamwise velocity for setting R6 can be seen together with corresponding experimental profiles in Figure 5.49. Computed profiles of turbulent intensity can be seen with corresponding experimental profiles in Figure 5.50. The computed recirculation zone $\bar{u} \leq 0$ can be seen together with the experimental level curve $\bar{u} = 0$ in in Figure 5.51.

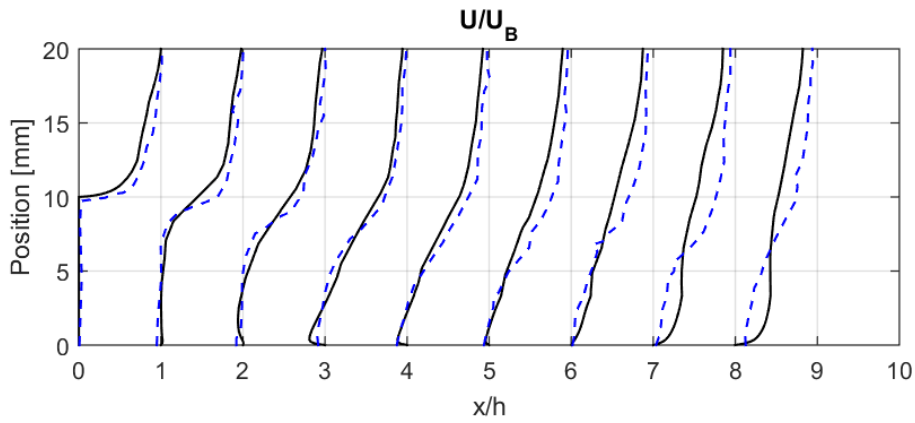


Figure 5.49: Computed profiles of mean streamwise velocity using the ODF model setting R7 for mass consistency $C_m = 1.5\%$ (—) and corresponding experimental profiles from Claesson et al. (2012) (--).

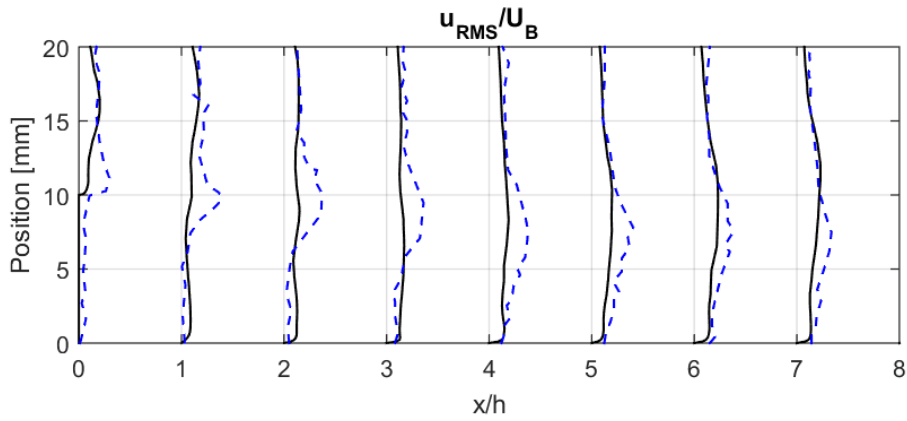


Figure 5.50: Computed profiles of turbulent intensity using the ODF model setting R7 for mass consistency $C_m = 1.5\%$ (—) and corresponding experimental profiles from Claesson et al. (2012) (--).

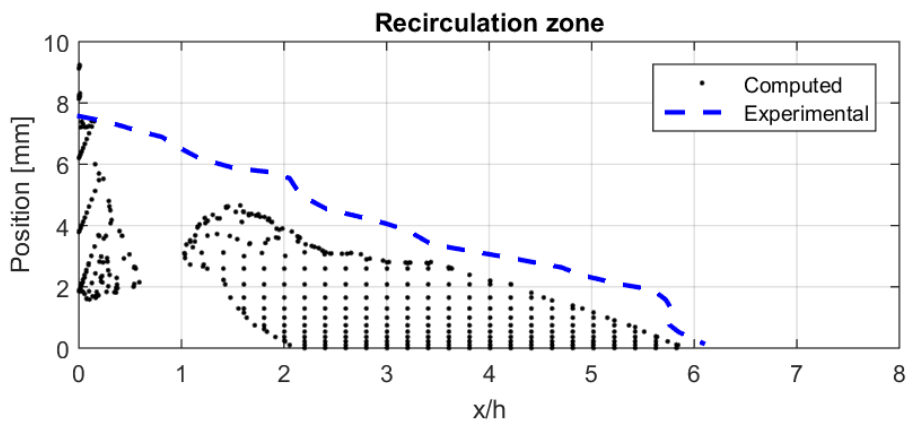


Figure 5.51: Computed recirculation zone, $\bar{u} \leq 0$, from simulations with the ODF model setting R7 and experimental level curve $\bar{u} = 0$ from the experimental data in Claesson et al (2012).

ODF model setting R8

Computed profiles of mean streamwise velocity for setting R6 can be seen together with corresponding experimental profiles in Figure 5.52. Computed profiles of turbulent intensity can be seen with corresponding experimental profiles in Figure 5.53. The computed recirculation zone $\bar{u} \leq 0$ can be seen together with the experimental level curve $\bar{u} = 0$ in Figure 5.54.

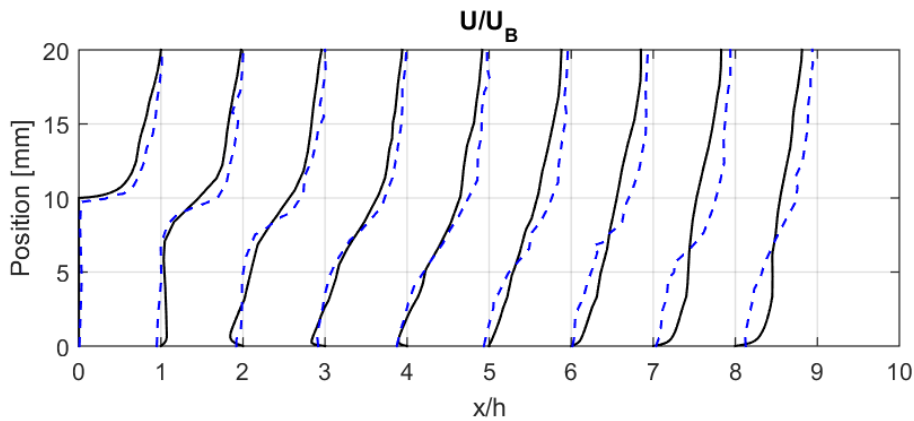


Figure 5.52: Computed profiles of mean streamwise velocity using the ODF model setting R8 for mass consistency $C_m = 1.5\%$ (—) and corresponding experimental profiles from Claesson et al. (2012) (--).

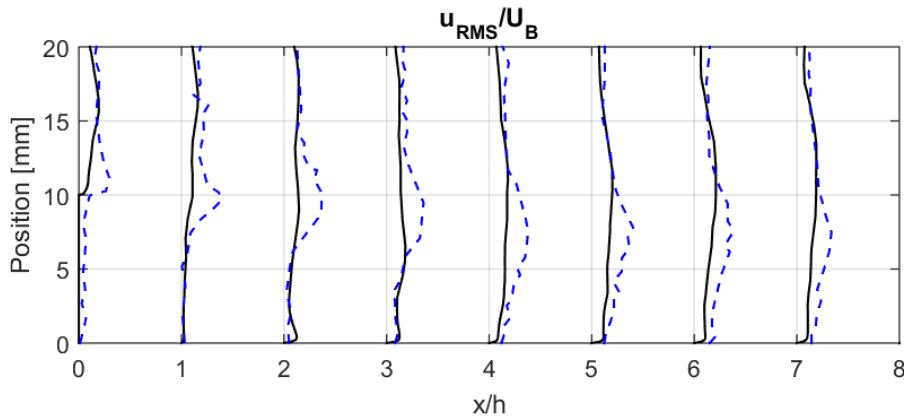


Figure 5.53: Computed profiles of turbulent intensity using the ODF model setting R8 for mass consistency $C_m = 1.5\%$ (—) and corresponding experimental profiles from Claesson et al. (2012) (--).

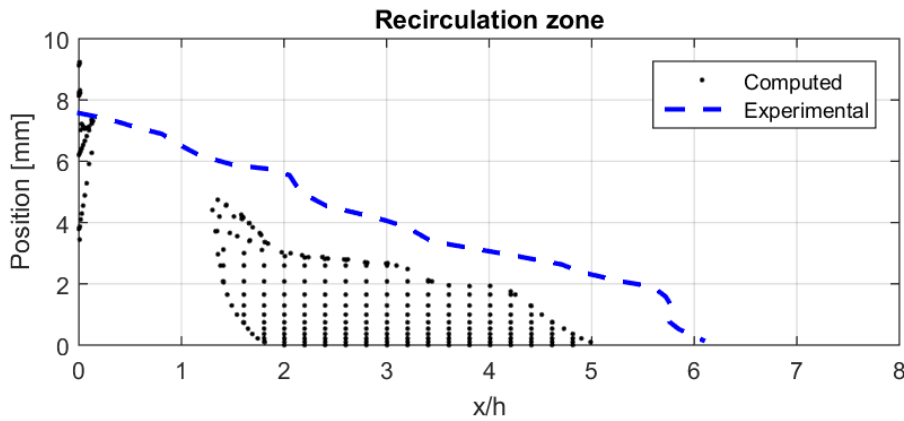


Figure 5.54: Computed recirculation zone, $\bar{u} \leq 0$, from simulations with the ODF model setting R8 and experimental level curve $\bar{u} = 0$ from the experimental data in Claesson et al (2012).

Comparison of ODF model setting R6, R7 and R8

In Figure 5.55 the computed RMS errors of mean streamwise velocity from corresponding experimental profiles can be seen for setting R6, R7 and R8. In Figure 5.56 the computed root mean square errors of turbulent intensity can be seen for the three settings. The same general trends can be seen as for all presented simulations with the fibre models. Setting R6 has the smallest or next to smallest error among the three settings both with respect to mean streamwise velocity and turbulent intensity. Comparing the three recirculation zones it can be observed that both setting R7 and R8 gave worse resemblance of the experimental data than setting R6. Given results indicate the among the three settings compared setting R6 is the best performing parameter setting.

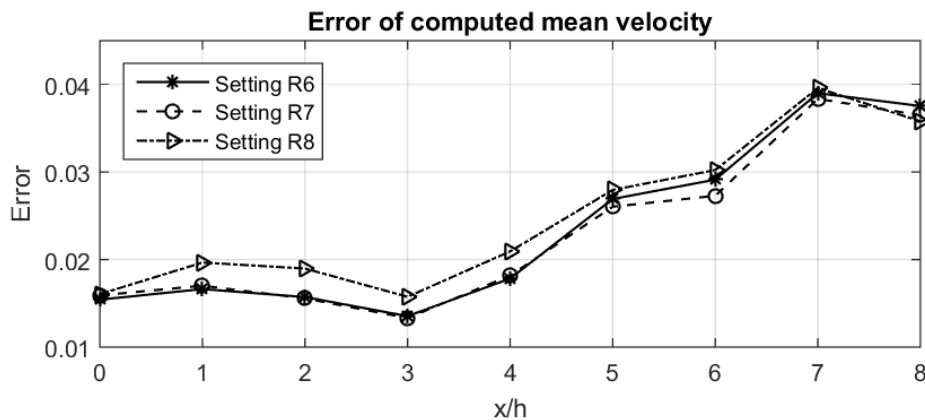


Figure 5.55: Standard error from experimental profiles of mean streamwise velocity at streamwise points downstream of the step from simulations with ODF model setting R6, R7 and R8.

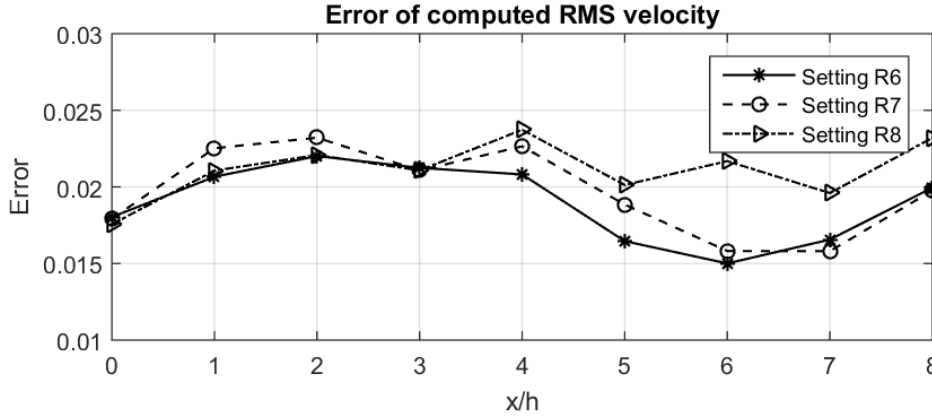


Figure 5.56: Standard error from experimental profiles of turbulent intensity at streamwise points downstream of the step from simulations with ODF model setting R6, R7 and R8.

5.1.5 Comparison between the respective models

Computed RMS errors from experimental profiles of mean streamwise velocity can be seen in Figure 5.57 for the best performing Bingham model setting, setting B3, for the best performing ODF model setting, setting R6, and computed in the same way from simulations of pure water flow. Corresponding RMS square errors with respect to turbulent intensity can be seen in Figure 5.58. It can be seen that for the upstream half of the channel downstream of the step the simulations with pure water does actually produce smaller errors than the fibre models. The result that pure water simulations may be able to resemble suspension flow in that area is somewhat expected since it is a turbulent area where the suspension is expected to be fluidised and exhibit Newtonian-like rheology. Further downstream, as turbulence decays, fibre effects increase in significance for the flow pattern and it can be seen in both Figure 5.57 and in Figure 5.58 that the fibre models both result in smaller errors. The computed recirculation zones $\bar{u} \leq 0$ for the three cases are shown for comparison in Figure 5.59. The experimental recirculation zone curve $\bar{u} = 0$ from experiments with fibre mass consistency $C_m = 1.5\%$ are included with all three recirculation zones. It can be observed that both the Bingham model and the ODF model outperform the pure water simulations in resembling the experimental recirculation zone the fibre suspension flow.

The fibre models showed better agreement with experimental profiles of mean velocity and turbulent intensity, respectively, in the downstream part of the channel downstream of the step. The recirculation zones produced by the simulations with the fibre models are both significantly better than the one obtained in the simulation of pure water. The results indicate that the fibre models take into account fibre effects on the suspension flow that are not captured by simulations of pure water. The performances of the best parameter settings for the Bingham model and the ODF model, respectively, are close to similar both with respect to computed errors and recirculation zones. Comparing the RMS errors of the models it can be observed that the Bingham model has the larger error in the upstream half of the channel and the lower error in the downstream part out of the two models. The recirculation zone is slightly better resembled by the Bingham model,

mainly because the length is slightly better resembled. Given the results the Bingham model is slightly more accurate than the ODF model, at least with the parameter settings tested at current stage and with the given experimental data.

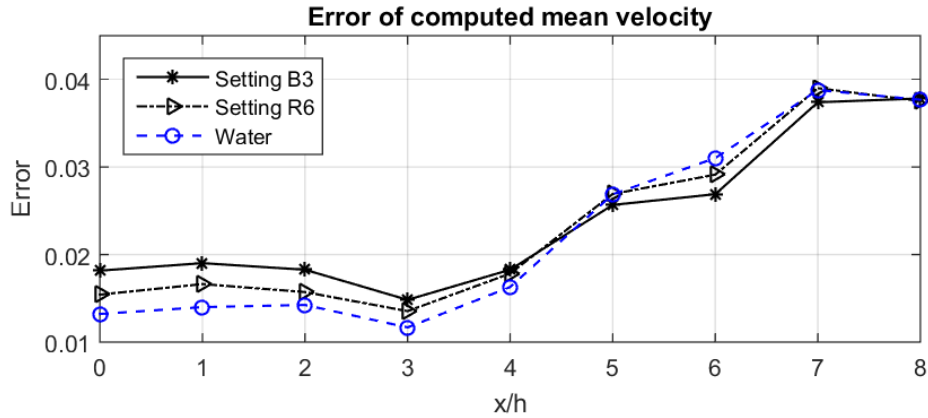


Figure 5.57: Standard error from experimental profiles of mean streamwise velocity at streamwise points downstream of the step for the best performing settings of the Bingham model and the ODF model and for pure water.

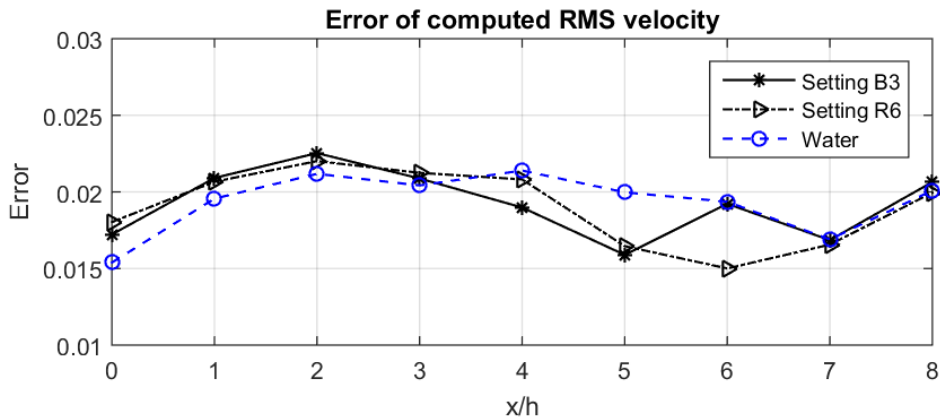


Figure 5.58: Standard error from experimental profiles of turbulent intensity at streamwise points downstream of the step for the best performing settings of the Bingham model and the ODF model and for pure water.

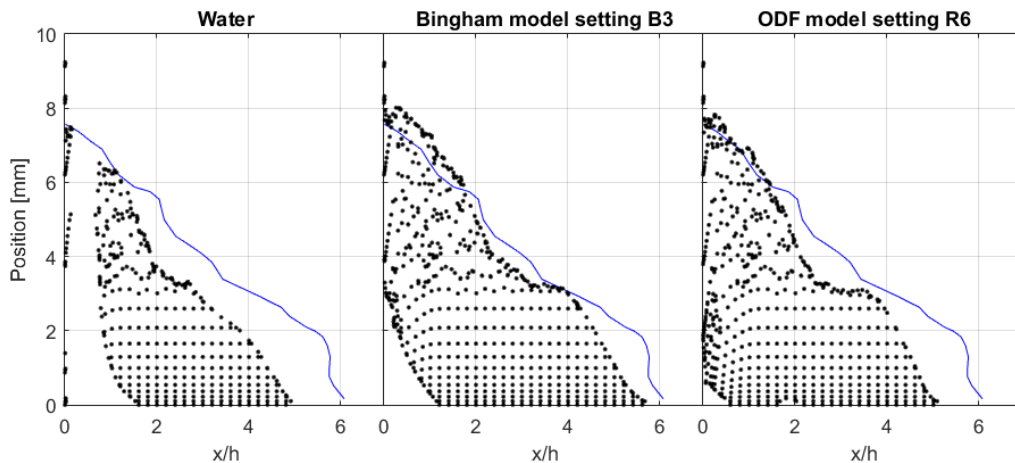


Figure 5.59: Computed recirculation zone using pure water (left), Bingham model setting B3 (middle) and ODF model setting R6 (right) plotted together with the recirculation curve obtained in the experiments by Claesson et al (2012) with fibre mass consistency 1.5%.

5.2 Comparison with experiments by Xu & Aidun (2005)

Computed profiles of mean streamwise velocity and turbulent intensity can be seen plotted with corresponding experimental data from Xu & Aidun (2005) in Figure 5.60 for fibre mass concentration 1.0% and $Re = 37,000$, in Figure 5.61 for 1.0% and $Re = 92,000$, in Figure 5.62 for 0.1% and $Re = 37,000$ and in Figure 5.63 for 0.1% and $Re = 92,000$. A general trend observed is that both models resemble the experimental velocity profiles better for higher Reynolds number than for lower and for lower fibre concentration than for higher. The result is expected since both a high Reynolds number and a low fibre concentration, respectively, decreases the effects of fibres in such a way that the suspension will exhibit Newtonian rheology. At lower Reynolds number and, especially, at the higher concentration fibre effects which are difficult to model correctly become more important for the flow. In addition, Xu & Aidun (2005) also concluded that increased flow rate decreases the influence of fibre effects.

With exception for the case of the lower Reynolds number and the higher concentration the predicted turbulent intensity is systematically overestimated by both fibre models. The results may indicate that the fibre models do not dampen the turbulence sufficiently to resemble the experimental flow correctly. In the case of the lower Reynolds number and the higher concentration, however, the Bingham model instead underestimates the turbulent intensity, indicating the turbulence in that flow is instead too much dampened. The overall results show that the performance of the studied fibre models depend strongly on the flow regime and concentration. The models showed success in resembling the experimental profiles of mean velocity and turbulent intensity in the more turbulent flows, which they are intended for.

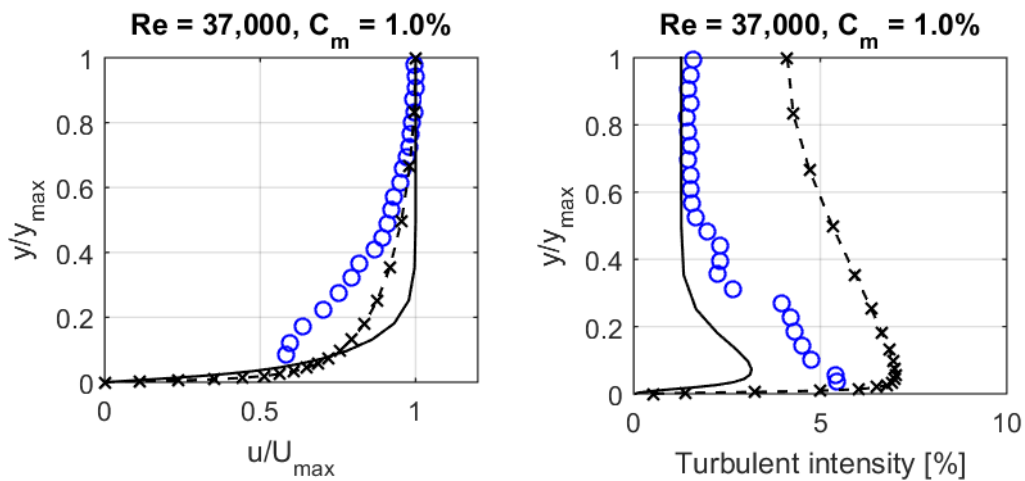


Figure 5.60: Profiles of velocity (left) and turbulent intensity (right) at $Re = 37,000$ and $C_m = 1.0\%$. Computed using the Bingham model (—), the ODF model (--x) and read from Xu & Aidun (2005)(o).

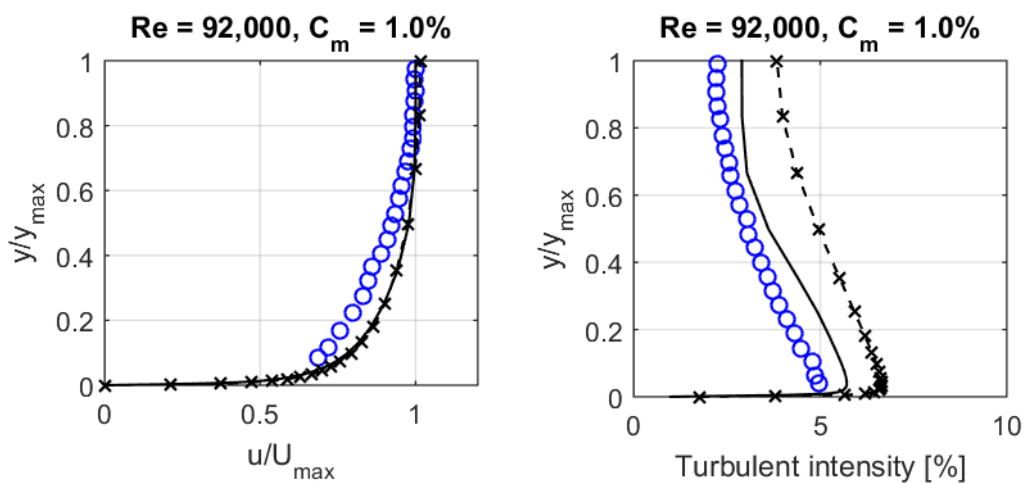


Figure 5.61: Profiles of velocity (left) and turbulent intensity (right) at $Re = 92,000$ and $C_m = 1.0\%$. Computed using the Bingham model (—), the ODF model (--x) and read from Xu & Aidun (2005) (o).

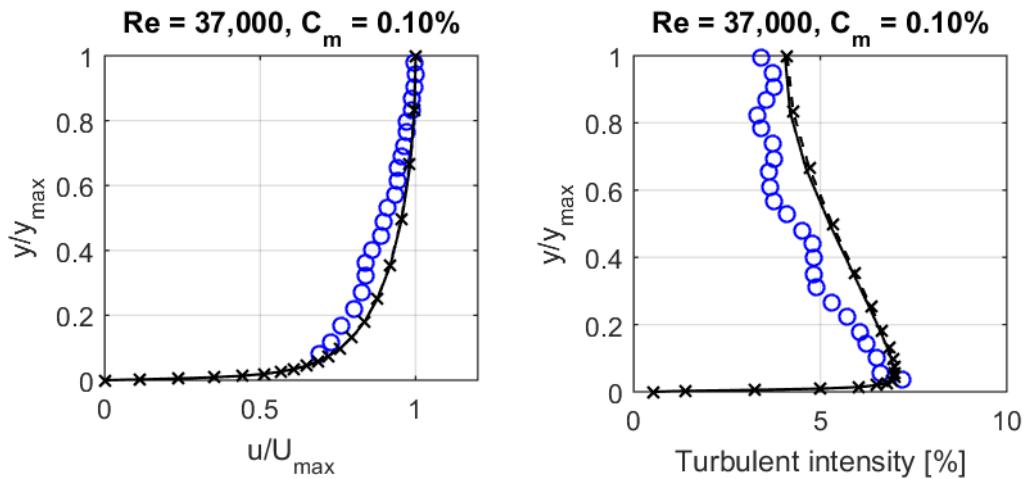


Figure 5.62: Profiles of velocity (left) and turbulent intensity (right) at $Re = 37,000$ and $C_m = 0.1\%$. Computed using the Bingham model (—), the ODF model (---x) and read from Xu & Aidun (2005) (o).

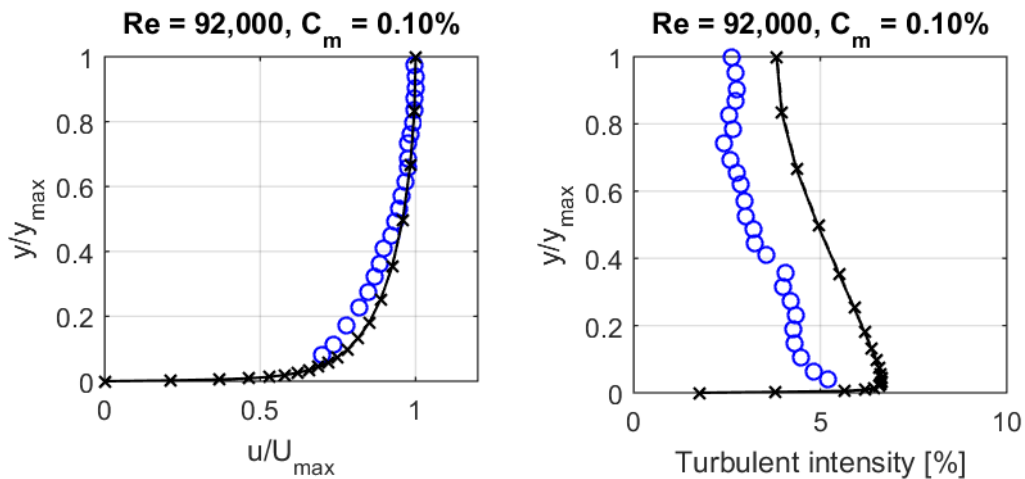


Figure 5.63: Profiles of velocity (left) and turbulent intensity (right) at $Re = 92,000$ and $C_m = 0.1\%$. Computed using the Bingham model (—), the ODF model (---x) and read from Xu & Aidun (2005) (o).

5.3 Disc refiner application

Results from the simulation of the disc refiner, described in Section 4.4, are presented in this section. Computed data was plotted over the cross section of the refiner groove at four different positions downstream of the inlet, namely at x -coordinates 20mm, 40mm, 60mm and 80mm, respectively. A model showing the cross sections can be seen in Figure 5.64. The top wall is moving in the direction from right to left in all plots, as seen from the flow inlet. A clarifying sketch can be seen in Figure 5.65.

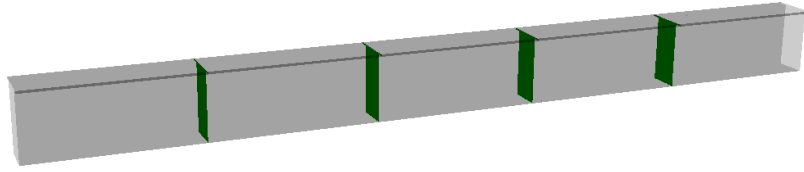


Figure 5.64: 3-D model of disc refiner groove geometry showing the cross sections used for visualising computed data.

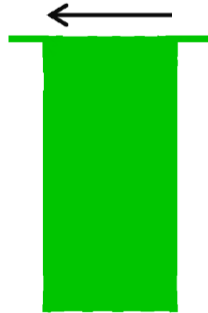


Figure 5.65: Direction of movement of the top wall in the disc refiner model, as seen from the inlet.

For the four positions in the groove direction, the velocity magnitude can be seen in Figure 5.66 plotted over the cross section. It can be observed that at $x = 20\text{mm}$, i.e. fairly close to the inlet, the velocity is practically uniform over the cross section, with exception for boundary layers near channel walls and the moving top wall. Increasing with distance from the inlet the uniformity in the velocity is disturbed to a greater extent. The top wall is moving with velocity 18.6m/s , which is on the same order of magnitude as the streamwise flow with velocity $\sim 20\text{m/s}$. A certain disturbance in the resulting flow is therefore to expect. The moving top wall should induce some swirling pattern in the flow. The intensity of the swirling motion should also increase with distance from the inlet, as the inlet is not swirling.

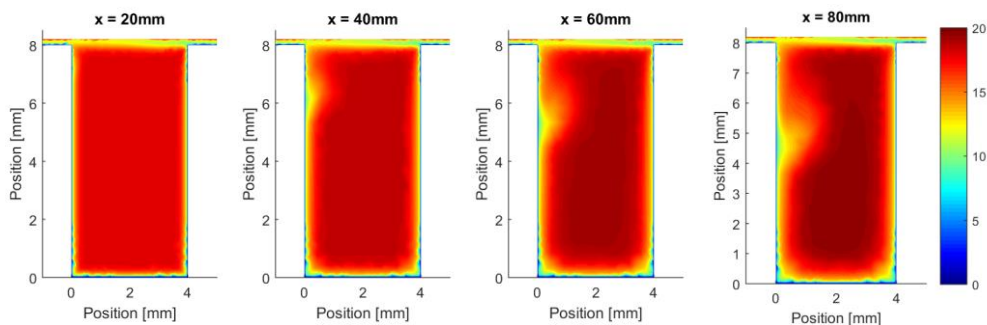


Figure 5.66: Velocity magnitude [m/s] plotted in the groove cross section at four different streamwise coordinates x .

Vectors of velocity projected in the cross section can be seen in Figure 5.67 for channel-part of the cross section, i.e. without the part section in the gap between bars and the moving wall. The gap area was left out since it only had very large velocities in the

direction of the top wall movement. It can be observed from the vectors that the flow is indeed swirling in upper part of the groove. The intensity of the swirling motion is also, as expected, increasing with distance from the inlet. In the lower part of the groove the swirling motion is practically non-existent and it can be seen from the velocity magnitude in Figure 5.66 together with the small magnitude of the projected vectors in Figure 5.67 that the flow there is mainly in the groove direction. Similar results with swirling flow in the upper part of the groove were also found in physical and numerical experiments in Prah Wittberg et. al (2012) for a similar flow model and geometry.

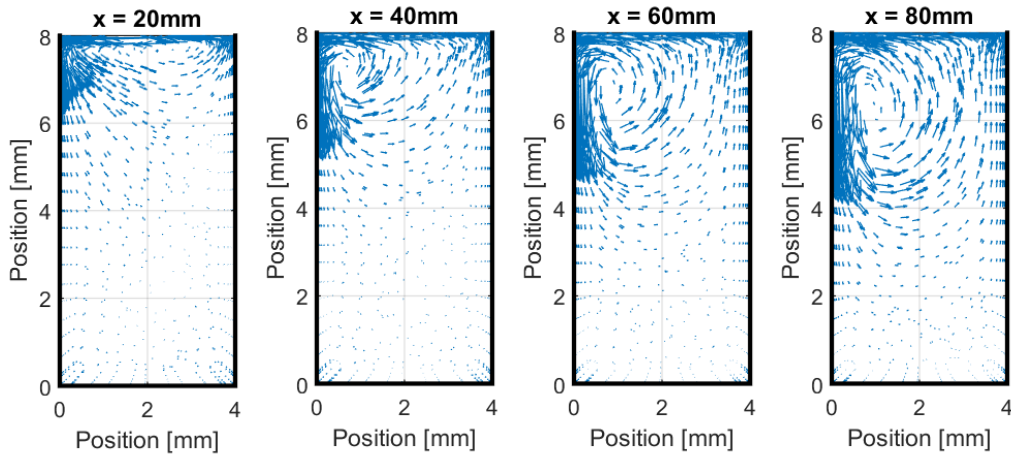


Figure 5.67: Velocity vectors [m/s] projected in the plane perpendicular to the flow direction plotted in the disc refiner groove.

Turbulent intensity in the flow was computed as

$$I = \frac{1}{U_B} \sqrt{\frac{2}{3}k} \quad (5.2)$$

where U_B is bulk velocity in the flow and k turbulent kinetic energy. The bulk velocity was defined as the free stream velocity at the inlet in the simulation, $U_B \approx 20\text{m/s}$. In Figure 5.68 the turbulent intensity is plotted over the cross section of the groove at the same four positions as previous plots. It can be observed that a lot of turbulence occurs close to the moving top wall, especially where the movement forces fluid into to the small gap and onto the bar in the upper left corner. Results near and in the thin gaps should, however, be interpreted carefully because of the poor mesh resolution in the area. Turbulent intensity near all walls increases with increased distance from the inlet which is likely due to increased disturbance from the moving wall on motion and flow development.

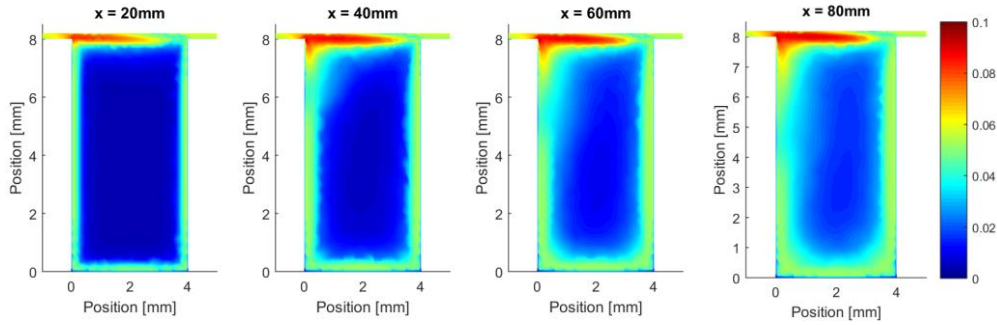


Figure 5.68: Turbulent intensity plotted in the groove cross section at four different streamwise coordinates x . Bulk velocity taken as maximum inlet velocity 20m/s.

The pressure field can be seen plotted over the groove cross section at the four positions in Figure 5.69. Different scales on the colour bars are used for the plots since no common scale showed variations over the cross section clearly. It can be observed that the general pattern over the cross section, although decreasing in magnitude from inlet to outlet, is roughly the same for the four positions. They all show a high pressure zone in the upper left corner of the groove, where the moving top wall forces fluid into the narrow gap and onto the channel wall. Again these results should be interpreted carefully due to the low mesh resolution in the area.

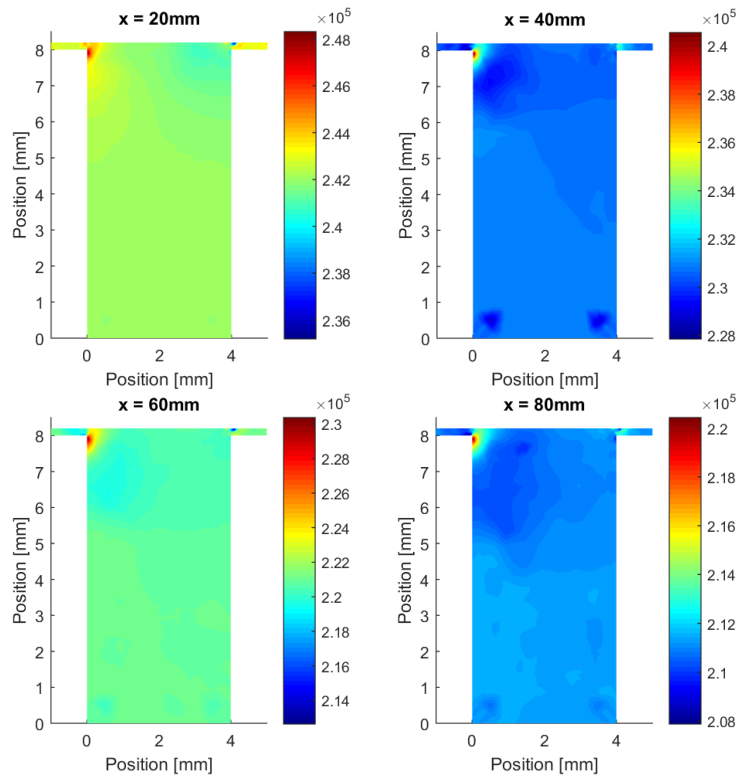


Figure 5.69: Pressure [Pa] plotted in the groove cross section at four different streamwise coordinates x .

The effective viscosity computed from the Bingham model is plotted over the cross section at the four positions in Figure 5.70. The results are consistent with the rest of the

presented results, given that the effective viscosity decreases with shear rate. At the inlet the velocity field is close to uniform except for in the boundary layers so that the shear rate is large close to walls but not away from them. The effective viscosity is thus large in the centre but low near walls. The viscosity is lower in the upper half of the channel which most likely is due to increased shear rate from the induced swirling motion. As the distance from the inlet increases the swirl increases in the top part of the channel and therefore also the shear rate, lowering the effective viscosity. At all walls the turbulent intensity increases further away from the wall, which results in increased boundary layer thickness and higher shear rates further from the wall compared to near the inlet. The zone of high viscosity in the centre of the channel therefore decreases in size as the distance from the inlet increases.

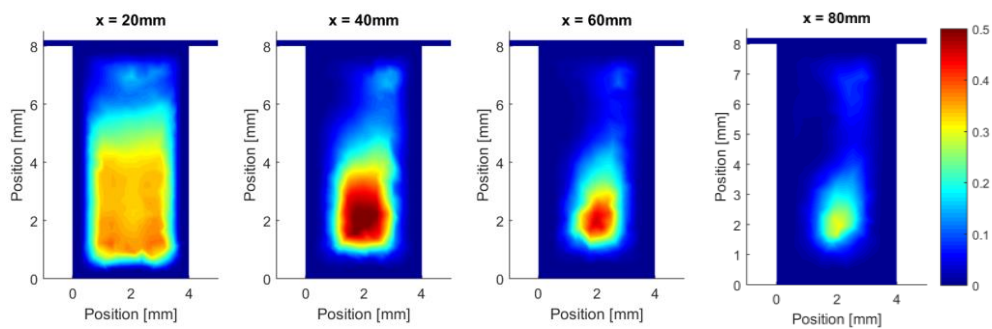


Figure 5.70: Effective viscosity [$\text{Pa} \cdot \text{s}$] plotted in the groove cross section at four different streamwise coordinates x .

6

Discussion

Important parts and aspects of the project are discussed in this section. First a general discussion on relevant error sources is given. The fibre models are then discussed with respect to performance, specific features and possible further development. The two fibre models are also discussed in comparison to one another. A short coverage on the disc refiner simulation is then made. Finally an outlook on future work is presented.

6.1 Error sources

There is always a trade-off between accuracy and computational cost in CFD-simulations and in numerical modelling in general. A coarse numerical grid may give low computational costs but yield inaccurate results. High resolution, on the other hand, gives accurate results but to high if not unaffordable computational costs. In addition, transient simulations with high spatial resolution also demand high temporal resolution CFL condition $u\Delta t/\Delta x \leq 1$ to be fulfilled, enhancing solution stability. A sufficient number of iterations time step must also be executed at each time step to obtain convergence, but a too large number of iterations will increase the computational cost.

Modelling is often a major source of error in CFD-simulations. Turbulence modelling is commonly used, which significantly reduces the mesh resolution required compared to resolving all turbulent fluctuations in a flow. On the other hand certain modelling errors are also introduced. How large the modelling errors are varies between models and different turbulence models are suitable for different flows. In simulations performed within this thesis work fibre modelling should also be considered a major source of errors. Both fibre models tested used macroscopic approaches in contrary to resolving micro-scale mechanisms. In addition, the complex rheology of fibre suspensions varies with concentration and flow regime and it may be difficult to capture all flow features within such simplified models. Certain modelling errors are therefore expected. It may also be remarked that since only two experimental flow cases were used to validate the models the risk of over-fitting must be considered. That would be the case if parameters are fitted very well to the data used for tuning parameters, but may not be representative for flows in general. To further validate the models and the parameter settings more rigorously additional experiments for a variety of representative flow situations would be preferable.

Regarding the validation procedure one should always expect certain errors when comparing results from numerical simulations to experimentally obtained data, as was made in this work. Numerical data has its own error sources, as discussed above, and experimental data itself contains measurement errors. In addition, it can be difficult to correctly model the experimental flow case correctly with respect to, for instance, geometry. The numerical mesh may be differing slightly from the experimental geometry which can cause major errors. An example of this was seen in the process of creating a mesh for the backwards facing step, described in Section 4.2.1, where the flow geometry upstream of the step showed to have a large impact the flow downstream of the step.

For the ODF model a miscalculation in the derivation of a relation between nl^3 , C_V and β , which was then used to compute μ_f , led to that computations were executed with a fibre aspect ratio half as large as originally intended. The error was discovered after all simulations were completed. The wrong values used for β is clearly a possible source of error. It should, though, be remarked that the error generated by systematically using $\beta/2$ instead of β , which resulted from miscalculation, may have been cancelled out by, for instance, the choice of slope in the relation for computing the ODF standard deviation which was tuned to experimental data. A correct value of β may result in another slope being required to resemble the experimental data correctly.

A possible concrete example of a modelling error was the results that all simulations failed to capture the mixing layer in the backwards facing step flow, a feature that could be seen in the experimental data. Even in the case of pure water, which has lower average viscosity than a fibre suspension and should thus exhibit more turbulence, simulations failed to capture the mixing layer. The profiles of turbulent intensity for pure water can be seen in Figure 6.1. The source of the error could, for instance, be either the flow geometry or the turbulence modelling.

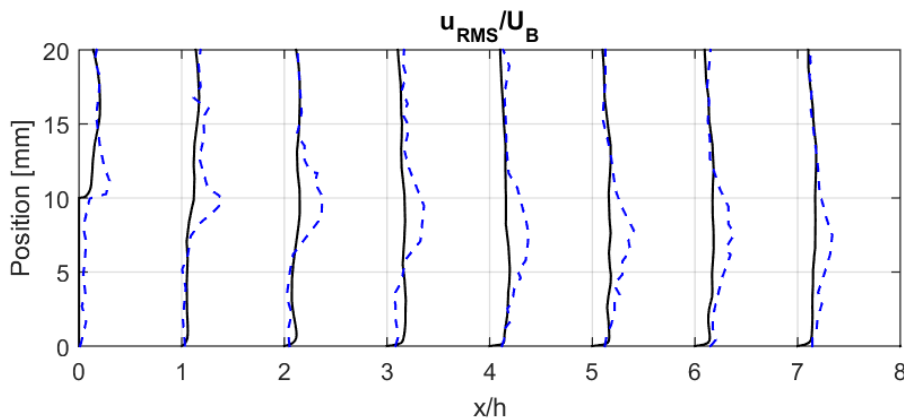


Figure 6.1: Computed profiles of turbulent intensity from simulations of pure water in the backwards facing step (—) and experimental profiles fibre suspension with mass concentration 1.5% from Claesson et al. (2012) (---).

6.2 Fibre models

Results obtained from simulations with both of the studied fibre models succeeded to a large degree to reproduce experimental data both in the flow over the backwards facing step and in the rectangular channel. In both flow cases the resemblance of experimental data was better in the more turbulent flow areas and flow cases, respectively, than where turbulence was less significant. The lower the turbulence levels in a flow are, and as turbulence decays, the more the fibres affect the suspension rheology. The systematic errors in such parts of the flows serve to illustrate the difficulties in finding a model that correctly takes fibre effects into account for all regimes of a flow. As it may be expected, an accurate macroscopic model that is valid for flows governed by complex micro-scale physical phenomena is difficult to construct. However, with the parameters identified as the best for the respective models both models resembled experimental data better than simulations of pure water in the backwards facing step case. In addition the models were further validated in the rectangular channel case. Those simulations showed that the fibre models both yielded results that resembled experimental data well, with exception for slightly overestimation of turbulent intensity, for low concentration and high flow rate. Again cases of turbulent flows where the fibre models give good results. Individual features of the respective models are discussed below.

6.2.1 Bingham model

By modelling fibre suspension flow with the Bingham model a highly simplified description of the rheology is obtained, based on empirical observations and relations. For instance, the parameters a and b , which are used to compute the yield stress τ_y , are not general but varies from suspension to suspension. Modelling a fibre suspension as a non-Newtonian fluid using a Bingham model have been done by others prior to this work where laminar flow was assumed (Fock et al., 2010), (Ford et al., 2006), (Prah Wittberg et al., 2012). In this work, however, the Bingham model also used for simulation of turbulent suspension flow. To argue that the Bingham model may be valid for turbulent flow it can be shown that it exhibits certain features which are expected from experimental observations. Fibre suspensions become fluidised in sufficiently turbulent flows, as described in Section 3.2, meaning that the suspension rheology approaches that of a Newtonian fluid. It can be seen from Equation (4.2) that this is the case with the Bingham model since at large shear rates $\dot{\gamma}$, which occur in turbulent flows, the effective viscosity is

$$\mu = \frac{\tau_y}{\dot{\gamma}} + k \approx k \quad (6.1)$$

What constant viscosity value should then be assigned to the consistency index k ? In the study performed within this work focus was pointed at the parameters a , b and μ_0 while consistency index was set to the viscosity of water. The same was made in Fock et al. (2010) and Ford et al. (2006). However, a study on the parameter k would be desired to fully evaluate the model. Varying the parameters a and b , used to computed the yield stress, and μ_0 showed to have significant impact on the results which could be the case also for k . It should be stressed that the parameter optimisation performed with

simulations on the backwards facing step was done in separate steps. In reality the existence of a correlation between the parameters, including k , is likely. A more rigorous study of the model should therefore include all possible combinations of the model parameters. However, in such a study the number of simulations increases rapidly with the number of values for each parameter.

Since the model effectively acts through a modification of the suspension viscosity the implementation in Fluent was straightforward and of low complexity. A single UDF was created to compute the viscosity from the shear rate according to Equation (4.2). The simple nature of the implementation also only resulted in a slightly increased computational cost, compared to simulations of pure water flow. Some instabilities were found, though, causing the need for an increased number of iterations per time step and smaller under-relaxation factors. A stable solution computed with constant viscosity before activating the Bingham model was also crucial to obtain stability. The exact source of the instabilities is not known for certain, but they may arise from large gradients in effective viscosity in some parts of the flow.

6.2.2 ODF model

Although being a lot more complex than the Bingham model, the ODF model does also provide a simplified description of fibre suspension rheology. The coupling from the orientation distribution of fibres to the fluid momentum equations rely on assumptions such as fibres being rigid and in a certain concentration regime. Anisotropic effects of fibre orientation are accounted for and influence the rheology while possible additional anisotropic effects from fibres bending and twisting are neglected. The developed model for the fibre distribution is empirical as it is based on results from numerical and experimental results on the ODF in turbulent fibre suspension flows. Micro-scale mechanisms determining movement and interaction of fibres, and thus the evolution of the ODF, are being modelled and not resolved. Now, is the level of detail sufficient to successfully describe a fibre suspension and can the modelling justified? First of all, further evaluation of the model is needed to answer the questions fully. However, computed results showed resemblance with experimental data to a certain extent. It should also be remarked that while many levels of anisotropy can be incorporated in a fibre model, at some point one needs to stop at a level that is possible to implement and computationally affordable. In this work both computational resources and time were limiting factors and the model was therefore only subjected to a limited study.

Since the model involves computation of the many components of the fibre orientation tensors, where a lot of work was put into constructing the a priori expressions, the implementation itself of the model was rather time-consuming and complex. The model increased the number of computations performed per iteration and therefore also increased the computation cost slightly. However, the a priori construction of the explicit expressions for the orientation tensor components significantly decreased the number of operations needed compared to numerically solve the integrals (4.17) (4.18) in each iteration. The model showed good stability and converged easily without the need to increase under-relaxation factors or the number of iterations per time step, compared to simulations of pure water in the same geometries.

The ODF model developed in this work does not account for any near-wall effects on the orientation distribution. Such effects could be induced either by the flow properties of the boundary layer or by the fact that fibres cannot rotate with total freedom due to adjacency of solid boundaries. Modelling of such effects could be introduced into the model by the use of some near-wall modification of the modelled ODF.

Two parameters were identified for the ODF model, namely the ODF standard deviation σ and the sensitivity constant D_f . While D_f was introduced to account for sensitivities with respect to unknown fibre suspension properties, σ can be considered as the main parameter studied in the model. Changing the parameter D_f , though, had a significant impact on the results indicating that the ODF model used is sensitive to correct information, or assumptions, on fibre properties such as aspect ratio. A possible use for the parameter D_f could therefore be to serve as an empirical constant for the ODF model which may be found different from suspension to suspension, not all unlike the parameters a and b used to compute yield stress in the Bingham model.

ODF standard deviation σ was assumed to vary with turbulent intensity I . Results from simulations where σ was computed as a linear function of I yielded better results than simulations with homogeneous σ , indicating that the assumption may be correct. Another indication that supports the assumption can be seen from the magnitude of the orientation tensors. It was found that the maximum magnitude of all components of a_{ij} and a_{ijkl} decreased for increasing σ . The observation is visualised in Figure 6.2 where the maximum magnitudes, taken over all possible flow directions $(\bar{\phi}, \bar{\theta})$, for all components of the orientation tensors are plotted against σ . Since the intent with the plot only is to show the common trend for all components the legends for the 21 unique components have been left out.

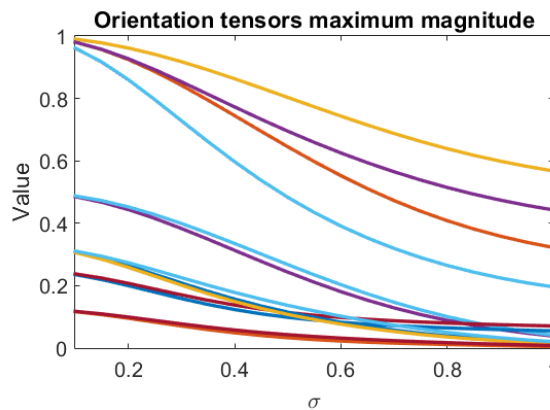


Figure 6.2: Maximum magnitude of all components of the fibre orientation tensors a_{ij} and a_{ijkl} for varying ODF standard deviation σ .

Assuming that a decrease in maximum magnitude points to an overall decrease in magnitude for the tensor components, the results then implies that the magnitude of fibre stresses τ_{ij}^f decreases with increasing σ . In other words, the larger the turbulent intensity is in the flow the smaller the fibre stresses in the fluid are and thus the suspension

behaves more like a Newtonian fluid. The behaviour is expected for a fibre suspensions as it should become fluidised in turbulent flow, as described in Section 3.2. It should be remarked that computing the ODF standard deviation σ from turbulent intensity I in the way that was done in this work introduces some arbitrariness in how I is defined. The computation of I demands the definition of a bulk velocity U_B which may be far from obvious in some flow cases. The consequence is that the model is not well-defined for an arbitrary flow case.

6.2.3 Comparison of fibre models

Both the Bingham model and the ODF model yielded results that resembled the experimental data well in large parts of the flow. For both models it was also observed that varying model parameters had clear impact on the computed results. Which one of the Bingham model and the ODF model is then the best? To answer the question the purpose of the modelling should be considered. The scope of this work was to find a fibre model suitable for engineering applications with sufficient accuracy and with limited computational cost. The ODF model opens up for a detailed description of the fibres suspension due to its complexity and description of individual components of the additional stresses arising from fibres in the suspension. It should be stressed, though, that the ODF model proposed is a new model and has been studied to a very limited extent within this work. The Bingham model, on the other hand, contains fewer uncertainties and relies on fewer parameters that also can be found literature. In addition it has been used to model fibre suspension flow prior to this work with examples to be found in literature. Further, it also has slightly lower computational cost than the ODF model and is easier to implement. With further investigation of the ODF model it may open up for the possibility of using it as an alternative to the Bingham model for applications with turbulent fibre suspension flows. However, for the sake of this project the Bingham model was considered more suitable.

6.3 Disc refiner application

The simulation performed with the disc refiner model was made to further validate the use of the chosen fibre model in an application relevant for the pulp and paper industry. Results from the simulation model showed a flow pattern that was expected and that could be found for flow cases studied experimentally and numerically in Prah *Wittberg et al.* (2012). In their study different types of wood fibres at different consistencies yielded slightly different results, though. Results from the simulation in this thesis work did to a large extent yield results that could be expected prior to computations. However, it should be stressed that since the gap clearance in the refiner model has the size on the order of a few fibre diameters it is questionable if a fibre model where the suspension is seen as a continuum, as the Bingham model, can really be justified. The results should therefore at most be seen as coarse guidelines to the flow pattern in a disc refiner groove rather than as a detailed description.

6.4 Future work

The fibre models covered in this thesis work were only subjected to a small study due to limitations in time and computational resources. To gain further knowledge on either of

the fibre models additional and more thorough studies need to be conducted. Additional physical and numerical experimental studies are also crucial a process of further developing the models. Physical experiments can give knowledge on fibre suspension flow structures that are needed to develop the models to more sophisticated levels of detail. Numerical experiments are needed to further validate the models with experimental data, but also to determine numerical issues and advantages for the respective models. Approaches for further development of the two models studies in this thesis work are proposed below.

6.4.1 Bingham model

Current form of the Bingham model provides a simple description of fibre suspension rheology implemented by modifying the suspension viscosity. The method results an isotropic modification of viscous stresses, as all stresses are multiplied by the same factor as

$$\tau_{ij} = 2\mu(\dot{\gamma}) \cdot S_{ij}. \quad (6.2)$$

A conceivable concept to further develop the rheology model could be to extend the detail by introducing some anisotropic modification where the viscosity is modified individually for each stress component τ_{ij} . The viscous stresses could be computed on the form

$$\tau_{ij} = 2\mu_{ij}(S_{ij}) \cdot S_{ij}, \quad (\text{no summation over } i, j), \quad (6.3)$$

where the viscosity μ_{ij} then no longer is isotropic and its components depend on the strain rate components S_{ij} in some way. A model on this form would introduce a higher extent of freedom for the model and might therefore give better description of fibre suspension rheology. However, thorough experimental and mathematical studies would be needed to correctly construct such a model.

6.4.2 ODF model

First of all, since the ODF model at this stage is new and many of uncertainties exist, simulations on a variety of flows should be performed and compared with experiments where information on all model parameters are known. By conducting such a rigorous study two main questions could come closer to being answered. Those questions are how do the different parameters affect the rheology described by the model, and what fibre types and concentration regimes are they valid for? A more detailed investigation on the structures of the fibre stresses τ_{ij}^f could also serve as valid input for further development of the model.

A more sophisticated method to compute the ODF standard deviation σ is needed. As discussed in Section 6.2.2 computing σ from the turbulent intensity I introduces some arbitrariness since a reference velocity is needed to compute I . In the Fokker-Planck equation the rotational diffusivity of the ODF D_p can be related to the strain rate in the flow (Zhang, 2014). The idea that velocity gradients in the fluid will affect and induce rotational motion of fibres and increase the variance of the ODF is also somewhat

intuitive. In addition, the strain rate is used to model the effect of unresolved turbulent fluctuations in both RANS models and LES models. A use of the strain rate tensor to connect ODF standard deviation with turbulence is therefore conceivable. The idea also opens up for possible further development of the ODF model to incorporate a higher level of detail. S_{ij} holds anisotropic information on the flow which could be used for a model where the ODF standard deviation needs not to be equal in all directions. The ODF could instead be modelled with a more general bivariate normal distribution, where the correlation between the angles ϕ and θ not necessarily need to be zero. It should be remarked, though, that the method of fitting one-dimensional Fourier series expressions for the ϕ - and θ -parts of the fibre orientation tensors would in that case fall apart due to the non-zero correlation of ϕ and θ . A suitable two-dimensional regression model would instead be appropriate.

7

Conclusion

Approaches for modelling of turbulent fibre suspension flow were studied and two models of different type were successfully implemented numerically. Both models effectively act as single-phase flow models through modification or addition of viscous stresses in the Navier-Stokes equation. A simpler model was denoted the Bingham model, where the suspension is modelled as a non-Newtonian fluid by computing the effective viscosity as a function of shear rate. A more complex model was denoted the ODF model, where the suspension rheology was modelled through an additional stress tensor computed from the orientation distribution of suspended fibres. A model for the orientation distribution function (ODF) was developed using normal distributions for the angular coordinates describing fibre rotation and their variance was connected to turbulence. Explicit expressions to compute the fibre stresses as functions of the flow field were constructed from the model using Fourier series.

For both models simulation results were compared to experimental data for the purpose of validation. The parameter settings yielding the results with best resemblance of experimental data for the respective models were then identified. Both models performed well along with reasonable computational cost and stability. The Bingham model had a simple implementation and resembled experimental data slightly better than the ODF model. In addition, the ODF model is in need of further studies at the current stage. The Bingham model was therefore identified as the best model and was also used to simulate the flow in a disc refiner model and successfully resembled general flow patterns from numerical and physical experiments in literature. In summary the aim of the work was fulfilled and a suitable fibre model was delivered.

References

- Andersson, S.R., Ringnér, J. & Rasmuson, A., 1999. The network strength of non-flocculated fibre suspensions. *Nordic Pulp and Paper Research Journal*, 14(1), pp.61-70.
- Andric, J. et al., 2013. A study of a flexible fiber model and its behavior in DNS of turbulent channel flow. *Acta Mechanica*, 224(10), pp.2359-74.
- ANSYS Inc. (a), 2013. *ANSYS Fluent Theory Guide*. Canonsburg, PA, USA: ANSYS Inc.
- ANSYS Inc. (b), 2013. *ANSYS Fluent User's Guide*. Canonsburg, PA, USA: ANSYS Inc.
- Bennington, C.P.J. & Kerekes, R.J., 1996. Power requirements for pulp suspension fluidization. *TAPPI Journal*, 79(2), pp.253-58.
- BETA CAE Systems S.A., 2014. *ANSA version 15.0.x User's Guide*. Epanomi, Greece: BETA CAE Systems S.A.
- Claesson, J., Wikström, T. & Rasmuson, A., 2012. Flow of concentrated fiber suspensions over a backward facing step studied using LDA. *Nordic Pulp and Paper Research Journal*, 27(3), pp.653-61.
- Crowe, C.T. & Michaelides, E.E., 2006. *Multiphase Flow Handbook*. Boca Raton: CRC Press.
- Davidson, L., 2014. *Fluid Mechanics, Turbulent Flow and Turbulence*. Lecture notes. Gothenburg: Chalmers University of Technology Department of Applied Mechanics.
- Davidson, L., 2015. *An Introduction to Turbulence Models*. Lecture notes. Göteborg: Chalmers University of Technology Department of Thermo and Fluid Dynamics.
- Derakhshandeh, B., Hatzikiriakos, S.G. & Bennington, C.P.J., 2010. The Apparent Yield Stress of Pulp Fiber Suspensions. *Journal of Rheology*, 54(5), pp.1137-54.
- Derakhshandeh, B., Kerekes, R.J., Hatzikiriakos, S.G. & Bennington, C.P.J., 2011. Rheology of pulp fibre suspensions: A critical review. *Chemical Engineering Science*, 66, pp.3460-70.
- European Commission, 2014. *Progress Towards Achieving the Kyoto and 2020 Objectives*. Progress report. Brussels: European Commission.
- Fock, H., Claesson, J. & Wikström, T., 2011. Near Wall Effects in the Plug Flow of Pulp Suspensions. *The Canadian Journal of Chemical Engineering*, 89, pp.1207-16.

- Fock, H., Rasmuson, A. & Wikström, T., 2010. CFD modeling of non-newtonian fluid mixing accounting for transient changes in local solids concentration - application to an agitated pulp stock chest. *Nordic Pulp and Paper Research Journal*, 25(1), pp.56-64.
- Ford, C., Ein-Mozaffari, F., Bennington, C.P.J. & Taghipour, F., 2006. Simulation of Mixing Dynamics in Agitated Pulp Stock Chests using CFD. *AIChE Journal*, 52(10), pp.3562-69.
- Frenander, K. et al., 2015. Flow Induced Venturi Cavitation to Improve Energy Efficiency in Pulp Production [unpublished]., 2015.
- Illikainen, M., Härkönen, E., Ullmar, M. & Niinimäki, J., 2007. Power consumption distribution in a TMP refiner: comparison of the first and second stages. *TAPPI Journal*, 6(9), pp.18-23.
- IPCC, 2014. *Climate Change 2014*. [Online] Available at: http://www.ipcc.ch/pdf/assessment-report/ar5/syr/SYR_AR5_LONGERREPORT_Corr2.pdf [Accessed 23 January 2015].
- Irgens, F., 2014. *Rheology and Non-Newtonian Fluids*. Springer. (eBook).
- Johansson, Ö. & Landström, L.-O., 2010. *Slutrapport: Hur kan resonansfenomen utnyttjas för att minska energiförbrukningen vid framställning av papper*. Technical report. ÅForsk.
- Kerekes, R.J., 2006. Rheology of fibre suspensions in papermaking: An overview of recent research. *Nordic Pulp and Paper Research Journal*, 21(5), pp.598-612.
- Krochak, P.J., Olson, J.A. & Martinez, M., 2009. Fiber suspension flow in a tapered channel: The effect of flow/fiber coupling. *International Journal of Multiphase Flow*, 35(7), pp.676-88.
- Lindström, S.B. & Uesaka, T., 2008. Particle-level simulation of forming of the fiber network in papermaking. *International Journal of Engineering Science*, 46(9), pp.858-76.
- Lin, J., Liang, X. & Zhang, S., 2011. Fibre orientation distribution in turbulent fibre suspensions flowing through an axisymmetric contraction. *The Canadian Journal of Chemical Engineering*, 89(6), pp.1416-25.
- Lin, J.Z., Liang, X.Y. & Zhang, S.L., 2012. Numerical simulation of fiber orientation distribution in round turbulent jet of fiber suspension. *Chemical Engineering Research and Design*, 90, pp.766-75.
- Lin, J.-Z., Sun, K. & Lin, J., 2005. Distribution of Orientations in Fibre Suspension Flowing in a Turbulent Boundary Layer. *Chinese Physics Letters*, 22(12).
- Lundberg, A. et al., 2014. An automatic method for optimizing venturi shape in cavitation flows [unpublished]., 2014. (Abstract accepted in July 2014).

- Lundberg, A. et al., 2015. Automated Aerodynamic Vehicle Shape Optimization Using Neural Networks and Evolutionary Optimization. *SAE International journal of passenger cars. Mechanical systems*, 8(1).
- Lundberg, A. et al., 2015. *Flow Induced Cavitation - Phase 2*. Technical Report. ÅF-Industry AB.
- Moosaie, A. & Manhart, M., 2013. Direct Monte Carlo simulation of turbulent drag reduction by rigid fibers in a channel flow. *Acta Mechanica*, 224(10), pp.2385-413.
- Mörtstedt, S.-E. & Hellsten, G., 2010. *Data och Diagram, Energi- och kemitekniska tabeller*. 7th ed. Stockholm: Liber AB.
- Nordling, C. & Österman, J., 2006. *Physics Handbook for Science and Engineering*. 84th ed. Lund, Sweden: Studentlitterature AB.
- Olson, J.A., Frigaard, I., Chan, C. & Hämäläinen, J.P., 2004. Modeling a turbulent fibre suspension flowing in a planar contraction: The one-dimensional headbox. *International Journal of Multiphase Flow*, 30(1), pp.51-66.
- Prahl Wittberg, L. et al., 2012. Flow conditions in the grooves of a Low-Consistency refiner. *Nordic Pulp and Paper Research Journal*, 27(2), pp.173-83.
- Rajabi Nasab, N., Olson, J.A., Heymer, J. & Martinez, M.D., 2014. Understanding of No-load Power in Low Consistency Refiners. *The Canadian Journal of Chemical Engineering*, 92(3), pp.524-35.
- Rice, J.A., 2007. *Mathematical Statistics and Data Analysis*. 3rd ed. Belmont, California: Thomson Brooks/Cole.
- Shaqfeh, E.S.G. & Fredrickson, G.H., 1990. The hydrodynamic stress in a suspension of rods. *Physics of Fluids*, 2(1), pp.7-24.
- Swedish Energy Agency, 2014. *En samlad bild över energiläget i Sverige*. [Online] Available at: <http://www.energimyndigheten.se/Press/Nyheter/En-samlad-bild-over-energilaget-i-Sverige/> [Accessed 23 January 2015].
- Tu, J., Yeoh, G.-H. & Liu, C., 2013. *Computational Fluid Dynamics A Practical Approach*. 2nd ed. Waltham MA, USA: Elsevier.
- Xu, H. & Aidun, C.K., 2005. Characteristics of fiber suspension flow in a rectangular channel. *International Journal of Multiphase Flow*, 31, pp.318-36.
- Yang, W., Shen, S. & Ku, X., 2013. A new model of turbulent fibre suspension and its application in the pipe flow. *The Canadian Journal of Chemical Engineering*, 91(5), pp.992-99.
- Zhang, F., 2014. *Instability in Settling Fibres: A Numerical study*. Doctoral thesis in Engineering Mechanics. Stockholm, Sweden: Royal Institute of Technology KTH Department of Mechanics.

